Instabilities of microcapsules in flow : breakup and wrinkles

Kaili Xie

Discipline: Mécanique et Physique des Fluides
Laboratoire: M2P2 UMR7340, LRP UMR5520
Ecole Doctorale: Mécanique, Physique, Micro et Nanoélectronique (ED353)

THÈSE DE DOCTORAT

pour obtenir le grade de

DOCTEUR de l'ECOLE CENTRALE de MARSEILLE

Instabilités de microcapsules en écoulement: rupture et rides

Instabilities of microcapsules in flow: breakup and wrinkles

---

par

Kaili XIE

Soutenance prévue le 13 septembre 2019 devant le jury composé de:

Mme. Anke LINDNER	Prof., PMMH, ESPCI, Paris	Président
M. Chaouqi MISBAH	DR., LIPhy, CNRS, Grenoble	Rapporteur
M. Christian LIGOURE	Prof., LCC, Uni. Montpellier, Montpellier	Rapporteur
M. Dominic VELLA	Prof., Uni. Oxford, Oxford	Examinateur
M. Clément de LOUBENS	CR., LRP, CNRS, Grenoble	Co-encadrant
M. Marc LEONETTI	CR., LRP, CNRS, Grenoble	Co-directeur
M. Marc JAEGER	Prof., M2P2, Centrale Marseille, Marseille	Direteur de thèse

"Simplicity is the ultimate sophistication."

Leonardo da Vinci

"无极生太极，太极生两仪，两仪生四象，四象生八, 八卦演万物。"

≪易传≫

Acknowledgments

The work in this dissertation has been accomplished under the frame work of Laboratory M2P2 in Centrale Marseille and Laboratory LRP in Université Grenoble Alpes. I therefore wish to thank the members, joining in the work, who help me and support my research. Also I thank the jury members for spending their time on reviewing my manuscript and for their comments. I specially thank my family for their endless encouragement and support.

I would like to firstly express my deep gratitude to my supervisors, Marc Jaeger at M2P2, Clément de Loubens and Marc Leonetti at LRP. Without their patient guidance and constructive criticism, I would never be able to finish my Ph.D. dissertation. Many thanks to M. Jaeger who gave me the opportunity to pursue my Ph.D. in France after an interview in Beijing. Specially, my sincere gratitude is to C. de Loubens who is not only my advisor for my research, but also really has been another family to me. The first year in Marseille, he introduced me to the experimental studies, helping me open the door to world of soft matter. Then, when I moved to Grenoble, he helped me a lot in my daily life, for example searching apartments. I also would like to thank M. Leonetti who is the captain of our project, guiding me to the right direction.

I would like also to thank the external experts in the jury of my Ph.D. defense, Mme. A. Lindner from ESCPI, C. Misbah from LIPhy CNRS, C. Ligoure from Université Montpellier and D. Vella from University of Oxford. Their insightful comments and friendly suggests help me to improve the writing of my thesis.

I would like to thank Frédéric Dubreuil at Cermav and Hugues Bonnet at ICMG for providing the AFM platform to obtain the topology of our samples. Also many thanks to Mme. Rachel Martin and Frédéric Charlot at CMTC at Grenoble INP for discussion and helping me measure the thickness of membrane with SEM and FIB platforms. Many thanks to Danièle Centanni and Philippe Marmottant at microFAB of LIPhy for giving access to prepare PDMS microfluidic chips. Also, I would like to thank Eric Bertrand at IRPHE for helping me print the 3D microfluidic chips by using a 3D printer.

In LRP, I would like to thank Mohamed Karrouch, Didier Blésès, Frédéric Hugenell, Eric Faivre and Hélène Galliard for their great unselfish help in my experiments. Thank you for every time you being able to solve my technical problems. Many thanks

to Louise Infuso, Sylvie Garofalo and François Bergerot for preparing documents in French every time for me. Besides, many thanks to all the permanent researchers, Hugues Bodiguel, Frédéric Pignon and Denis Roux, etc. at LRP for your useful discussion and suggestion in my research work.

I would like to thank my friends Dr. Yun-Long Wei, Dr. Shuming Bai, Prof. Congshan Zhuo, Dr. Xiaotong Zhan, Dr. Xue Chen, Dr. Jian Yang, Dr. Jun Chen, Dr. Wei Zhu, Dr. Donglai Gao, Dr. Guillaume Martrou, Xinxin Qian, Zhuang Pei and Jinming Lyu for the excellent moments that we shared during my first year of Ph.D. in Marseille. Many thanks to Prof. Gang P. Chen at M2P2 for helping me adapt to the new living in Marseille. Also, I would like to appreciate William Chevremont, Dr. Candice Rey, Dr. Alexis Mauray, Dr. Ziemihori Ouattara, Hugues Mondesert, etc for playing Squash together as a team. I have memorable experience living in Grenoble. Many thanks to Dr. Revaz Chachanidze, Dr. Antoine Naillon and Mehdi Maleki for their discussion about my project, and suggestion for experimental images processing. Special thanks to Revaz and Mehdi for their correction for my thesis manuscript. All the colleagues and friends at LRP, Ahlem, Sihem, Essa, Moctar, Haimeng, Clément, Youness, Alice, Diego, Mohamad, Luis Carlos and Xavier, etc, have my sincere gratitude for passing joyful moments together at LRP to explore and discover the unknown world of rheology.

I am deeply grateful for the financial support for my research from the Ph.D. scholarship of Centrale Marseille - China Scholarship Council and the CNRS. These fundings gave me more flexible chances to learn and discover new things.

Finally, I would like to express deep gratitude to my family. My parents always offer me warm embrace when I go home, no matter what troubles I encountered outside. They teach me how to become a strong man facing life. I also owe many thanks to my dear brother Keli, and dear sisters Kefang and Keling. Their loves to me are always the strongest power to force me advance. I am grateful for the encouragement, patience and unconditional love of my wife Lili Gao. The distance between China and France has never been an obstacle to our love. Deeply loving each other motivates me to accomplish this PhD.

Abstract

Deformable particles such as cells, vesicles and microcapsules exhibit abundant spatiotemporal dynamics in flows. In particular, it is commonly accepted that the membrane mechanical properties and flow types govern these dynamics, for example global deformation and shape oscillation. There also exist locally self-organized shape modulations in response to the flows, for example wrinkling and breakup instabilities. The objective of this thesis is to understand the emergence of such instabilities on microcapsules. The challenge comes to the tunability and control of the membrane rheological properties. We first develop a new formulation of assembling microcapsules made of a thin membrane with widely tunable properties. We describe an original visualization set-up that images microcapsules in orthogonal views, allowing a 3D characterization of pattern formation and the first measurement of wrinkles wavelength. The wrinkling instability is characterized by various scaling laws to highlight the salient parameters. Especially, wrinkling pattern appears above a unique critical capillary number regardless of membrane properties. Wrinkles-to-folds transition is observed if the capillary number is greater than the second critical capillary number. However, under extremely high capillary number, microcapsules surface become stable again, prior to breakup. A phase diagram of capsules breakup in extensional flow is also established and compared to the case of droplets.

Keywords: microcapsule, mechanical instabilities, wrinkles, breakup, interfacial rheology, Stokes flow.

Résumé

Les particules déformables telles que les cellules biologiques, les vésicules ou encore les capsules présentent une grande richesse de dynamiques sous écoulement. Ces dynamiques, telles que des oscillations de la forme, résultent du couplage fluide-structure entre la réponse mécanique de la membrane et la contrainte hydrodynamique appliquée. La résistance de la membrane au cisaillement et à la flexion induit une nouvelle classe d'instabilités conduisant à une modulation de la membrane qui apparaissent comme des plis. L'objectif de cette thèse est de comprendre l'émergence de telles instabilités sur des microcapsules. Nous avons développé une nouvelle méthode de fabrication qui permet de varier les propriétés mécaniques et l'épaisseur de la membrane dans une grande gamme. Un montage expérimental original a été développé pour visualiser la formation de motifs et la longueur d'ondes des plis. L'instabilité de plissement est caractérisée par plusieurs lois d'échelle permettant d'établir les nombres sans dimension pertinents. En particulier, la forme est instable quand le nombre capillaire est plus grand qu'une valeur unique indépendantes des propriétés mécaniques membranaires. A un plus grand nombre capillaire, la transition plis-creux (ou plis profonds localisés) est observée et caractérisée. Au-delà d'un nombre capillaire, la forme redevient stable. A plus grand nombre capillaire, la transition vers la fragmentation ou la fracture de la capsule est caractérisée par un diagramme de phase et comparé à celui d'une goutte.

Mots-clés: microcapsule, instabilités mécanique, rides, rupture, rhéologie interfaciale, écoulement de Stokes

List of publications

Articles

- **K. Xie**, C. de Loubens, F. Dubreuil, D. Z. Gunes, M. Jaeger and M. Leonetti. Interfacial rheological properties of self-assembling biopolymer microcapsules. *Soft Matter*, 13(36): 6208-6217, 2017.
- **K. Xie**, C. de Loubens, R. Chachanidze, F. Dubreuil and M. Leonetti. Wrinkling and folding of microcapsules in extensional flow. *Submitted*, 2019.
- **K. Xie**, C. de Loubens, F. Dubreuil and M. Leonetti. Microcapsules breakup in extensional flow. *In preparation*, 2019.

Oral presentations

- **K. Xie**, C. de Loubens, M. Jaeger and M. Leonetti. Wrinkling and folding on soft microcapsules. *22^{e} Rencontre du Non-Linéaire*. 26-28 March 2019, Paris, France.
- **K. Xie**, C. de Loubens, F. Dubreuil, M. Jaeger and M. Leonetti. Wrinkling instability of biomimetic cells. *Journee GDR CellTiss*. 1-3 October 2018, Paris, France.
- **K. Xie**, C. de Loubens, F. Dubreuil, M. Jaeger and M. Leonetti. Wrinkling instability on microcapsule in elongation flow. *12th European Fluid Mechanics Conference*. 9-13 September 2018, Vienna, Austria.
- **K. Xie**, C. de Loubens, F. Dubreuil, M. Jaeger and M. Leonetti. Interface assembly of microcapsules via liquid-liquid droplets templates. *MicroNano Fluidics*. 15-16 March 2018, Grenoble, France.
- **K. Xie**, C. de Loubens, F. Dubreuil, M. Jaeger and M. Leonetti. Monodisperse microcapsules with controlled interfacial properties generated in microfluidic T-shape junction. *23ème Congrès Français de Mécanique*. 28 August-1 September 2017, Lille, France.

Poster presentations

- **K. Xie**, C. de Loubens, F. Dubreuil, M. Jaeger and M. Leonetti. Interfacial rheology of composite microcapsules: elasticity, plasticity and membrane bursting. *Glyco@Club days*. 23-24 April 2018, Grenoble, France.
- **K. Xie**, C. de Loubens, M. Jaeger and M. Leonetti. Interfacial rheology of composite microcapsules: elasticity, plasticity and membrane fracture. *Winter School*. 16-20 January 2017, Grenoble, France.

Others

- M. Maleki, **K. Xie**, M. Leonetti, H. Bodiguel, C. de Loubens. Strucuration of suspensions of soft microcapsules in confined flow, an experimental study. *Annual European Rheology Conference*. April 2019, Portoroz, Slovenia.
- C. de Loubens, **K. Xie**, F. Dubreuil, M. Leonetti. Dynamics of microcapsules in elongational and shear flows. *Deutsche Physikalische Gesellschaft Spring Meeting*. March 2017, Germany.

Contents

General introduction

Inspired by biological cells, soft artificial particles such as microcapsules are designed by encapsulating liquid core media with thin membranes. The membranes generally are solid-like, having elastic nature, which can protect the core media from the external environment. The encapsulated contents thus can be released or exchanged in a controlled way, which are widely used in pharmaceutical [1] and bioengineering applications [2]. Since microcapsules share common mechanical features with biological cells, e.g., red blood cells (RBCs), they are also often considered as artificial models [3] used to understand the dynamics of RBCs in microcirculation flows [4]. It is thus essential to understand the mechanical response of microcapsules to the applied stress fields, both in applications and fundamental studies.

In flow, it is well understood that soft particles are elongated, as a result of the competition between hydrodynamic stress and membrane elasticity resistance. Several complex dynamical motions might appear during the deformation. For example, in a shear flow, both RBCs and microcapsules are observed to show membrane tank-treading (TT), rigid body-like tumbling (TU) and inclination swinging (SW) [5, 6]. In some cases, there exists wheel motion-like rolling (RO) for RBCs [7]. Viscous dissipations inside and outside the particles, membrane constitutive laws, and flow types are accepted to govern the global deformation and the dynamics. Experimentally, well-controlled membrane properties are required.

However, there are few investigations focusing on the locally self-organized shape modulations of microcapsule in response to the flow, namely membrane mechanical instabilities such as wrinkling and breakup. Indeed, the challenges to control these instability patterns come to the tunability of **membrane properties** and consideration of **curved-closed geometry** of microcapsule.

Thin elastic sheet undergoes surface wrinkling when it is exposed to sufficiently large compression locally. Similarly, on soft particles, due to the contribution of membrane elasticity, the surface might lose their mechanical stability, leading to wrinkling or folding. Buckling instability of RBCs has been first observed in a cone-plate shear flow, with chemical-modified membrane, in which the pattern is assumed to have a wavelength with the same order of magnitude as the cells diameter ($\approx 8\ \mu$m) [8].

Artificial microcapsules have been expected to show well-organized wrinkles in a Poiseuille flow [9] and shear flow [10], due to compression loop presence at the rear and middle sections, respectively. Confinement (capsule size to channel dimension) and flow capillary number are found to play essential roles in the formation of wrinkling pattern. It is well accepted that compression in the membrane, inducing negative stress tensors, dominates the emergence of wrinkling instability. However, initial curved-closed geometry of microcapsule makes it more complex that the evolution of wrinkling instability might be different from the situation in planar membrane. Moreover, from the experimental point of view, the current study of wrinkling on deformable spherical particles stays in general observation, but lacks the quantitative description [10, 11], for example, wrinkling threshold and scaling laws [12]. The main drawback of existing recipes of assembling microcapsule membrane in the literature is that the tuning range of membrane mechanical properties is limited. The variation of wrinkling feature, e.g., wavelength, is not detectable. Numerical simulations allow to predict the compression region on microcapsules where wrinkling instability might happens [13], but they cannot describe the real physics of wrinkling, due to not considering the membrane bending resistance.

Another mechanical instability of microcapsules in flow is the membrane breakup. Breakup occurs at the membrane being stretched largely where it exceeds the limit of wall material to maintain the whole shape. Interfacial tension-driven liquid droplets breakup [14, 15] has been investigated well, including the threshold, surfactant modification and breakup modes, etc. However, the breakup of microcapsules governed by elastic membrane has been rarely reported. Previous work only showed tears [16] or small lobes [11] appearing near the tips of capsules at the moment of breakup. It is poorly understood that how the membrane elasticity and flow strength affect the breakup process. In application, for example drug-delivery system, the release rate is often considered as proportional to the size of microcapsules [17]. The control of post breakup is thus essential, e.g., the size distribution of daughter capsules after breakup, in the encapsulated contents release.

Therefore, the **objective** of this thesis is to understand the mechanical instabilities, such as wrinkling and breakup, of microcapsule membrane in flow, by developing a new approach of assembling microcapsules with widely tunable and controllable membrane properties, namely as the followings:

- **Developing a new strategy to assemble microcapsules**

  We dedicate to develop a new strategy for assembling microcapsules membrane with tunable rheological properties and controlled size. The stability of microcapsules in external fluid has to be paid much attention, avoiding any buckling and

swelling due to mass transfer through the membrane. The rheological properties of membrane require to be modified easily and largely. The size distribution of microcapsules can be controlled by using microfluidics.

- **Characterizing the membrane properties**

  The membrane shear resistance can be measured by immersing microcapsules in a planar extensional flow. The fluid-structure interaction (FSI) connects linearly the small deformation of capsules and flow stress, which allows us to evaluate the surface shear elastic modulus G_s. Membrane thickness can be estimated by atomic force microscope (AFM) or scanning electron microscope (SEM).

- **Understanding the process of breakup**

  Compare to droplets, we aim at investigating the effect of viscosity ratio on the threshold of breakup, using microcapsules with similar membrane shear elastic modulus. Moreover, the effect of flow strength on breakup types has to be addressed, giving a breakup phase diagram. We also try to understand the effect of capsule membrane elasticity on the threshold of breakup.

- **Understanding of wrinkling evolution**

  Flow-induced wrinkling instability involves the interplay between the membrane and flow field. To visualize the wrinkles, a set-up with two orthogonal views is required. Wrinkling features need to be quantitatively described, for example using critical stress, wavelength, and length of wrinkles, etc. We study and tune the wrinkling pattern evolution via modifying the membrane properties and flow strength, to obtain a phase diagram.

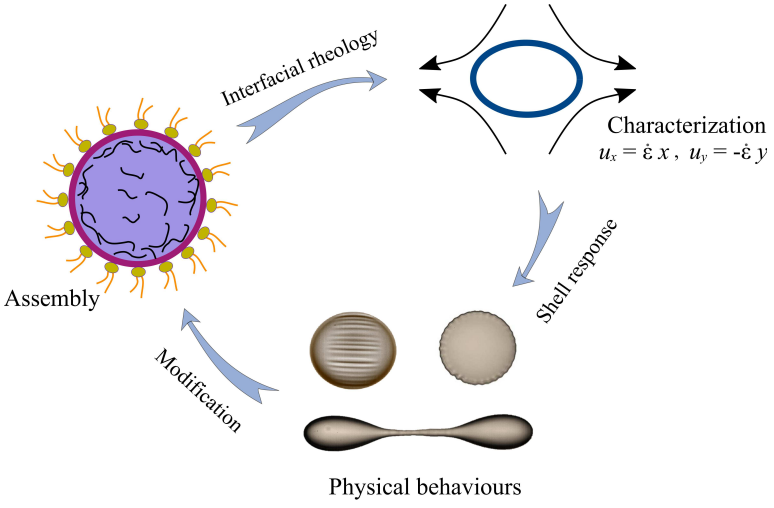

Figure 1: Study procedures of this thesis.

To achieve these objectives, we will organize the **structure of this thesis** in the following steps, mainly focusing on three parts: microcapsules fabrication, characterization, breakup and wrinkling. The sketch (Figure 1) illustrates the procedures of study in this thesis.

In **Chapter 1**, we state the basic concepts and latest investigation of microcapsules in hydrodynamic flow fields. Starting from the modelling of microcapsules, we discuss the current study on mechanical instabilities of capsules, interplaying with the flow. In addition, we remark the challenge of synthesizing microcapsules for specific purposes, for example control of instability pattern.

In **Chapter 2**, we focus on the experimental materials and methods. Microcapsules are fabricated in a decoupled water-in-oil emulsification. Drop-templates are first generated using microfludics with controlled size. Membrane assembly then starts on the template interfaces, in which membrane properties are expected to be controlled well. Capsules stabilities at rest, such as shrinking and swelling, have been paid more attention for the aim of control the prestress of the membrane. Two-view visualization set-up are developed to study the mechanical behaviours of microcapsule in flow. We estimate the membrane shear elasticity by using small deformation theory, and the membrane thickness by using AFM and SEM.

In **Chapter 3**, we present the main results of tuning membrane rheological properties. The effects of reaction time, capsule size, solution concentration and pre-stress on the membrane elasticity will be addressed, based on the method in Chapter 2. Further, in the large deformation, residual deformation and relaxation of capsules after flow cease are discussed.

In **Chapter 4**, we discuss the capsule breakup in the planar extensional flow. In contrast to droplets, we first demonstrate the interface (referred as to membrane for capsule) traction induced by the flow. General breakup modes of droplet and capsule are compared. Then, we study the effects of viscosity ratio and membrane elasticity on the critical breakup. Finally, phase diagrams and post breakup are discussed by considering the flow strength and shear elasticity.

In **Chapter 5**, we focus on the capsule wrinkling in Near-Threshold regime (NT). We quantitatively describe the emergence of wrinkling on microcapsule in the small deformation. The critical stress of wrinkling is scaled as $\sigma_c^w \sim h/R$, where h and R are the membrane thickness and capsule radius. The wavelength of well-defined wrinkles is directly measured, which follows well the scaling $\lambda_w \sim h^{1/2}$. Moreover, we discuss the wrinkles-to-folds transition when the capillary number exceeds another threshold Ca_c^f. Finally, we obtain a phase diagram of wrinkling on microcapsule in flow.

In **Chapter 6**, we extend the work of Chapter 5 by using another kind of capsule membrane material. Here, we highlight the wrinkling instability from the Near-Threshold (NT) to Far-from-Threshold (FT) regimes. Thanks to the low shear modulus of the material, a second bifurcation is discussed, where the membrane become stable again, wrinkles disappearing. We also describe the wavelength on microcapsules varying with the capillary number.

In the last, **Chapter 7**, we generally conclude our work in this thesis and propose some perspectives.

Chapter 1

State of the art: dynamics and synthesis of microcapsules

Contents

1.1 Introduction

This chapter is dedicated to reviewing the basic concepts and applications, mechanical responses and synthesis of microcapsules. Deformable microcapsules subjected in flows not only undergo global deformation and complex dynamics, but also have local shape modulations. We, here, expand the statement in the general introduction, to bring better knowledge on capsules in flows, based on the latest investigations in current literature.

1.2 Basic concepts of microcapsules

1.2.1 Scales, configuration and properties

In nature, soft capsules are commonly found in the form of bacteria, cells and eggs, etc. [5], with the scale ranging from a few nano-meters to centi-meters (Figure 1.1(a)). In contrast to rigid particles, they tend to be deformed by a small energy input. Specifically, inspired by the natural capsules, artificial microcapsules are designed using solid-like membranes to enclose contents (Figure 1.1(b)). The membrane, e.g., made of complex polycondensation, might exhibit both the features of liquid and solid under deformation.

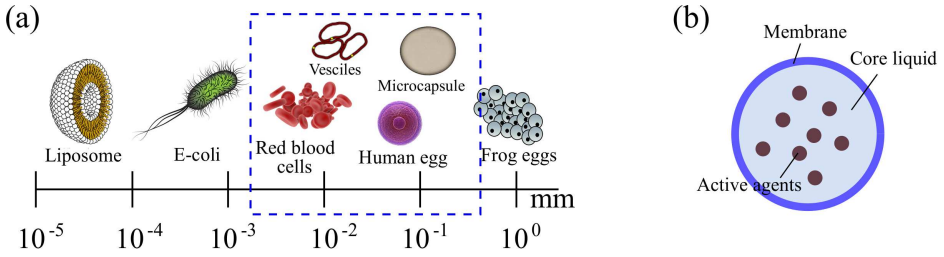

Figure 1.1: (a) Overview of soft particles scale often seen in nature. Blue dashed line indicates the general scale range used in study physical issues. (b) General configuration of a liquid-core microcapsule.

Basically, artificial microcapsules share some common properties with other soft particles, for example red blood cells (RBCs) [18] and vesicles [19]. They have, thus, received an increasing attention in physics. But, they are actually different in the composition and properties of the membranes. We briefly make a comparison here, focusing on the RBCs, lipid bilayer vesicles, and artificial capsules.

RBCs, making up 40%-50% volume of human blood, have the membrane consisting of a lipid bilayer supported by transmembrane proteins and spectrin network. On

one hand, the membrane protects the integrity of the cells when passing micro-vessels in the blood circulation [20], and functionalizes, on the other hand, the substance exchange process. It is found that the cytoskeleton (spectrin and filament) contributes to the deformability. However, due to the existence of incompressible lipid layer, the membrane surface area is considered to be constant during deformation. Thus, membrane bending can easily happens rather than stretching [21].

Vesicles are simplified configuration of RBCs, consisting of lipid bilayer. Similarly, their membrane are considered as volume- and area-incompressible. Nevertheless, different from RBCs, the bilayer of vesicles is totally free, fluid-like, leading to no fixed reference shape [22]. The shear resistance is negligible, but bending resistance has to be considered due to the binding of phospholipids molecules.

Artificial microcapsules have different membrane composition from RBCs and lipid vesicles. The membrane can be assembled by cross-linking network [23–25] or polymer absorption [26–28], around liquid droplets. The composite membrane is often considered as volume-compressible, but has resistance against the shear and dilation deformations. Since the membrane thickness is quite small compared to capsule dimension (typically, radius $R \approx 100$ μm), membrane bending resistance can be neglected in studying the overall deformation, especially in numerical simulation [13, 29, 30]. However, the bending resistance does play important roles in the local modulation of shape, such as wrinkling and folding [4, 10, 16].

Table 1.1: Comparison of RBCs, vesicles and typical artificial capsules.

	RBCs [31, 32]	**Vesicles** [33, 34]	**HSA-TC** [9, 25, 35]	**HSA-ALG** [36–38]	**OTS** [11, 39]
Thickness h [μm]	$\sim 10^{-2}$	$\sim 10^{-2}$	0.5-10	1-30	$\sim 10^{-1}$
Radius R [μm]	4-5	1-10^{2}	10-200	$\sim 10^{3}$	100-300
Shear mod. [N/m]	6-9$\times 10^{-6}$	–	10^{-2}-5	10^{-2}-5	10^{-2}-0.5
Area dilation [N/m]	$\sim$0.5	$\sim$ 0.2	0.2-6	0.2-6	0.1-1
Bending mod. [N·m]	0.4-3$\times 10^{-19}$	2$\times 10^{-19}$	10^{-16}-10^{-10}	10^{-14}-10^{-9}	$\sim 10^{-16}$

HSA-TC: capsules are made by cross linking human serum albumin with therephtaloyl chloride.
HSA-ALG: millimetric capsules are made of human serum albumin complexed with alginate.
OTS: capsules are made of n-octadecyltrichlorosilane.

In summary, we compare the physical properties of RBCs, lipid vesicles and artificial capsules in Table 1.1. It can be seen that the membrane properties of artificial capsules are determined by the wall materials.

1.2.2 Applications

Artificial microcapsules have various applications in the pharmaceutical [1, 40], cosmetic [41] and food industries [42], as well as in bioengineering [2]. Different purposes require different functionalizations of the membrane. For example, hollow microcapsules [43–45] are expected to load and release drugs or DNA for specific disease treatment. Basically, the solid-like membrane of microcaspules can isolate the core media from the environment. This would be helpful to protect some active agents that are sensitive to external surroundings, e.g., enzymes [46]. The release rate of encapsulated contents can be controlled by tuning the permeability of membrane that is sensitive to pH, temperature or ionic strength [41, 47]. In bioengineering application, for example living cells culture [48], specific substances transfer is required across the membrane. More applications of capsules can be found in the reviews [40, 49, 50].

What more interesting in physics is that microcapsules can be used to simulate the dynamics of cells (e.g., RBCs) in flows, thanks to their similar configuration and properties. In this case, it is focused on the liquid-core microcapsules subject into another immiscible fluid. For example, in shear flow microcapsules are found membrane tank-treading [51], tumbling [11] and oscillation of shape [10, 11, 52]. For the simplicity of membrane structuration of microcapsules, it brings us deeper understanding to these dynamic motions.

Whether in applications or in the study of fundamental dynamics, the challenge comes to understand and control the membrane properties of microcapsules in experiments. Numerically, the modelling of membrane is essential to describe the mechanical response of microcapsules in flow.

1.3 Modelling of capsule membrane

A microcapsule generally has a finite membrane thickness, h. Compared to the size of capsules, the thickness is quite small ($h \ll R$). For simplicity, the membrane can be considered as 2D, neglecting the bending resistance due to the thin thickness [53], in which the global deformation of capsule can be described well. However, if the membrane is thick or non homogeneous, the bending moments due to the curvature of capsule deformation play important roles [54]. The bending resistance then has to be taken into account.

1.3.1 2D membrane

In the absence of bending resistance, the transverse shear stress vanishes across the membrane. The stress tension can be replaced by the tension $\boldsymbol{T}$ at the middle plane of the membrane (defined as force per unit arc length). When stretched or compressed, the membrane only undergoes in-membrane deformation, with surface shear elastic modulus G_s and area dilation modulus K_s [13]. The tension $\boldsymbol{T}$ can be decomposed into two principal direction, T_1 and T_2.

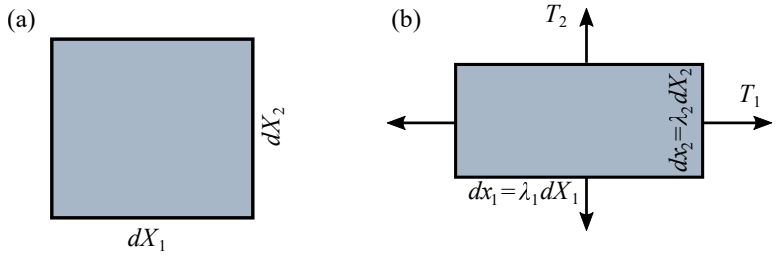

Figure 1.2: Deformation of a 2D membrane element. (a) Reference shape. (b) Deformed shape with extension ratios λ_1 and λ_2 under principal tensions T_1 and T_2 [55].

As shown in Figure 1.2, in a simple way, the deformation is related linearly with two principal extension ratios, $\lambda_1 = dx_1/dX_1$ and $\lambda_2 = dx_2/dX_2$. To describe the stress-strain relationship, several constitutive laws have been proposed [5, 56, 57]. Hooke's law (H) is used to model the elastic material for small deformation,

$$T_1^H = \frac{G_s}{1-\nu_s}\left[\lambda_1^2 - 1 + \nu_s\left(\lambda_2^2 - 1\right)\right] \quad \text{(similar for} \quad T_2^H\text{)} \tag{1.1}$$

where G_s is the surface shear elastic modulus, and ν_s is the surface Poisson ratio, between -1 and +1, and for area incompressible membrane $\nu_s = 1$. In contrast, Poisson ratio for incompressible 3D material is $\nu = 1/2$. The area dilation modulus is expressed as $K_s = G_s(1+\nu_s)/(1-\nu_s)$.

For polymeric membrane of microcapsules, a generalized Hooke's law (GH) is proposed, in which the strain energy is a quadratic function of the strain,

$$T_1^{GH} = \frac{G_s}{1-\nu_s}\frac{\lambda_1}{\lambda_2}\left[\lambda_1^2 - 1 + \nu_s\left(\lambda_2^2 - 1\right)\right] \quad \text{(similar for} \quad T_2^{GH}\text{)} \tag{1.2}$$

If the material exhibits strain-softening property, e.g., rubber-like material, a neo-Hookean law (NH) in 2D is given by

$$T_1^{NH} = \frac{G_s}{\lambda_1\lambda_2}\left[\lambda_1^2 - \frac{1}{\lambda_1^2\lambda_2^2}\right] \quad \text{(similar for} \quad T_2^{NH}\text{)} \tag{1.3}$$

This law can be used to model the behaviour of an infinitely thin membrane that is volume incompressible and isotropic. The area-dilation resistance $K_s = 3G_s$. But, the NH law can not model the area-incompressible membrane [5].

The NH law can be expanded into a general expression, referred to as Mooney-Rivlin (MR) law,

$$T_1^{MR} = \frac{G_s}{\lambda_1\lambda_2}\left(\lambda_1^2 - \frac{1}{\lambda_1^2\lambda_2^2}\right)\left[\Psi + \lambda_2^2\left(1-\Psi\right)\right] \quad \text{(similar for} \quad T_2^{MR}\text{)} \tag{1.4}$$

where Ψ is the coefficient varying between 0 and 1. For NH, the $\Psi = 1$.

R. Skalak *et al*. [58] first proposed a strain-hardening law for describing RBCs membrane behaviours. Later, taking into account material properties, D. Barthès-Biesel [56, 59] developed it as following,

$$T_1^{SK} = \frac{G_s}{\lambda_1\lambda_2}\left[\lambda_1^2\left(\lambda_1^2-1\right) + C\lambda_1^2\lambda_2^2\left(\lambda_1^2\lambda_2^2-1\right)\right] \quad \text{(similar for} \quad T_2^{SK}\text{)} \tag{1.5}$$

where C is the tuning parameter for membrane area incompressibility. For example, the red blood cell membrane has a bilayer lipid which is almost area incompressible but easy to shear. In this case, the coefficient is often assumed as $C \gg 1$.

Indeed, capsules with different wall materials exhibit different stress-stain relationships. A comparison of different constitutive laws can be found in the reference [56], in large deformation. Y. Lefebvre *et al*. [60] and X.-Q. Hu *et al*. [61] compared the NH and SK laws effects on the HSA capsule flowing in the cylindrical and square-section microchannels with numerical and experimental studies. It shows that the NH law is more appropriate to model the albumin capsule. However, de Loubens *et al*. [57] found that the GH law describes the HSA capsules well in an extensional flow. In the limit of small deformation, all the constitutive laws reduce to the Hooke's law.

Experimentally, artificial microcapsule membrane might not be perfectly elastic, but may be with a contribution of viscosity. A dimensionless number is defined to describe the viscosity and elasticity,

$$\chi = \frac{\eta_m\dot{\gamma}}{E_s} \tag{1.6}$$

where η_m is the membrane shear viscosity, and $\dot{\gamma}$ is the shear rate. E_s is 2D Young's modulus, $E_s = Eh$, for homogeneous material. In numerical simulation, the viscous term is linearly added in the elastic tensors, more details seen in the references [62, 63].

Note that the 2D membrane assumption has been widely adopted in simulation, where the bending resistance is often neglected [13, 64, 65]. It gives an acceptable accuracy for studying the general deformation, but cannot describe the membrane out-of-plane deformation, for example wrinkles.

1.3.2 3D membrane

For a thick membrane, the transverse shear forces across the membrane can not be considered as homogeneous. The produced tangential bending moments are not negligible [66, 67]. The developing of bending moments make the 3D membrane with flexural stiffness, which is correlated to the bending modulus, B. Although the bending modulus has a few orders of magnitude smaller than the surface shear modulus, the bending resistance is believed to play central roles in determining the curved configuration at equilibrium for soft particles, for example biconcave RBCs [22].

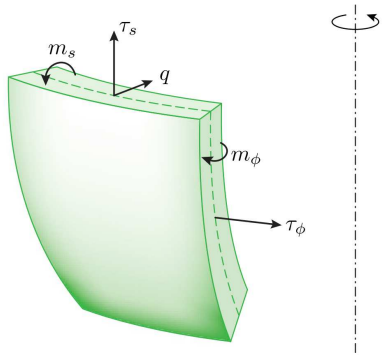

Figure 1.3: Schematic of tensions and bending moments on an element of curved capsule membrane [66].

As illustrated in Figure 1.3, when the membrane is bent, it produces the in-plane tension $\boldsymbol{\tau}$ which requires $\boldsymbol{n} \cdot \boldsymbol{\tau} = 0$. In the circumferential direction, the tensor can be described as τ_s and τ_ϕ. The transverse shear tension is described as a vector $\boldsymbol{q}$, acting on the cross section of the membrane. The bending moment tensor is named as $\boldsymbol{m}$. Like elastic tension, the transverse shear tensions and bending moments are required to have no normal component, lying in the tangential plane, namely $\boldsymbol{q} \cdot \boldsymbol{n} = 0$ and $\boldsymbol{m} \cdot \boldsymbol{n} = 0$. Thus, the full tension tensor, including the tangential and transverse shear tensions, can be written as

$$\boldsymbol{T} = \boldsymbol{\tau} + \boldsymbol{q}\boldsymbol{n} \tag{1.7}$$

where the transverse shear tensor is expressed as $\boldsymbol{q} = (\boldsymbol{\nabla} \cdot \boldsymbol{m}) \cdot (\boldsymbol{I} - \boldsymbol{n}\boldsymbol{n})$. The bending moment tensor is related to the local curvature and the bending modulus. The detailed formulations can be found in reference [67]. To close the problem, constitutive laws in 3D is required. Strain-energy function is useful to deduce the tension tensor [67, 68].

A membrane without bending resistance might form corned shape, showing no curvature. In contrast, with the presence of bending resistance, the membrane has a reasonable curvature, after achieving the minimum energy. In this case, the final shape

is the competition result of in-plane stress tension, bending resistance and external forces.

1.4 Capsules in flows

Soft particles exhibit spatiotemporal deformation when they are exposed to external stress field, for example in a hydrodynamics flow field. Since the flow generally has low Reynolds number ($Re < 1$), it is governed by the Stokes equation. Flow stress imposes traction on the membranes to deform the particles. Meanwhile, complex dynamics might be coupled. In the past decades, an extensive number of studies have been carried out on RBCs [18, 33], vesicles [22, 69] and artificial capsules [5, 11, 57, 70, 71] in flows, via both experiments and numerics. In this section, we review the flow-structure interaction induced deformation and the general dynamics of capsules in shear and extensional flow.

1.4.1 Deformation

Initially, we consider a three-dimensional spherical capsule with a thin elastic membrane enclosing a Newtonian fluid, subjected in another Newtonian fluid, with viscosity ratio λ_η (defined as the viscosity of internal to external) (Figure 1.4). The capsule is identified by an undeformed radius R and membrane thickness h. Since no mass exchanges across the membrane, the volume of capsule, $V = 4\pi R^3/3$, preserves constant during the deformation. For a real membrane material, a capsule owns finite shear resistance (G_s), bending resistance (B) and area-dilation resistance (K_s) [70].

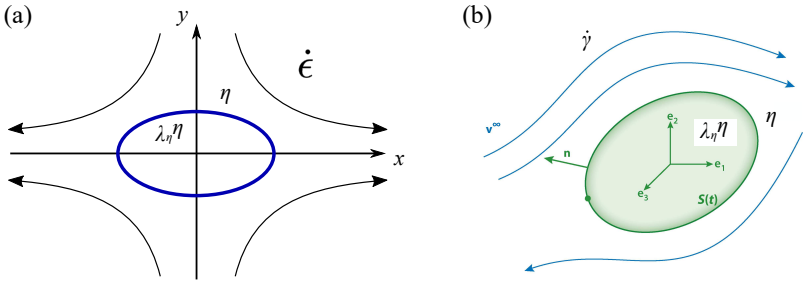

Figure 1.4: Schematic of a capsule deformed in flow. (a) Planar extensional flow. (b) Linear shear flow [5]. Here, the viscosity ratio between inside and outside the capsule is denoted as λ_η. $\dot{\epsilon}$ and $\dot{\gamma}$ are extension rate and shear rate of the flows, respectively.

The microcapsule is deformed by a flow governed by Stokes equation, $\nabla p^{(\alpha)} = \eta^{(\alpha)}\nabla^2 \boldsymbol{u}^{(\alpha)}$, where $\alpha = in$ or ex. In the absence of capsules, the flow field has the velocity

gradient tensor [3],

$$\nabla \boldsymbol{u} = \frac{1}{2}\dot{G}\begin{bmatrix} 1+\alpha & 1-\alpha & 0 \\ -1+\alpha & -1-\alpha & 0 \\ 0 & 0 & 0 \end{bmatrix} \tag{1.8}$$

where $\boldsymbol{u}$ is the undisturbed velocity, $\dot{G}$ is the strain rate, and α is the parameter to determine the flow types. For example, α = 1 is corresponding to the planar extensional flow, α = 0 for simple shear flow, and α = -1 for purely rotational flow. To be clear, we denote strain rate $\dot{G} = \dot{\epsilon}$ in the extensional flow and $\dot{G} = \dot{\gamma}$ in the shear flow.

The hydrodynamic load applied on membrane is due to the jump of viscous traction, $\boldsymbol{\Delta f} = (\boldsymbol{\sigma}^{ex} - \boldsymbol{\sigma}^{in}) \cdot \boldsymbol{n}$, in the thin-membrane system. For the membrane without bending resistance, the elastic tension $\boldsymbol{T}$ in membrane caused by deformation is balanced by the load [13],

$$\boldsymbol{\nabla_s T} + \boldsymbol{\Delta f} = 0 \tag{1.9}$$

where $\boldsymbol{\nabla_s}$ is the gradient in membrane surface. For both incompressible fluid inside and outside the capsule, it follows the continuity equation, $\nabla \cdot \boldsymbol{u}^{(\alpha)} = 0$. However, for the membrane considering the bending resistance, the tension tensor, $\boldsymbol{T}$, in Equation 1.9 is replaced by the Equation 1.7. In deformation, it meets the boundary conditions. There is no flow perturbation in the field far from the capsule, $\boldsymbol{u}^{ex}(\boldsymbol{x}, \boldsymbol{t}) \to \boldsymbol{u}^{\infty}$. At the interface, the velocity is continuous, $\boldsymbol{u}^{ex} = \boldsymbol{u}^{in}$. The interface velocity at a point can be determined from a boundary integral equation [5, 64].

In numerics, combining boundary conditions and constitutive laws, solving the fluid equations and solid equations gives the tracking of capsules boundaries in flows [13]. Experimentally, G. I. Taylor [72] first studied the droplets deformation in the Four-roller and Parallel-band devices. Similarly, for capsules, a parameter that describes the deformation is named as Taylor parameter,

$$D = \frac{L - S}{L + S} \tag{1.10}$$

where L and S denote the semi-major and semi-minor axis lengths of the deformed capsule. In the small deformation, an asymptotic solution has been developed by D. Barthès-Biesel [5, 68] for initially spherical capsules suspended in Stokes flow. The deformation of capsule in shear flow or extensional flow is thus connected with hydrodynamic stress by

$$D = \frac{5}{2(k+1)} \frac{2+\nu_s}{1+\nu_s} \frac{\eta \dot{G} R}{G_s} \tag{1.11}$$

where k = 0 and 1 are corresponding to planar extensional flow and shear flow, respectively. η is the viscosity of external fluid (here $\eta = \eta_{ex}$). R is the radius of undeformed

capsule and G_s is the surface shear elastic modulus, and $\dot{G}$ is the strain rate of fluid. In shear flow, this theoretical prediction is limited in the case of large viscosity ratio ($\lambda_\eta >$ 5) [73]. In the extensional flow, the viscosity ratio has no effect because the membrane and the internal fluid are motionless at the steady state of deformation.

A dimensionless number that describes the competition between viscous stress and elasticity of membrane, is often defined as the capillary number

$$Ca = \frac{\eta \dot{\epsilon} R}{G_s} \quad \text{or} \quad Ca = \frac{\eta \dot{\gamma} R}{G_s} \tag{1.12}$$

for extensional flow and shear flow, respectively. By assuming the surface Poisson ratio $\nu_s = 0.5$, Equation 1.11 is often used to evaluate the membrane shear elasticity via direct measurement of the global deformation and flow stress [3, 11, 25, 71].

1.4.2 Dynamics

Soft deformable particles are found to show complex behaviours under flows [6, 51, 74, 75]. For example, in a shear flow a particle might exhibit tank-treading motion (TT) in which the membrane rotates around the core medium with almost the same inclination angle to the flow streamline, tumbling motion (TU) in which it moves like a rigid body, flipping continuously, and swinging motion (SW) in which the deformation and the inclination oscillate around positive values, seen in Figure 1.5. Due to the biconcave configuration of RBCs, the rolling motion might happen, exhibiting like a wheel rotation with a center axis perpendicular to the shear plane [7, 18]. In some cases, the TT may co-exist with SW both for vesicles and RBCs.

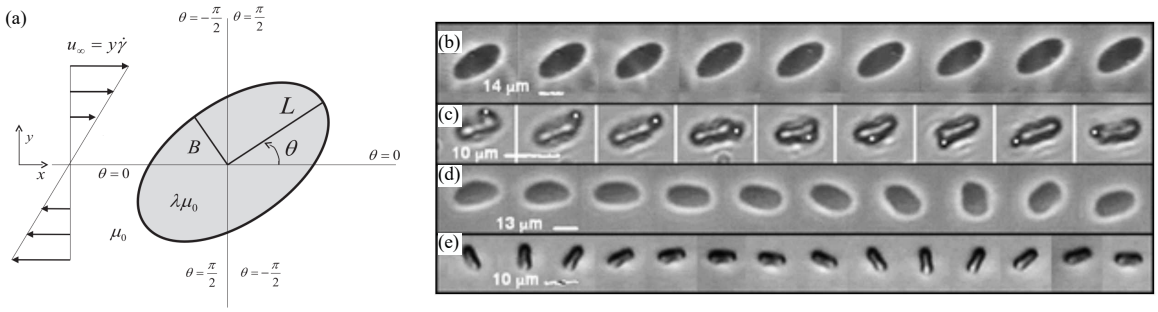

Figure 1.5: Dynamics of deformable particles in shear flow. (a) Schematic of a particle suspended in lineaer shear flow [76]. (b) Tank-treading vesicles. (c) Tank-treading accompanied with swinging motion of RBCs. (d) and (e) are tumbling motion of vesicles and RBCs, respectively [22].

In the early stage, T. M. Fischer *et al*. [77] studied the frequency of tank-treading behaviour by decorating the RBCs membrane with Latex particles in simple shear flow.

Inspired by RBCs, Keller & Skalak [78] considered an initially ellipsoidal geometry in shear flow, and predicted the tank-treading and tumbling motions as function of the shape and viscosity ratio. Later, many experimental [79, 80], theoretical [74, 81] and numerical [70, 82] works on dynamical motions of vesicles and RBCs have been boosted. These studies reveals that the transition between different motions is dependent not only on the shear rate and the viscosity ratio, but also on the membrane viscosity [82].

In shear flow capsules have been predicted to show the oscillation of deformation and orientation, particularly to the viscoelastic membrane, as a function of the parameter χ,

$$\theta = \frac{1}{2}\arctan\frac{\chi^2 + 5/9}{2\chi(\chi^2 + 7/9)} \tag{1.13}$$

where we can see the orientation varies between 0° and 45°. This has been qualitatively verified by nylon capsules in a Couette flow [16]. If the $\chi \to 0$ where it is the purely elastic membrane, the inclination angle $\theta \to 45°$.

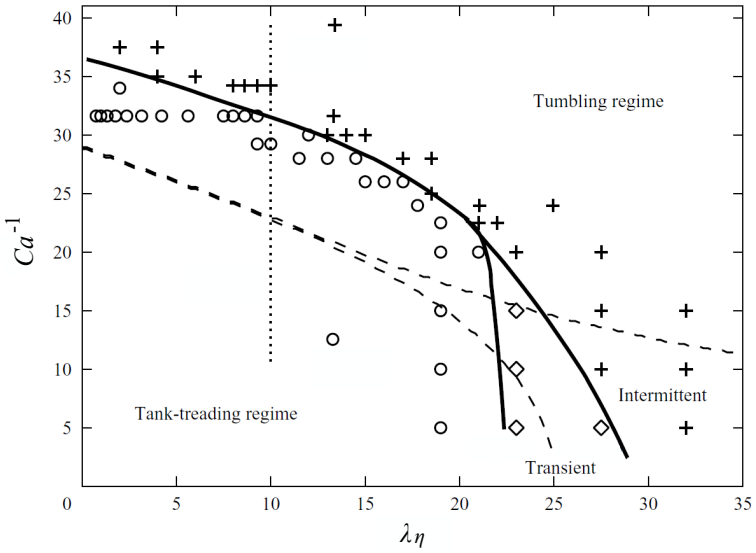

Figure 1.6: Phase diagram of an elastic capsule motions in shear flow [6]. Circles: tank-treading; Crosses: tumbling; Diamonds: transient region.

The membrane viscosity is correlative to the frequency of the membrane TT motion due to the viscous dissipation. Boussinesq number (Bq) is defined as the ratio of membrane viscosity to the external fluid viscosity.

$$Bq = \frac{\eta_m}{\eta_{ex} R} \tag{1.14}$$

For pure elastic membrane ($Bq \ll 1$), the orientation θ is fixed at 45°. However, for the viscoelastic membrane, the particles might do not exhibit steady state, while showing

continuous inflation and deflation, accompanied by a periodic variation of the orientation between -45° and 45° [62].

For capsules, a full description of dynamical motions has been reported numerically in Figure 1.6. However, there are only a limited number of experimental investigations. Probably the SW motion was first experimentally observed on elastic capsules by Chang & Olbricht [16] in a Couette flow. Later, TU and SW motions were characterized on polysiloxane capsules in the group of H. Rehage [10, 11, 75, 83]. By decorating the albumin membrane with iron oxide powder, de Loubens *et al*. [51] investigated the TT motion of capsules with $\lambda_\eta = 1$ in large deformation. The difficulties in experiment, for example the control of membrane rheological properties and visualization techniques, may limit the number of experimental studies for capsules.

To summarize this section:

- At equilibrium, the deformation of soft particles in flow is the result of competition between the flow stress and membrane tensions.
- The dynamical motions of deformable particles in shear flow have been understood well. Capillary number Ca and viscosity ratio λ_η play essential roles in the motions transition.

1.5 Capsule wrinkling in flows

In the previous section, we have reviewed the global deformation and dynamical motions of deformable particles, e.g., artificial capsules, in flows. It is well understood that the membrane rheological properties and flow types govern the responses of capsules. There also exist locally self-organized shape modulations on capsules in these flows, for example wrinkling and breakup instabilities. First, we review the current works on capsule wrinkling instability in flows.

1.5.1 A brief review

Starting from RBCs, it has been repoted that RBCs membrane with chemical modification (e.g., diamide treatment) is more susceptible to be buckled than to be elongated with only in-plane deformation, when they are sheared [8, 84] (illustrated in Figure 1.7). Natural RBCs, however, do not show buckling in shear flow. The difference is attributed to the modification of membrane shear resistance. Chemical treatment increases the cellular membrane shear modulus in several orders of magnitude. When deformed, the membrane requires much more energy for stretching. Bending the membrane, however, requires less energy. In Figure 1.7(c), we can see that the buckling wavelength has approximately the same order of magnitude as the cell diameter (≈ 8 μm).

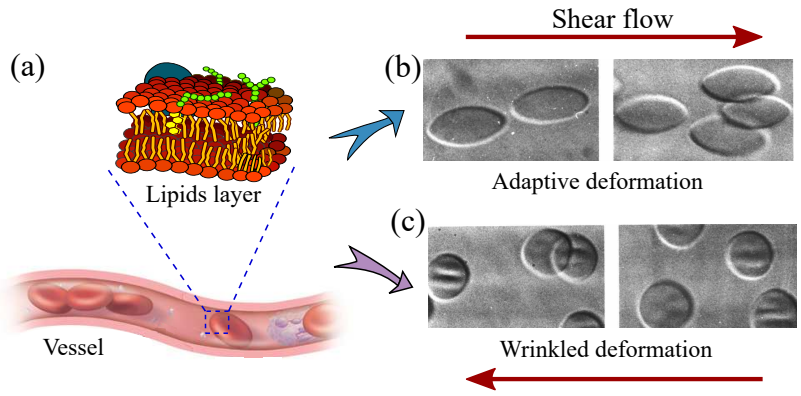

Figure 1.7: Healthy human red blood cells in flow. (a) Red blood cell membrane structure and flowing in blood microcirculation. (b) Large deformation of natural red blood cells in shear flow. (c) Rigidity modification of red blood cells membrane with 0.1 mM diamide or 0.1 mM 4,4'-dithiodipyridine treatment in shear flow. Wrinkles appear during the deformation. (from reference [8])

Similarly, artificial capsules with thin membrane have been reported wrinkling in a confined flow. V. Seshadri *et al*. [4] first observed the periodic wrinkles on capsules flowing in a round capillary. Later, a theoretical analysis was proposed by T. W. Secomb *et al*. [85], considering the elastic properties of membrane. It is found that there exists a compression region at the rear of the deformed capsule in capillary. More recently, J. Gubspun [9] designed a two-view visualization set-up to observe directly the wrinkling profile of capsules both in round and square capillaries. Wrinkles are found at the rear rather than the front, which confirms the theory in reference [85]. Well-defined wrinkles were observed (Figure 1.8(d)). These observations are significant, but lacking quantitative description for the wrinkling instability on capsules.

Experimentally, capsule wrinkling also have been reported in the shear flow. Walter *et al*. [10] first used a rheoscope (consists of a Couette geometry and fast camera) to observe the wrinkles on polyamide and polysiloxane capsules (Figure 1.8(a)). They also used an interfacial rheometer to explore the 2D storage modulus $\mu^{'}$ for the membranes, and found that elasticity seems to be an important criterion governing the wrinkling phenomenon. Later, in the same group, they experimentally observed OTS capsule wrinkling using the same device [11, 52, 75] (Figure 1.8(b)). However, due to small wavelength of wrinkles and low magnification of the images, it is difficult to obtain the accurate wrinkling features (e.g., wavelength and wavenumber). The pre-stress in the membrane induced by osmotic pressure might change, due to the solubility of water in oil (OTS capsules were made in O/W emulsification). Water might transfer into the oil phase, inflating the capsules. Consequently, the membrane is under stressed. In their experiments, wrinkling was not observed if the oil phase contains a small quantity of water. In summary, these formulations of fabricating capsules do not allow to obtain the insights of wrinkling in a repeatable and quantitative way.

Since experimentally it is difficult to study wrinkling on microcapsules, numerical simulation were carried out by other researchers. Lac *et al*. [13] performed numerical simulation of capsules with different constitutive laws subjected into simple shear flow and elongation flow. It is found that when the $Ca < Ca_L$ negative stress is easy to occur (Figure 1.8(c)), predicting the region where wrinkles might appear on capsules. A. Yazdani *et al*. [63] considered the influence of membrane viscosity on the negative stress distribution. For example, membrane with $Bq \gtrsim 10$, $\lambda_\eta = 1$ and Skalak model ($C = 1$) are observed distortion in shear flow, which modified the distribution of negative stress. Moreover, pre-stress in membrane [13, 86] and high viscosity ratio [30, 63] have been proposed to prevent compression appearing on capsules in shear flow. Initial stress in membrane compensates the negative tension during deformation, resulting in the surface under stretching everywhere.

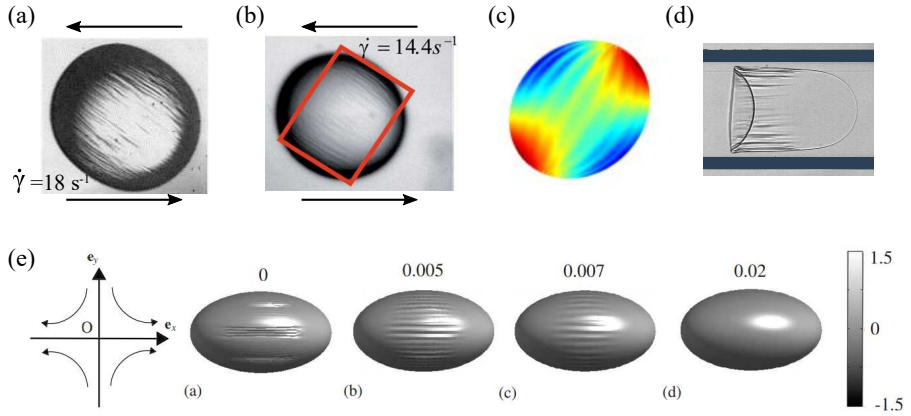

Figure 1.8: Wrinkling on artificial microcapsues in flows. (a) Membrane folding of polysiloxane microcapsule at shear rate $\dot{\gamma}$ = 18 s^{-1}, radius R = 343 μm [10]. (b) Well-organized wrinkles on polysiloxane microcapsule at shear rate $\dot{\gamma}$ = 14.4 s^{-1}, radius R = 163 μm [11]. (c) Capsule with NH membrane showing tensions distribution in shear flow at Ca = 0.0375 [13]. Colours: red means under tension, while blue means under compression. (d) Albumin capsule developing wrinkles at the rear in a capillary flow [9]. (e) Membrane stability of capsule considered relative membrane thickness in a planar hyperbolic flow. From left to right the thickness h/R = 0, 0.005, 0.007 and 0.02 respectively [87].

Up to now, the numerical investigations we reviewed above did not take into account the capsule membrane bending resistance. The prediction of wrinkling is only based on the negative stress distribution, which is not the physical instability phenomenon. Recently, Dupont *et al.* [87, 88] numerically considered a capsule with a given thickness made of a three-dimensional homogeneous material in shear and extensional flow. This is more close to the real system. They found that the wavelength is corresponding to the shell thickness, $\lambda_w \sim \sqrt{hR}$ at the middle of surface. Thus, it is possible to prevent the wrinkling by increasing the wall thickness (Figure 1.8(e)). However, in shear flow, wrinkles might be streamed as the membrane rotates (tank-treading), which makes it more complex to characterize [89].

In spite of the wrinkling on capsules observed in experiments and predicted by numerical simulations, the understanding of wrinkling threshold and evolution on capsules are still lacking. Finken & Seifert [12] derived analytical results both for threshold value of the shear rate, $\dot{\gamma}_c \sim \sqrt{BE_s}/(\eta R^2)$, and for critical wavenumber of wrinkling, $k_c \sim 1/\sqrt{hR}$, where B is the bending stiffness and E_s is the 2D Young's modulus of isotropic material, $E_s = Eh$. In a confined flow, the critical capillary number of wrinkling Ca_c is found decreased with the confinement (defined as a ratio of capsule size to capillary diameter) [9].

1.5.2 Wrinkling energies

The thin surfaces or layers undergo wrinkling when they are exposed to external constraints such as compression [90, 91] or to internal strains such as growth [92, 93]. Physically, a membrane might wrinkle when under compression or transverse shrinkage induced by stretching due to Poisson ratio of material. In this case, the membrane is often assumed not being able to support any negative stress during deformation [94].

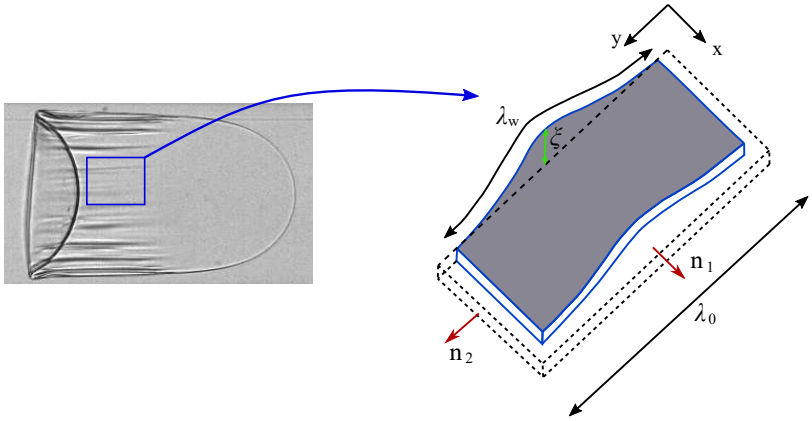

Figure 1.9: Schematic of a membrane wrinkling. Left image of wrinkling capsule is from the reference [9].

Taken into account an element of the membrane (Figure 1.9), it is stretched in the $\boldsymbol{n_1}$ direction by flow stress. Spontaneously, it induces transverse compression in the $\boldsymbol{n_2}$ direction. Based on the assumption above, when the principal stress in $\boldsymbol{n_2}$ direction reaches below zero, the membrane will form out-of-plane deformation, wrinkles appearing.

Energetically, wrinkling occurrence on a surface with small thickness, h, involves three energies (Equation 1.15): stretching energy U_s, bending energy U_b and the energy U_m due to membrane itself constraints [95, 96].

$$U = U_s + U_b + U_m \tag{1.15}$$

At equilibrium, we assume the membrane having a small deflection ξ, thus leading to the energies, stretching $U_s = \frac{1}{2}\int_A T(x)\left(\frac{\partial \xi}{\partial x}\right)^2 dA$, bending $U_b = \frac{1}{2}\int_A B\left(\frac{\partial^2 \xi}{\partial y^2}\right)^2 dA$, and adding $U_m = \int_A f(x)\left[\frac{1}{2}\left(\frac{\partial \xi}{\partial y}\right)^2 - \frac{\Delta(x)}{W}\right] dA$, where A is the surface area, and W is the characteristic width. $f(x)$ is an unknown multiplier. For a sheet under uniaxial stretching, $T(x) \sim Eh\gamma$ and $\Delta(x) \sim \nu\gamma W$, where γ is the tensile strain. By minimizing

the total energy $\frac{\partial U}{\partial \xi} = 0$, it yields Foppl-von-Kármán (FvK) equation

$$B\frac{\partial^4 \xi}{\partial y^4} + T(x)\frac{\partial^2 \xi}{\partial x^2} - f(x)\frac{\partial^2 \xi}{\partial y^2} = 0 \tag{1.16}$$

With a small transverse compression, the membrane also satisfies the following relationship,

$$\int_0^L \left[\frac{1}{2}\left(\frac{\partial \xi}{\partial y}\right)^2 - \frac{\Delta(x)}{W}\right] dy = 0 \tag{1.17}$$

which indeed contributes in the term of U_m. Finally, a general scaling law that describes wrinkling far from the boundary constraints is thus obtained by solving above equations with some conditions (details in reference [96]),

$$\lambda_w = 2\sqrt{\pi}\left(\frac{B}{T}\right)^{1/4} L^{1/2} \quad \text{and} \quad A = \frac{\sqrt{2}}{\pi}\varepsilon^{1/2} \tag{1.18}$$

where λ_w and A_w are wavelength and amplitude, respectively. Note that the compressive strain $\varepsilon = \nu\gamma$ for an isotropic material. This work also has been found in good agreement for membrane floating on a liquid substrate [90, 97].

To summarize this section:

- Negative stress induced by compression in membrane determines the wrinkling instability.
- Numerical simulation not considering bending resistance allows to predict the compression on capsules in flow.
- Experimentally, wrinkling is observed qualitatively on capsules, but lacks the quantitative description, e.g., critical wrinkling and wrinkles development.

1.6 Capsule membrane breakup

Another mechanical instability of capsules in flow is the membrane breakup. When the flow stress exceeds the limit of wall material, membrane rupture occurs. Understanding the membrane breakup process of capsules plays important roles for the design and control of drugs in the delivery systems. For instance, artificial capsules used for drugs delivery [47, 98, 99], release the drugs either by continuous diffusion with controlling membrane permeability, or by sudden membrane breakup. The release rate is often considered as proportional to the size of capsules [17].

A simple picture is that a single microcapsule immersed in another viscous fluid is deformed up to breakup by an extensional or shear flow [3, 16]. If the encapsulated phase is conductive, the deformation and breakup may be achieved in an electric field [100]. Indeed, the breakup of drops that dominated by the interfacial tension in hydrodynamic flows and electric field have been investigated well, for example the famous Grace Curve that describes critical breakup [14, 101]. In contrast, to our knowledge there are very limited number of studies on elastic microcapsules breakup either in hydrodynamic flow or in electric field.

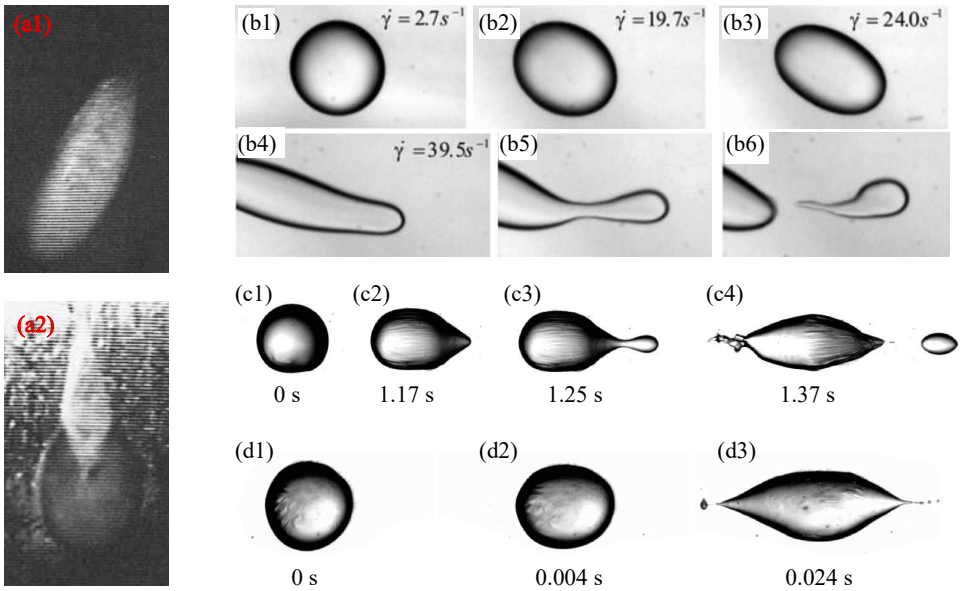

Figure 1.10: Artificial capsules breakup types. (a1)-(a2) Tear formation on nylon millimetric capsule, imaged in two views, in shear flow [16]. (b1)-(b6) A polysiloxane capsule in shear flow at different shear rates [11]. Small lobes form near the tips at high shear rate. (c1)-(c4) Capsule breakup at $Ca \approx Ca_c$ in an electric field. (d1)-(d3) Capsule breakup at very high capillary number $Ca \gg Ca_c$ in an electric field. [100].

Experimentally, D. Barthès-Biesel [102] compared the breakup of droplets and capsules in elongation flow. With the same viscosity ratio, the polylysine capsules exhibited pointed ends. Thereafter, the membrane was broken by ejecting small droplets of the internal fluid. This is different from the membrane breakup observed on nylon capsules in a shear flow (Figure 1.10(a)) [16]. The breakup of nylon capsule occurs when a thin strip of membrane appears near the tip, followed by a tear growing. Consequently, the capsule was broken into two pieces. Thinning of local membrane during the deformation could give an explanation for this rupture process. But, it is difficult to measure directly the thickness variation at th moment of breakup. Unlike the thick membrane of nylon capsules, polysiloxane capsules [10, 11, 83] have ultrathin membrane which were observed rupture at the tips but with detaching small lobes in a shear flow (Figure 1.10(b1-b6)). Similar breakup of polysiloxane capsules in a uniform electric field was also observed when the capillary number is close to the critical value ($Ca \gtrsim Ca_c$). While, if the applied electric field intensity is initially much higher than the critical one ($Ca \gg Ca_c$), the membrane breaks by ejecting a set of very tiny daughter capsules (Figure 1.10(c1-d3)). In a spinning-drop apparatus, it is also reported that breakup could happen at the poles of deformed capsules [103], which is in good agreement with the theoretical prediction that maximum elastic tension happens at the poles.

Numerically, X. Li *et al*. [89] and Lac *et al*. [13] found that there exists large compressive stress near the tips of capsules, causing buckling, when they are exposed to a shear flow with large capillary number (e.g., $Ca > 1$). The compression might arise from the torque induced by the vorticity of shear flow. E. Foessel *et al*. [30] argued that the compression on capsule shifts from the center towards the tips with the increase of capillary number in shear flow.

Several mechanisms of capsule breakup have been suggested by experiments [16] and simulations [13, 53, 89, 104], namely membrane thinning, excessive tension and tip-buckling. To our knowledges, all the types of breakup, observed in previous studies, happen near the tips of capsules. Membrane thinning induced failure seems to be more reasonable for polymerized capsules. Under deformation, the membrane is stretched in plane, but meanwhile it decreases the thickness. Breakup occurs most likely at the point where the membrane has smallest thickness. However, in practice, the breakup of artificial capsules in flows is complicated, due to their unknown membrane rheology.

In flow, interfacial tension-driven droplets have been observed several types of breakup: bulbous (BU), cylindrical (CY), tip steaming (TS) and stretched tip streaming (STS), illustrated in Figure 1.11. However, it is poorly understood that how capsules membrane break in hydrodynamic flows. For capsules, there exist several difficulties

to study the breakup. First, it is challenging to prepare the same batch of capsules having the same rheological properties. Second, the viscosity ratio of capsules is difficult to adjust in a large range, without changing membrane properties, but also considering the balance of density (no buoyancy force). Third, it requires appropriate models to describe the capsule deformation at breakup, concerning the elasticity of membrane.

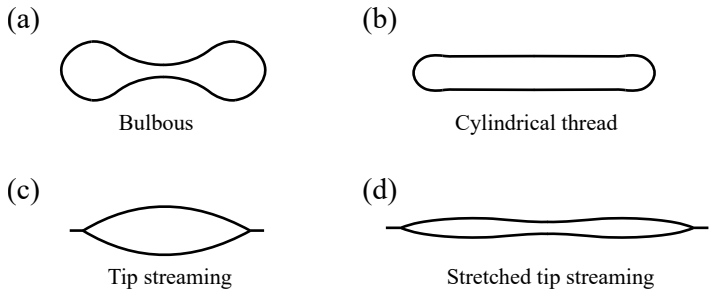

Figure 1.11: Schematic of a droplet breakup modes in a hyperbolic extension flow.

To summarize this section:

- Experimentally and numerically, capsule breakup in flows is found to happen near the tips.
- Viscosity ratio and flow strength are rarely reported on the breakup process for capsules in flows.
- It has few quantitative understanding for capsule breakup in flows, due to the poor controlling in membrane rheology.

1.7 Synthesis of microcapsules

To study the mechanical responses of microcapsules in flows, experimentally the first thing comes to the synthesis of microcapsules. The types of microcapsules are diverse [44, 48, 105] in various purposes. However, in this section, we only focus on the synthesis of microcapsules with liquid internal contents, used for the suspension study. Liquid-core encapsulation generally involves two steps: two immiscible phases emulsification forming droplets, then polymerization occurring around the droplets forming membrane [106]. Parameters such as size and shape, properties such as membrane rheology, morphology and stability should be paid attention.

1.7.1 Liquid cores formation

The first step is the droplets formation using different immiscible phases. Conventional approaches (Figure 1.12(a)), for example static mixing [1, 107], high-pressure valve homogenizing [108] and electrospray [109, 110], are expected to have high efficiency in generation of droplets, which can meet the industrial requirement. However, the size of droplets is polydisperse due to exposure of produced droplets into the non-uniform shear or pressure field that might break a large droplet into several daughter droplets [111]. Recently, the emulsification of injecting a disperse phase into a continuous phase through a membrane where there exist micropores with a certain spacing array, provides a high production rate for droplets formation with size dispersity CV = 10-20% [112, 113] (Figure 1.12(b)).

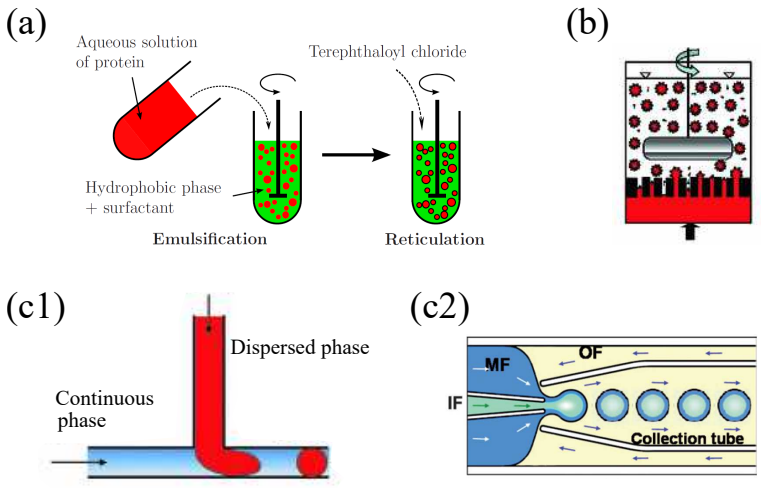

Figure 1.12: Liquid-liquid droplets formation based on immiscible phases emulsification. (a) Static agitation [107]. (b) Cell-membrane emulsification [113]. (c1) T-junction microfluidic chip [113]. (c2) Flow-focusing microfluidic chip [114].

Microfluidic approach alternatively provides a facile way to produce monodisperse droplets with $CV < 3\%$. Single or double emulsion can be achieved in a T-junction or flow-focusing configuration of microfluidic chip (Figure 1.12(c)), by controlling the mixing of immiscible phases. The drawback for a single-channel microfluidic chip is that the production rate is limited by the flow rates. To overcome that, a cluster of microchannels array is required [115], but with size distribution $CV < 10\%$.

1.7.2 Membrane formation

The second step of encapsulation comes to membrane formation around the liquid droplets by interfacial polycondensation or solidification [28], with presence of functional chemicals. This process generally can be classified into two categories: chemical cross-linking and physical electrostatic absorption [116].

Chemical cross-linking: The interfacial reaction takes place at the liquid-liquid interface when the functional chemicals contact each other. This polymerization can be achieved by chemical bonds connection such as hydrogen bonds and hydrolysis. One kind of chemical with high mobility aggregates with the special groups on another one, forming cross-link network, for example chlorides cross-linked with amino groups in protein [23, 117]. Typical capsules, such as nylon capsules [3], OTS capsules [11, 83] and albumin capsules [25] are made in this strategy.

Electrostatic absorption: Polyelectrolyte membrane can be formed by depositing negative layers onto positive layers or reversely, at the interface through electrostatic absorption [28, 118]. In this regard, layer-by-layer (LbL) assembly is achieved with precisely controlled thickness and structure [26], but the process is complicated and time-consuming. Since the bonding strongly depends on the chargeability of chemicals, the membrane may then be damaged by, for example tuning pH values and ionic strength.

1.7.3 Rheological properties

Combination of the droplets generation and membrane assembly permits the synthesis of liquid-core microcapsules. However, it is still a challenge to balance the tuning of membrane rheological properties and size distribution. For example, ejecting oil phase and water phase with functional chemicals in a microfluidic chip allows to produce microcapsules with well-controlled size distribution, but the membrane polycondensation time is strongly limited by the residence time of microcapsules in microchannels of the chip (maximum a few minutes) [119, 120]. Consequently, it is difficult to obtain the microcapsules with thicker membrane. Decoupling the droplets generation and

membrane formation makes it more flexible to tune the rheological properties of membrane.

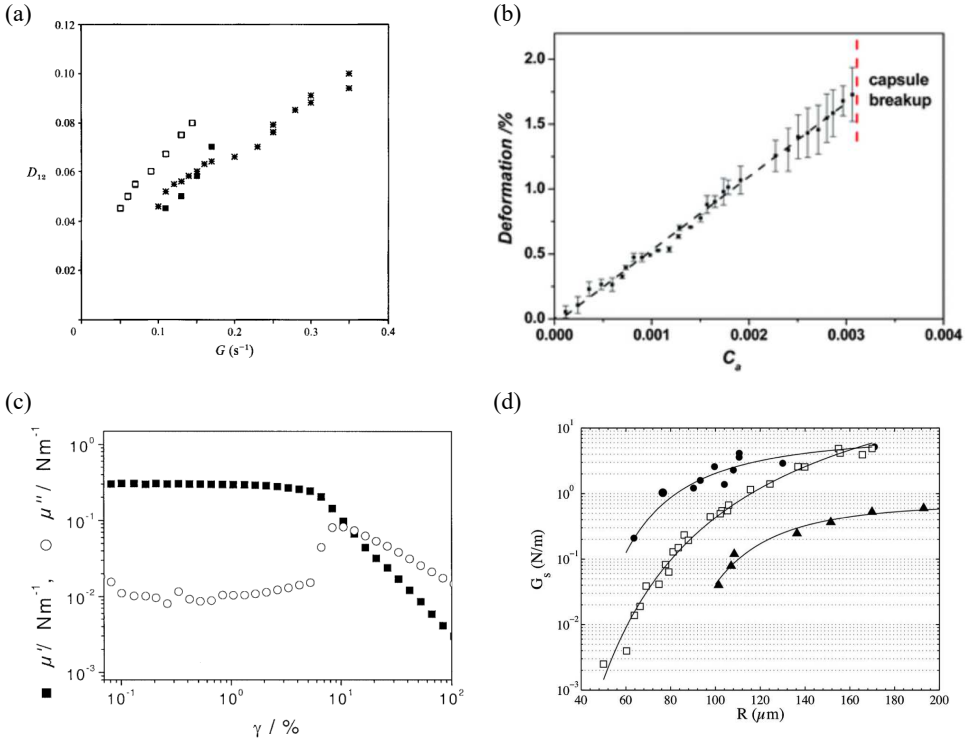

Figure 1.13: Rheological properties of artificial microcapsules membrane. (a) Taylor parameter (defined as Equation 1.10) as a function of shear rates for different nylon capsules fabricated in the same batch [3]. (b) Taylor parameter of polysiloxane microcapsules as a function of Ca number (defined as Equation 1.12) [11]. (c) Elasticity $\mu^{'}$ and viscosity $\mu^{''}$ of flat polysiloxane membrane as a function of the strain amplitude γ [39]. (d) Surface elastic modulus G_s as a function of radius R of HSA microcapsules. Circles: 20% HSA; Squares: 10% HSA; and Triangles: 5% HSA [25].

K. S. Chang *et al.* [3] fabricated millimetric capsules by dripping sebacoyl chloride (in oil phase) droplets into diethylene triamine solution (in water phase), and characterized them in a four-roll mill extensional device. Different capsules exhibited various deformation under the same shear rate (Figure 1.13(a)), which means that capsules produced in the same batch have different mechanical properties. In contrast, I. Koleva *et al.* [11] prepared n-octadecyltrichlorosilane (OTS) capsules by dispersing OTS solution into glycerine solution with $NaOH$ in a T-junction channel. Capsules were characterized in a Couette device, showing similar mechanical response in the small deformation (Figure 1.13(b)). Membrane rupture happens easily in large deformation, due to the small membrane thickness. To obtain thicker membrane, it takes long time

(> 1 hour) as the kinetic reaction at the interface is slow for OTS capsules. The adjustment range of the stiffness of capsules is thus limited. Strain-sweep experiment shows that the OTS membrane has viscoelastic feature (Figure 1.13(c)). In small strain value, elasticity dominates the behaviour of membrane, while when the strain is over 10% viscosity plays more prominently than elasticity.

More recently, albumin microcapsules were made by cross linking protein with a cross-linker, terephthaloyl chloride (TC), in the way of static agitation [25, 29, 51] or microfluidics [120]. These capsules, however, show that the membrane elasticity not only depends on the polycondensation at the interface, but also on the size (Figure 1.13(d)). Therefore, size becomes an essential parameter that needs to be considered in the process of microcapsules preparation.

Polyelectrolytes are expected to synthesize the capsule with controlled membrane properties, e.g., structure, thickness and rheology, through depositing layers [121, 122]. One of promising strategies is the one-step assembly of microcapsules [28, 123], positively/negatively charged polyelectrolyte undergoing fast complexation with the negatively/positively charged one at the interface. Membrane rheological properties therefore can be controlled by varying the concentration, chargeability and complexation time, etc [124].

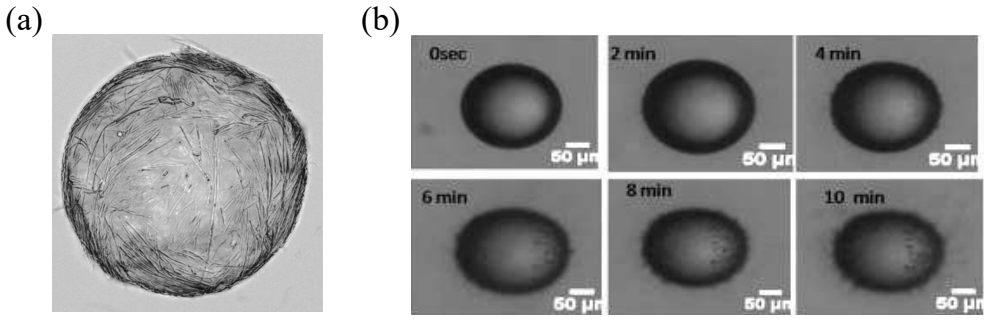

Figure 1.14: Morphology of microcapsules. (a) Polymeric microrods complexed on a capsule surface [125]. (b) Hairy membrane formation by dispersing water droplets in silicone oil with OTS. [126].

1.7.4 Morphology

The nano-/micro-structures of microcapsules determine the morphology. In flow, the initial morphology, for example roughness, might induce additional perturbation to the mechanical response [119]. Polymeric SU-8 microrod particles have been reported to decorate the capsule surface to modify the structure of membrane [125] (Figure 1.14(a)). Moreover, protein-based formation of membrane has been reported a rough

surface if it is exposed to the cross-linking agents for long time [127]. Indeed, the morphology modification of such capsules reflects the degrees of cross linking of membrane. More recently, polysiloxane microcapsules (OTS) [11, 126, 128] have shown that microscale filaments form around the surface, due to complexation between water and OTS (Figure 1.14(b)). pH values, concentration of OTS and polymerization time probably determine the hairy membrane growth. The roughness or hairiness of microcapsule surface result in the inhomogeneity of membrane, for example non-uniform thickness. In the study of focusing on shape modulations, smooth surface is required.

1.7.5 Stability

Since the capsule membrane is generally permeable or semi-permeable particularly for small molecules, e.g., water molecules, mass transfer induced shape instability might occur, for example buckling and shrinking [129, 130], both during the fabrication and characterization. These shape instabilities of microcapsules can be triggered physically either by the gradient of chemical potential between the capsule phase and external phase [131, 132], or by extremely large deformation of membrane under constraints [133].

In the former case, it is known that a spherical capsule buckles to form one or several indentations randomly on the surface, when the pressure change is above the threshold; the pressure variation is often achieved by controlling the osmotic pressure [134]. At the critical situation, the pressure that can support the spherical shape is scaled as $p_{cr} \sim E(h/R)^2$, where R is the radius, E and h are the Young's modulus and membrane thickness, respectively. In the water-in-oil (W/O) or oil-in-water (O/W) emulsification system, the mobility of water molecules occurs across the membrane (e.g., low solubility of water in oil). Consequently, capsules might show shrinking or swelling (see Figure 1.15(a),(b)), changing the initial stress on the membrane in the fabrication; it shows slack on shrinking capsules, while pre-tension on swelling ones. The presence of amphiphilic surfactant molecules [135, 136] is found to enhance the water transfer process. But, as the membrane grows, it additionally induces increasing barrier to the water motility in membrane [28]. Thus, a recipe of fast assembling membrane is required in the preparation of microcapsules to prevent shape instabilities.

In the latter case, shape instabilities, e.g., buckling, might happen when the capsules are exposed to the excessively large deformation. For example, PAH/PSS microcapsules [133] are found to show buckling when passing through a micro-channel with much narrower size than capsules themselves (similar to RBCs moving in capillaries). This happens due to irreversible deformation of membrane (Figure 1.15(c)).

Indeed, after large deformation, nylon capsules [3] and OTS capsules [11] are found permanent residual deformation, which is often thought to be a nuisance in characterization (several times of loading and unloading). Albumin cross-linking capsules [25, 57] show highly elastic behaviour even exposed to large deformation, recovering their spherical shape when the load is removed. The drawback in their investigation is that as mentioned above the membrane rheological properties are dependent on the size distribution.

Microcapsules maintaining their stability is, therefore, essentially required both in the fabrication and mechanical testing. The materials and assembling approaches of membrane have to be chosen carefully. In further, the pre-stress on membrane should be controlled well.

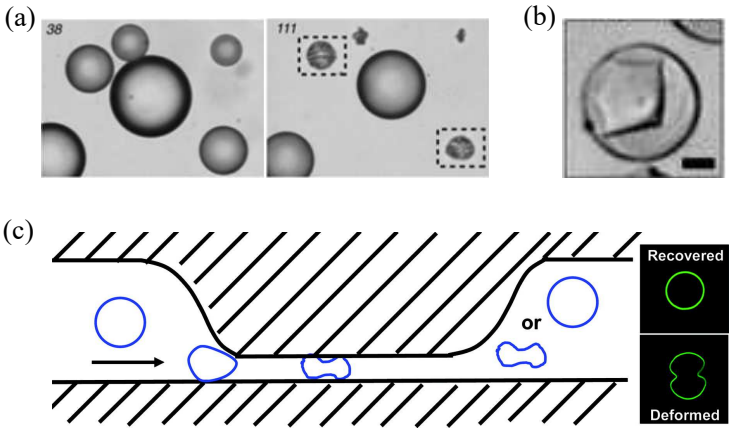

Figure 1.15: Examples of capsules buckling instability. (a) Mobile oil drops with interfacial shear rigidity undergoing compositional shrinking due to mass transfer [132]. (b) Inhomogeneous capsule buckling during polymerization [134]. Scale bar is 35 μm. (c) Mechanical squeezing induced shape buckling when passing a microchannel [133].

To summarize this section:

- Microfluidics provides a controlled way of producing microcapsules in narrow size distribution, prior to membrane formation by chemical cross-linking or electrostatic absorption.
- The range of tuning membrane rheological properties is limited for current capsules formulations.
- Morphology and stability of microcapsules have to be paid much attention in synthesis and characterization.

1.8 Conclusion

In this chapter, we review the modelling of deformable capsules in flows. The global deformation and complex dynamical motions have been investigated excessively. It is well understood that the membrane mechanical properties and flow types govern the capsules responses in flows. However, there are a limited number of investigations focusing on the local self-organized shape modulations of capsules in flows, namely mechanical instabilities such as wrinkling and breakup of membrane. Although general pictures that describe these phenomena have reported, there is still lacking quantitative understanding from the experiment point of view. Existing formulations of capsules synthesis can not be used to study such physical problems, due to their limited tuning range of membrane rheological properties. Therefore, our main objective is to understand quantitatively the mechanical instabilities, wrinkling and breakup, of microcapsules in flow, by developing a new approach of assembling microcapsules with widely tunable and controllable membrane properties. In Chapter 2, we focus on the methods of microcapsules fabrication and characterization. We then present the results of tuning membrane rheological properties in Chapter 3. In Chapter 4, we deform microcapsules in large deformation up to breakup. Finally, in Chapter 5 and Chapter 6, we discuss the wrinkling emergence and development on curved-closed microcapsules.

Chapter 2

Materials and methods

Contents

2.1 Introduction

In this chapter, we present the chemicals used in capsules synthesis, and the methods to characterize them. In Section 2.2, chemicals are listed. Next, we describe the synthesis process of microcapsules with controlled physical parameters in Section 2.3. In Section 2.4, we test capsules stability in suspending fluids under various conditions,

prior to characterization. In Section 2.5, we present the original two-view visualization flow chamber, and validation of flow field with absence of capsules. In Section 2.6, based on the asymptotic solution of small deformation, we address the determination of membrane shear elasticity in both observations. Finally, we introduce two techniques used to measure the capsule membrane thickness: atomic force microscope (AFM) and scanning electron microscope (SEM).

2.2 Chemicals and solutions

Chitosan with medium molecular weight and 75-85% deacetylation (chemical structure in Figure 2.1(a), from Sigma-Aldrich), and anionic surfactant, phosphatidic fatty acids (referred to as PFacidYN, food grade, chemical structure shown in Figure 2.1(b), from Palsgaard E442), were used for assembling chitosan-based microcapsules (referred to as CHT/PFacidYN capsules). Chitosan was dissolved in deionized water (resistivity 18 MΩ cm, Millipore) at pH = 3.0 and at temperature of 22 $\pm$ 2°C, while PFacidYN was dissolved in rapeseed oil (*Brassica rapa*, from Sigma-Aldrich) at temperature of 35 $\pm$ 1°C (in an oven).

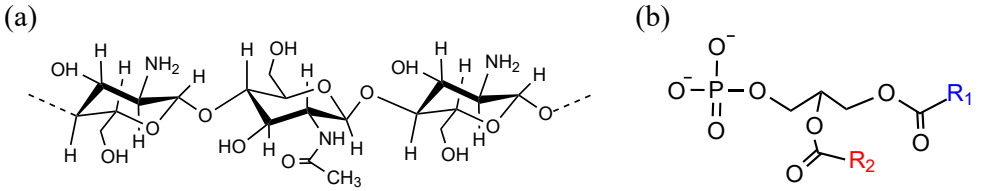

Figure 2.1: Chemical structure of chitosan and phosphatidic acid. (a) Partial deacetylation chitosan. (b) Monomer of phosphatidic acid.

To synthesize protein-based microcapsules, we used human serum albumin (HSA in Figure 2.2(a), lyophilized powder, $\geq$ 97%, from Sigma-Aldrich) dissolved in Phosphate Buffered Saline solution (PBS, tablets from Fisher Scientific), and terephthaloyl chloride (TC in Figure 2.2(b), flakes, $\geq$ 99%, from Sigma-Aldrich) dissolved in a mixture of chloroform (anhydrous, $\geq$ 99%, from Sigma-Aldrich) : cyclohexane (anhydrous, 99.5%, from Sigma-Aldrich): mineral oil (light, viscous liquid, from Sigma-Aldrich) at a ratio of 1:1:4 by volume. Span 85 (non-ionic, from Sigma-Aldrich) was used to stabilize albumin drops before emulsion.

To balance the density of microcapsules and suspending fluids, we used glycerol (98% of purity, from VWR) to mix with chitosan and HSA solutions. To stop membrane reaction after a given time, we used a large volume of mixture of mineral oil and cylohexane (4:1 v/v), followed by pure cyclohexane twice which is compatible with

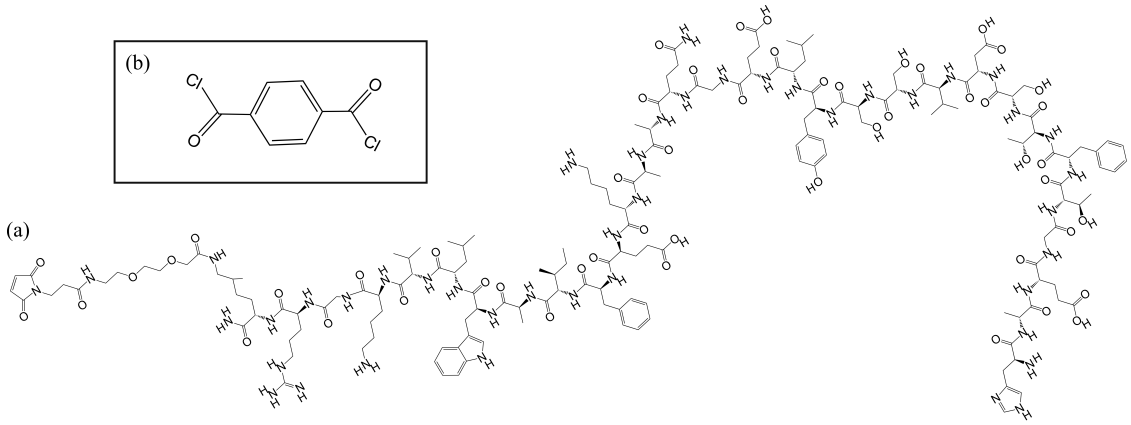

Figure 2.2: Chemical structure of human serum albumin (a) and terephthaloyl chloride (b).

the suspending fluids, to rinse microcapsules. To suspend microcapsules for characterization in a viscous flow, we finally used silicone oils (DC200 from Sigma, AP1000 and AR1000 from Wacker Chemie AG). They are non-toxic for capsule membrane and perfectly repulsive for water (because the encapsulated medium is water based), and have highly thermal and chemical stability.

Detailed solutions preparation and any associated references are available in the Appendix A.

2.3 Microcapsules synthesis

Microfluidics is a well-established technique to control liquid droplets size, which is recently adapted for microcapsules fabrication. However, it is contradictory between the capsules production rate and polymerization time at interfaces, when the size adjustment and membrane growth are coupled in the microchannels. If it works at high production rate of producing capsules, the membrane growth will be weakened, due to shortening the residence time of capsules in the microchannels. Reversely, long residence time prolongs the membrane growth, but simultaneously it lowers significantly the production rate.

To overcome this, and to tune capsule membrane growth in a wide range, we thus decoupled the interface emulsion from drop generation in the microfluidic chip, which is more cost-effective. First, we fabricated monodisperse drop templates by using a microfluidic chip. Then, these templates were transferred into an oil solution with presence of surfactant or cross-linker, where we can control the membrane growth easily by varying the concentrations and reaction time.

2.3.1 Decoupling interface emulsion

Drop-templates generation

Monodisperse water-in-oil drop-templates were fabricated by a 3D home-made microfluidic T-junction chip (Figure 2.3(a), detailed configuration seen in Appendix B). Continuous phase (oil phase) was pumped through the main channel. In contrast, disperse phase (aqueous phase) was introduced by the branch consisting of round glass capillary (from CM Scientific Ltd) of 200 μm or 300 μm inner diameters depending on requirement of capsule size. Indeed, the size of droplets generated in the chip is also related to the flow rate ratio as well as to the relative viscosity ratio of these two phases [137]. The continuous phase is rapeseed oil with a low concentration of surfactant (0.02% PFacidYN or 0.1% Span 85) compared to the finial emulsification concentrations, which thus approximately has a constant viscosity ($\approx$ 70 mPas). In contrast, the viscosity of disperse phase varies, particularly for different concentration of chitosan solution (see Appendix A). For a given flow rate ratio, the higher viscosity ratio, η_{dis}/η_{con}, leads to produce larger capsules. Considering size and production rate together, we therefore narrowed the intersection area of the T-junction chip for strengthening shear forces. Typical dimension of microcapsules produced in our experiment is shown in Figure 2.3(b), with standard deviation of size less than 6%.

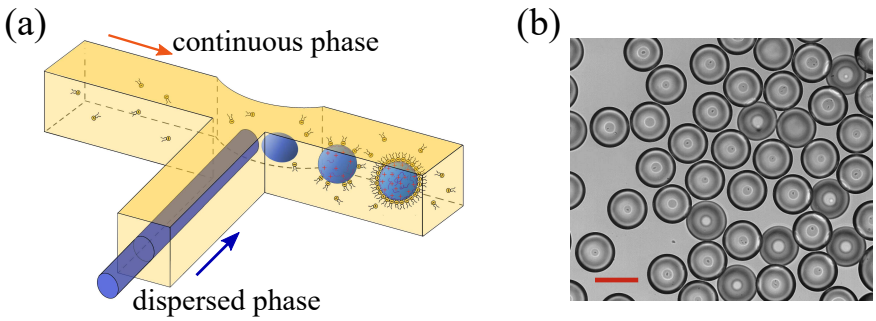

Figure 2.3: Drop-templates generation in a 3D T-junction microfluidic chip. (a) Schematic of T-junction chip fabricated by a 3D printer. (b) Optical micrograph of monodisperse capsules after interface emulsion on a substrate. The scale bar is 200 μm.

The flow rates of two phases were controlled by self-corrected controllers (Fluigent system, see details in Appendix B). By adjusting the flow rates, we can easily modify the size of drop templates with radius ranging from 30 to 300 μm.

Membrane assembly

After droplets generation, membrane is formed around the droplets by electrostatic absorption or chemical cross-linking with presence of PFacidYN or TC (schematic shown

in Figure 2.4). To do that, we transferred drops into a reservoir with a certain concentration of PFacidYN or TC in the organic phase (PFacidYN in rapeseed oil and TC in a mixture) rapidly. Careful shaking was then introduced to expose the liquid templates to reagents homogeneously. To stop the membrane reaction, we thus used a large quantity of rinsing liquid to dilute and remove the reagents. By tuning the reaction time, we expect to control the membrane properties widely. The membrane formation for CHT/PFacidYN capsules is actually driven by the diffusion of the surfactant in bulk, nevertheless for HSA/TC membrane the growth is mainly determined by the content of albumin that bonded on interface (more detail in Chapter 3).

Combination of capsules membrane assembly and elasticity estimation in microfluidic devices [120, 138] is limited to detect the kinetic process at early stage of membrane emulsion, which cannot give access to assemble capsules membrane, typically in the order of a few minutes. In contrast, our decoupling membrane emulsification allows us to tune time more flexibly (from a few minutes to approximately one hour), and to be able to control growth of membrane and therefore its mechanical properties.

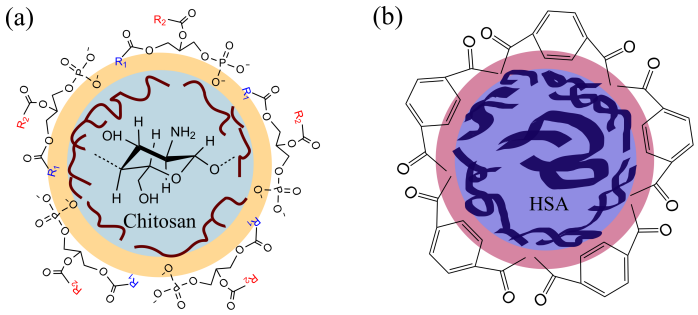

Figure 2.4: Schematic of membrane assembly of CHT/PFacidYN and HSA/TC microcapsules. Chitosan and HSA are enclosed inside capsules in aqueous phase, while surfactant PFacidYN and cross-linker TC move freely in oil phase surrounding capsules.

2.3.2 Stability of capsules during membrane assembly

Although the decoupling interface emulsification allows us to assemble microcapsules with tunable mechanical properties, it is still a challenge to control the morphology and stability of capsules during the membrane formation. In water-in-oil (W/O) emulsion system, the most-likely medium that might transfer out of capsules through membrane is water content, due to their small molecular weight and high motility [136, 139]. As a result, the membrane collapse occurs (Figure 2.5(a)), which is referred to as buckling. Generally, surface of capsule with low stiffness is found to have multiple dimples. In contrast, smaller number of dimples appear on the capsule with larger stiffness. This

buckling, indeed, is a nuisance that we have to avoid in the investigation of capsules deformation in flows. Interestingly, with presence of surfactant, for example PFacidYN in oil phase, capsules start to buckle at a critical size in a long time membrane reaction, $\sim$ 20 minutes, for concentration of PFacidYN 3.3% w/w (Figure 2.5(b)). For capsules size larger than the critical value, their surface show well.

As the amphiphilic surfactant molecules mainly play a role of water carrier in the emulsion [131], and there exists a big step of chemical potential for water inside and outside the capsules, one of the strategies to prevent the buckling is adding a few microliters of water in the bulk phase before transferring CHT or HSA droplet templates into. To achieve a balance, we thus vibrated the bulk strongly, and then let it at rest 10 minutes. The difference of capsules diameter before and after membrane emulsion in this way is less than 3% which is within the standard deviation of size distribution in microfluidics. Another strategy is to increase the osmotic pressure inside capsules by adding some salts in the encapsulated medium, for example Ca^{2+} and Mg^{2+}.

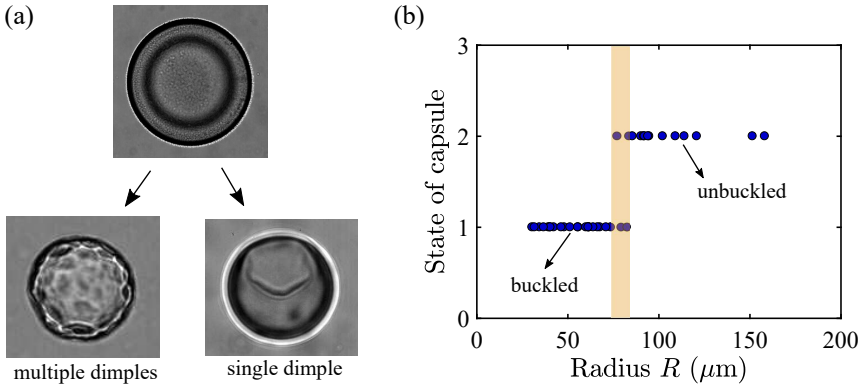

Figure 2.5: Buckling of CHT/PFacidYN micocapsules. (a) Buckling modes of capsules with different membrane elasticity. Multiple dimples were observed on thin membrane, while a single dimple appeared on thick membrane. (b) Capsules stability in oil phase with presence of surfactant during W/O emulsion.

Apart from the buckling observed during membrane emulsion, in the step of washing, capsules instability also might happen, and this depends on the types of washing liquids. When we used the oil which has relatively large water solubility (e.g., rapeseed oil or sunflower oil) as the washing liquid, we found that capsules were susceptible to be buckled (Figure 2.6(a)), but this buckling would be inhibited if the fraction of capsules in the washing liquid was increased. On the other side, if we used the oil with highly repulsive property to water (e.g., paraffin oil or mineral oil) as washing liquid, the stability of capsules during washing can be improved a lot, at least in a time scale of

washing ($\sim$ 5 minutes). The relative size of capsules changed little (Figure 2.6(b)). Cyclohexane here is used to accelerate the sedimentation of capsules in washing process. To check influence of the mixture of mineral and cyclohexane on capsules stability, typically we used two ratios of mineral/cyclohexane = 4/1 (v/v) and 1/4 (v/v) to wash capsules after membrane formation. As expected, these two ratios do not change capsules size compared to that before washing (Figure 2.6(c)). It is very useful that we can control the sedimentation time of capsules in the mixture in the step of washing via adjusting the ratio of mineral and cyclohexane.

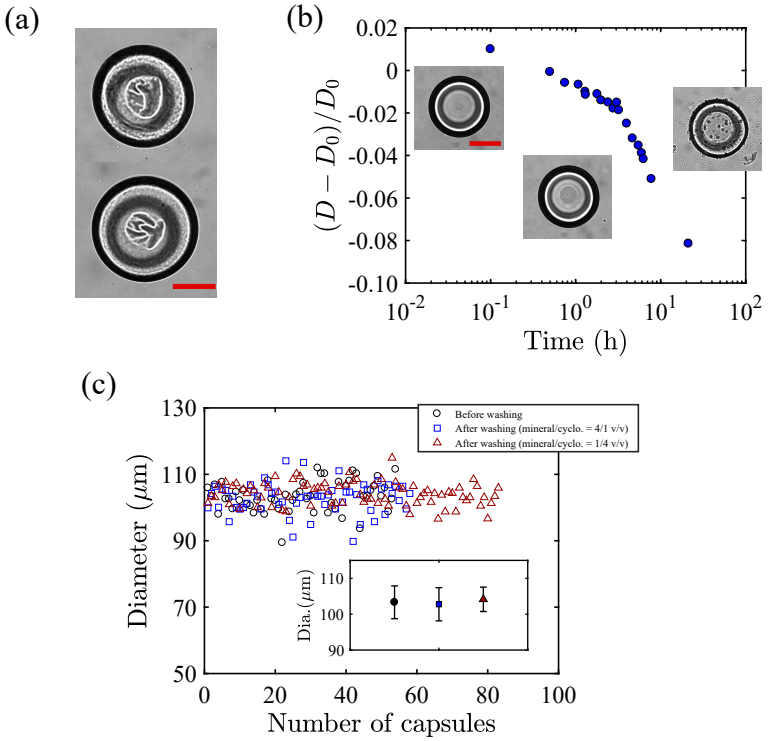

Figure 2.6: Capsules stability in the step of washing. (a) Capsules were washed by a volume of 60 mL rapeseed oil for 10 minutes. Scale bar: 80 μm. (b) Capsules diameter as a function of observing time. The data showed here is during the washing step by a mixture of mineral/cyclohexane = 4/1 (v/v). As there were some surfactant molecules in the mixture, the size showed a slight decreasing for long observation time. Inserted images are states of capsules at beginning, 1 hour and 8 hours from left to right, respectively. Scale bar: 100 μm. (c) Comparison of capsules size before washing and after washing with a mixture. Insert: mean values of capsules diameter with standard error bar. Volume of the mixture is 60 mL. The washing process takes around 5-6 minutes.

2.3.3 Control route of physical properties

In summary, we control microcapsules size during drop templates generation thanks to the microfluidic system, by varying flow rate ratio of disperse/continuous phases and the dimension of capillary inserted in T-junction chip. Membrane growth adjustment can be achieved by varying the concentration of encapsulated medium as well as concentration of reagents in the bulk phase, and complexation time of interface emulsification prior to being rinsed. To avoid the capsules buckling during the membrane assembly and washing step, we pay attention carefully to the capsules size change in each step. Consequently, we are able to ensure that capsules fabricated in our experiment initially have little pre-stress in the membrane.

The decoupling fabrication of microcapsules provides us a single-step way to assemble capsules with tunable membrane properties, which allows us investigate the membrane mechanical instabilities, such as breakup and wrinkling, in flow.

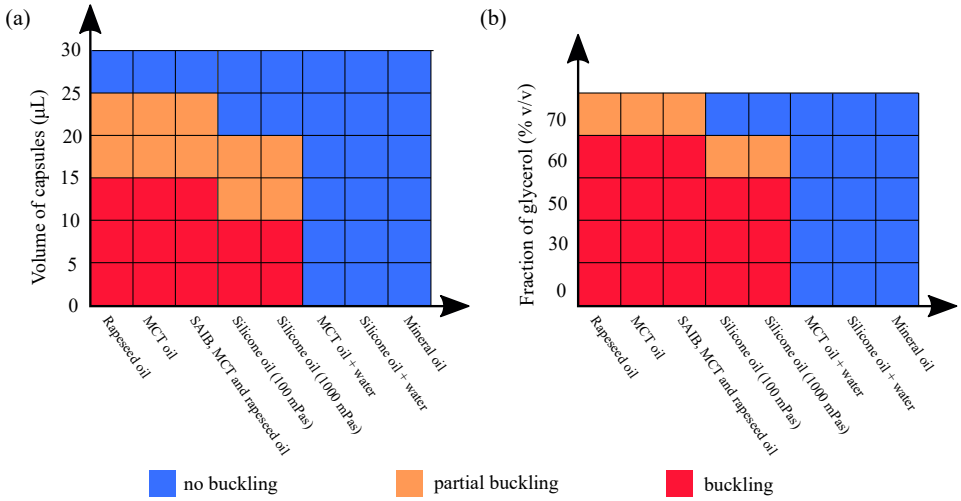

Figure 2.7: Capsules stability in different types of oils. (a) Different concentration of capsules without glycerol enclosed in 5 mL oils. (b) 5 μL capsules with different fraction of glycerol enclosed in 5 mL oils. The duration of capsules staying in oils was around 12 hours.

2.4 Stability of capsules in suspending fluids

After microcapsule synthesis, for characterizing the membrane elasticity we thus need to suspend them in a suspending fluid. Oil-based fluids would be the first choice as the suspending fluids for W/O microcapsules. Similar to the process of capsules preparation, capsules should be stable in such suspending fluids, for example no buckling. In

this section, we discuss water-based microcapsules stability in some common oils, and further discuss the means to control the pre-stress on membrane in suspending fluids.

2.4.1 Qualitative observation of capsules stability in common oils

First, different types of oils were selected and added into closed reservoirs with a fixed volume of 5 mL (see Table A.5 in Appendix A for detailed properties of the oils). Then, we immersed different volumes of capsules (no glycerol enclosed) in these oils, and observed the status of capsules in 12 hours. Figure 2.7(a) shows that increasing the fraction of capsules in a type of oil can inhibit buckling. Saturating the oils with water, for example MCT oil and silicone oil, efficiently vanishes buckling even for the low fraction of capsules. Mineral oil exhibits good features to stabilize capsules.

Increasing the fraction of glycerol that enclosed inside the capsules is also helpful to slow down the buckling for a given volume fraction of capsules in oils (Figure 2.7(b)). Similarly, MCT oil and silicone oil with water treatment, and mineral oil show good performance to prevent buckling.

In this context, we chose silicone oil with water saturation treatment as suspending fluid for capsules characterization. In contrast to mineral oil, silicone oil has high viscosity that produces relatively large viscous stress to deform the capsules.

2.4.2 Pre-stress control on membrane

As discussed above, silicone oil with water treatment can prevent buckling, but it might introduce inflation of capsules if there is excess water in the oil, thus resulting in additional pre-stress on the membrane [13, 140]. This has to be avoided since the pre-stress contributes additional in-membrane tension that influences the apparent membrane elasticity and mechanical behaviours (details in Chapter 3). A question might be asked: how much water should be added to saturate silicone oil ?

Indeed, in practice, it is a challenge to measure the pre-stress on membrane of capsules. One strategy is to monitor capsule size change when subjected in the silicone oil with different water content. The pre-stress on membrane due to osmotic pressure difference Δp is given by Laplace's law

$$T' = \frac{R}{2}\Delta p \tag{2.1}$$

where R is the radius of inflated capsules. If the size difference of a capsule with time, $\Delta R = R - R_0$ has a order of $\Delta R \ll 1$, where R_0 is the initial radius of capsule, we thus neglect the pressure-induced pre-stress in membrane. To achieve that, we

suspended capsules in silicone oil containing various fraction of water content (details in Appendix A). As expected, there is an obvious swelling of capsules when the water content is excessive, while the membrane collapses if the water fraction is low (Figure 2.8). Therefore, there exists a fraction of water content in silicon oil, in which there is no size change of capsules. Again, the swelling and buckling of capsules in such treated silicone oil are dependent on the initial properties of membrane. In contrast to the curve 2 in Figure 2.8, capsules tested in curve 1 have thinner membrane and lower elasticity, therefore inflation happens in the early stage and eventually reaches a plateau due to the balance between pre-stress and membrane elasticity.

Figure 2.8 shows that for 15 μL of water emulsified in 40 mL silicone oil, capsules exhibit good stabilization (size change less than 2% within the measurement error). To check the storage time of capsules in silicone oil affecting the membrane elasticity, we measure surface shear elastic modulus G_s (described later) of the fresh capsules and the capsules stored for one night. Table 2.1 shows that the mean values $\overline{G}_s$ of two situations have little difference. In our experiment, we thus suspend capsules in silicone oil with same treatment of water to ensure no additional pre-stress induced and to prevent any buckling occurrence at rest.

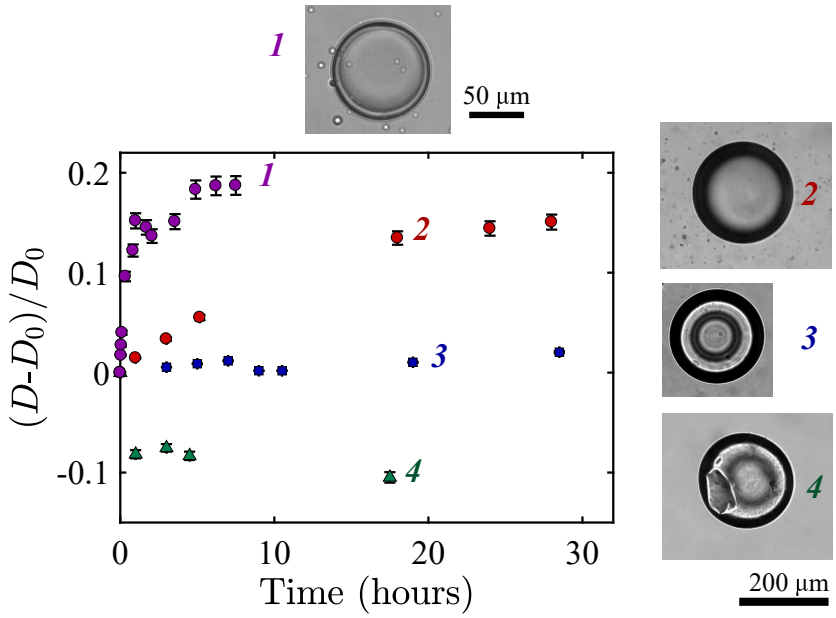

Figure 2.8: Relative diameter of capsules as a function of time in silicone oil treated by different fraction of water. Purple circles: 100 μL water in 40 mL silicone oil, thin membrane of capsules; Red circles: 100 μL water in 40 mL silicone oil, thick membrane of capsules; Blue squares: 15 μL water in 40 mL silicone oil; Green triangles: 5 μL water in 40 mL silicone oil.

Table 2.1: Comparison of surface shear modulus G_s of fresh and stored one night capsules in silicone AP1000 (treatment). Mean value of G_s were calculated from 5-6 capsules selected randomly. Tesing capsules are CHT/PFacidYN capsules.

Capsules	R (μm)	Average $\overline{G}_s$ (N/m)
Fresh	98 ± 2	0.34 ± 0.04
One night	100 ± 2	0.36 ± 0.03

2.5 Planar extensional flow

We used a cross-slot chamber creating a planar extension to deform the microcapsules. Two opposite flows meet at the centre of the chamber, followed by moving backward away from the centre (stagnation point, SG point). Therefore, a symmetric stretching is generated in a region around the SG point. The geometric scale of the chamber is millimetric ($\sim$ 1 mm). It requires smaller volume of suspending fluid, which might be interesting for experiments on toxic or high-price fluids. The viscous stress applied on capsule membrane depends on the extensional rate which is measured by Particle Tracking Velocimetry (PTV).

2.5.1 Visualization

Photography of capsules

The enclosed medium inside capsule is water based, which has a refractive index close to 1.33. The refractive index of suspending fluid is between 1.40 and 1.50, much larger than the encapsulated phase. In vertical observation direction, refraction happens severely at the edge of capsule when light pass from suspending fluid into capsule. Consequently, a black ring appear around the capsule (Figure 2.9(a) and (b)). To weaken the refraction caused by RI difference, one of strategies is to increase the RI of enclosed medium by adding glycerol (Table A.5). Figure 2.9(c) shows that RI of chitosan solution has a linear increase with the fraction of glycerol mixed. But, it also increases the mean density of the chitosan solution.

The photography of a capsule subjected into fluids with different refractive indices also might be affected by the thickness of the suspending fluid between the capsule and the bottom of the channel (Figure 2.10). To verify that, we set a capsule in a vertical channel filled with silicone oil DC200, and captured images of the capsule from different positions in the channel. We found that the image of the capsule near the bottom of the channel has thinner black ring. This provides another strategy that we

should design the flow chamber as thin as possible to reduce the effect of RI difference (see Appendix C).

However, well-match refractive indices between capsules and suspending fluid have to be prevented when we study the wrinkles length development (discussed in Chapter 5 and 6). To do that, we set RI of capsule around 1.36, and RI of silicone oil 1.50, but with balanced density. Images from two views can be seen in Figure 2.11, either by matching refractive index or by balancing the density.

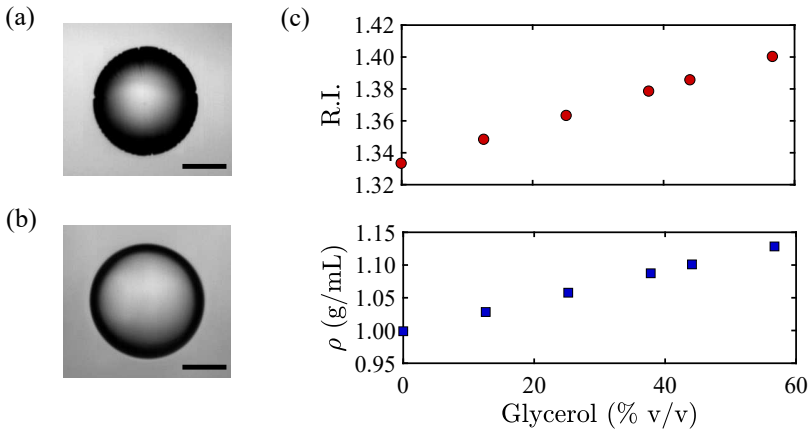

Figure 2.9: Photography of a capsule subjected in the suspending fluid. (a) Capsule without glycerol suspending in silicone oil DC200. (b) Capsule with 30% v/v glycerol suspending in silicone DC200. (c) Refractive index and density of chitosan solution mixed with different fraction of glycerol. Scale bar: 60 μm.

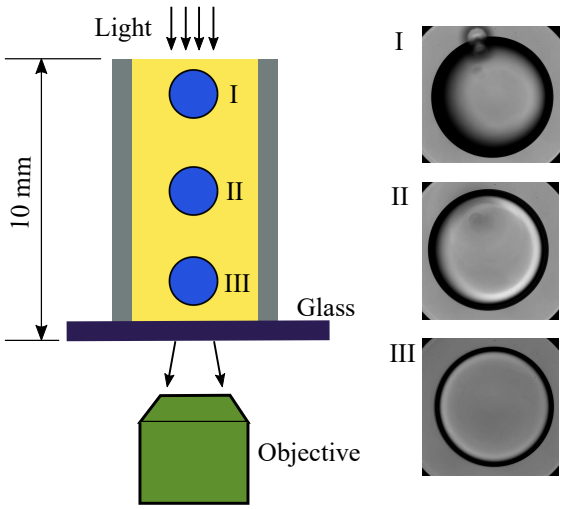

Figure 2.10: Photography of a capsule in a channel filled with silicone DC200. The distance of the capsule from the bottom of the channel influences the imagery.

Cross-slot chamber

The cross-slot chamber consists of perpendicular, bisecting channels with two pairs of inlets and outlets, generating an extensional flow field (see Figure 2.11). The channels were milled on a PMMA plate (RI = 1.48) or PVC (not transparent) with a square cross section 1 mm x 1 mm. To improve visualization quality, the surfaces of channels where light beam passes were covered with thin optical glass (RI = 1.48, from RS France). The outlets of chamber were connected to containers at ambient pressure, and inlets were connected to a glass syringe with a splitter. The syringe filled with capsules was driven by a PI actuator (M235-52S or L-239.50SD) and stepper motor controller (module C663).

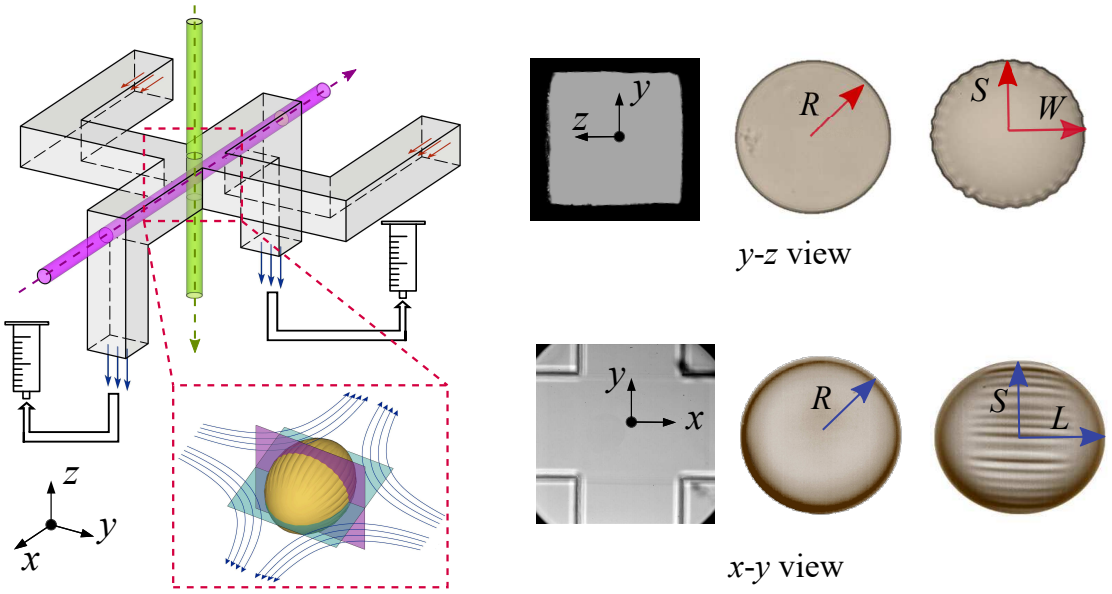

Figure 2.11: The cross-slot flow chamber and visualization of capsules in two perpendicular views. Global deformation and wrinkles length of capsules are measured in x-y view, and profiles are detected from y-z view.

The flow chamber then was placed under an inverted microscope (Olympus IX-71) equipped with 20x or 10x of magnification. A high speed camera (Photron Fastcam SA3) enabled us to acquire up to 5000 frames per second of images. To measure local temperature, we used a digital thermocouple (a precision of 0.1 °C) for correction of the viscosity of suspending fluid. Note that, to minimize transient time of flow, any deformable pipes and air bubbles should be avoided in this system.

To image wrinkles length on capsule surface, we illuminated the chamber in a direction perpendicular to x-y plane (Figure 2.11, x-y view), while detecting profiles on y-z plane was achieved by turning the chamber 90° (Figure 2.11, y-z view). Indeed, we designed the two-view experiment set-ups separately, which is more interesting for

reducing pressure loss and improving photography quality (see details in Appendix C).

2.5.2 Flow field and validation

As mentioned above, the suspending fluid was delivered by a syringe connected to the PI actuator with pushing velocity, 1 μm/s $\leq U_{syr} \leq$ 5000 μm/s. Parameters of the experiment system are listed in Table 2.2. The mean velocity of flow U at the entrance of slot is estimated as

$$U = \frac{Q}{2wd} \tag{2.2}$$

where w and d are the width and the depth of the channel, and $Q = U_{syr}A_{syr} = \frac{1}{4}\pi U_{syr}D_{syr}^2$ is the total flow rate at the main entrance of system. The mean flow velocity U ranges from 0.085 mm/s to 425.45 mm/s.

Table 2.2: The physical parameters of the system.

Ch. width w (mm)	**Ch. depth d (mm)**	**Syringe Diam. D_{syr} (mm)**	**Syringe Vel. U_{syr} (μm/s)**	**Flow rate Q (μL/s)**
1.0	1.0	14.72	1-5000	0.17-850.89

The Reynolds number in this flow-rate driven experiment can be calculated by Equation 2.3 based on the dimension of the channel,

$$Re = \frac{\rho U D_h}{\eta} \tag{2.3}$$

where ρ and η is the density and viscosity of suspending fluid, respectively (1.09 g/mL, 1000 mPas). $D_h = 2wd/(w+d)$ is the hydraulic diameter. The Reynolds number in our experiment is in a range of $9.27\times10^{-5} \leq Re \leq 0.46$, which means that the flow is in the Stokes regime.

For an ideal planar extensional flow, the velocity field is described as

$$u_x = \dot{\epsilon}_0 x, \quad u_y = -\dot{\epsilon}_0 y \quad \text{and} \quad u_z = 0. \tag{2.4}$$

where extension rate ϵ_0 is constant everywhere in a region around SG point. Note that Equation 2.4 is only for the extensional flow with SG point at (0, 0) in Cartesian coordinates.

Experimentally, the extension rate in the vicinity of SG point was measured by Particle Tracking Velocimetry (PTV) [25, 71]. Briefly, 1.6 mg/mL of spherical polystyrene

particles (from Bangs Lab) with average diameter of 10 μm were seeded in the suspending fluid. To avoid particles aggregation, the particle-laden liquid was placed on a roller device for mixing a few hours before using. The images were processed using a home-made Matlab routine based on open-source functions [141]. We tracked each particle in a sequence of images by using cross-correlation functions, which gives us the coordinates of each particles in each image. The interval time Δt of each particle motion in two neighbouring images was determined by the frame rate of fast camera. Thus, the velocity at coordinates (x_i, y_i) can be calculated as $u_{x,i}$ = (x_{i+1} - x_{i-1})/(2Δt) and $u_{y,i}$ = (y_{i+1} - y_{i-1})/(2Δt). We used up to 2000 frames in each video to analyse the velocity field. Typical flow rate tested in our experiment is from 0.85 to 510.54 μL/s.

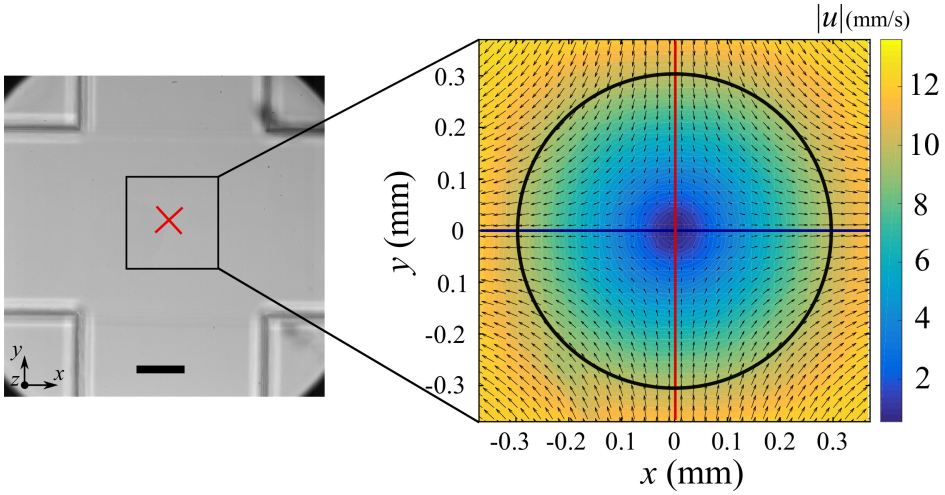

Figure 2.12: Velocity field in the middle plane (z = 0) of the cross-slot chamber for flow rate Q = 17.02 μL/s. The right figure is magnified from the selected area in left one. The two orthogonal lines are corresponding to x = 0 and y = 0. Circle represents the Region of Interest (ROI) defined from Figure 2.13(b). The red cross is the stagnation point. The scale bar is 250 μm.

Figure 2.12 shows the flow field in the vicinity of SG point in the middle plane (z = 0) of chamber. As expected, velocities of two inlet flow vanish at the SG point resulting in u_x = u_y = 0 mm/s. The velocity profiles taken along two axes x = 0 and y = 0 are shown in Figure 2.13(a), confirming the symmetry of the velocity field around the SG point. By differentiating the data in Figure 2.13(a), we thus obtained extension rate along these two centre lines as a function of location, shown in Figure 2.13(b). Again, it gives a symmetrical extension. In the vicinity of SG point (0,0), the extension rate changes little (within the dashed lines), deviation less than 10%. Nevertheless, it decreases drastically when the location is far from the SG point. Therefore, to minimize the measurement error, it is necessary to define a Region of Interest (ROI) where the

deviation of extension rate does not exceed 10% in the x-y plane. We set the ROI with a radius of maximum 300 μm around the SG point, shown in Figure 2.12(circle).

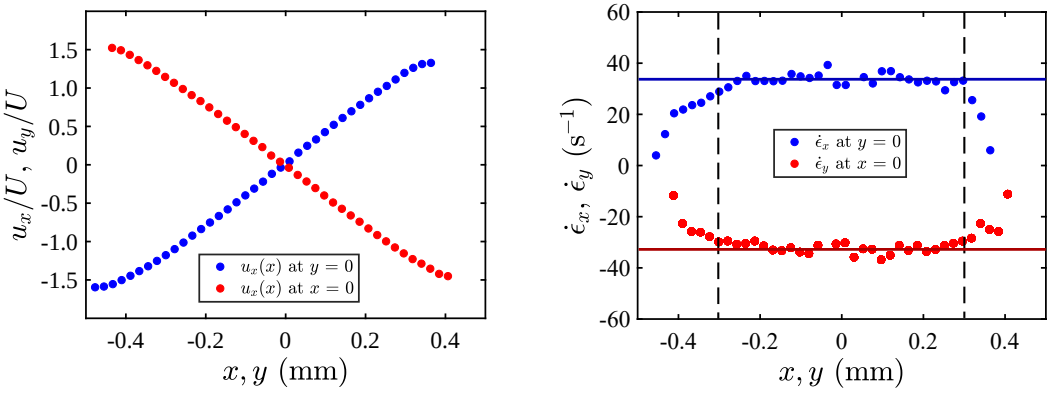

(a) (b)

Figure 2.13: Streamwise flow velocity and extension rates. (a) Dimensionless velocity measured along the two orthogonal lines shown in Figure 2.12 right for flow rate Q = 17.02 μL/s. (b) Extension rate along these two lines calculated by differentiating the data in (a). Vertical dashed lines are corresponding to x, y = $\pm$300 μm. Horizontal lines are the mean values bounded by dashed lines.

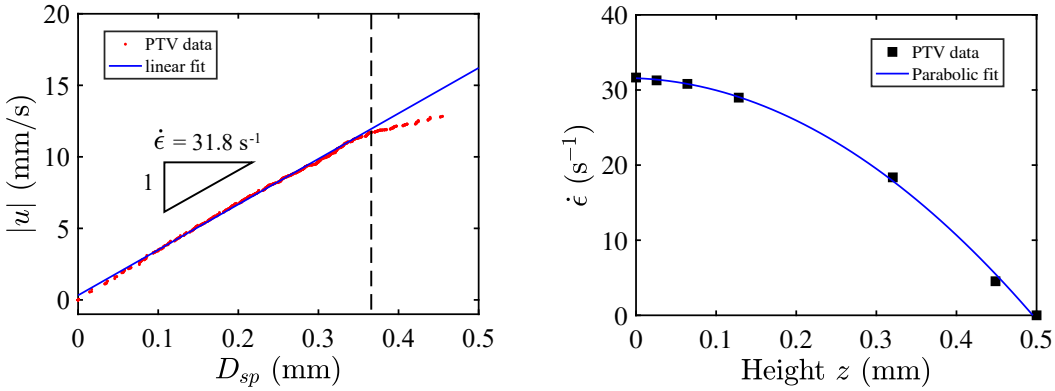

(a) (b)

Figure 2.14: Determination of extension rate $\dot{\epsilon}$ for flow rate Q = 17.02 μL/s. (a) Velocity magnitude $|u|$ as a function of its distance from the SG point D_{sp}. From the slope, we deduced the extension rate $\dot{\epsilon}$ = 31.8 s^{-1} in the middle plane. (b) Parabolic distribution of extension rate in x-y plane along the half depth of cross-slot chamber.

To calculate extension rate $\dot{\epsilon}$ in the ROI, we plotted velocity magnitude $|u|$ as a function of the distance of this velocity point from the SG point D_{sp}, shown in Figure 2.14(a). By fitting the data, we can deduce the extension rate from the slope.

Influenced by the channel walls, extension rate decays along the depth of the channel. Figure 2.14(b) shows that extension rate has a Poiseuille-like profile, $\dot{\epsilon} = f(z)$, with maximum value in the centre plane ($z = 0$). In contrast, the extension rate in the plane z = 0.15 mm decreases within 6%. Experimentally, we only study capsules deformation within the region of $z = \pm 100$ μm.

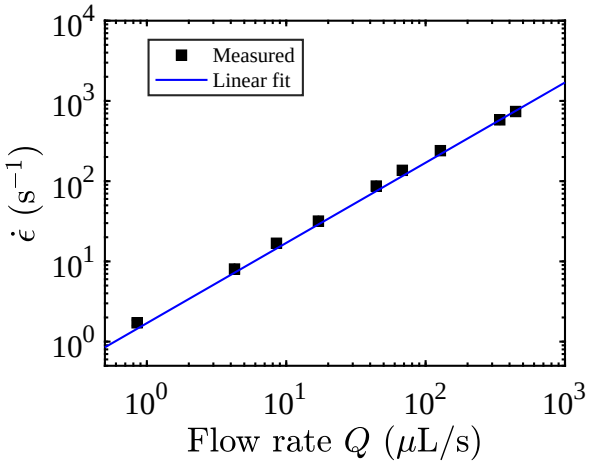

Figure 2.15: Mean extension rate in middle plane of ROI as a function of injected flow rate for the cross slot. The error bar is smaller than the symbols size.

The relationship between flow rate and extension rate in the middle plane is illustrated in Figure 2.15. We found that the extension rate linearly increases with the injected flow rate, typically ranging from 0.85-500 μL, which allows us to modify the extension rate applying on microcapsules easily.

2.6 Determination of membrane elasticity

In flow, the model of Barthès-Biesel [13, 59] provides a connection between global deformation and membrane elasticity of capsule. The capsule has a radius of R at rest, and half-principle axes of L, S and W at deformed, illustrated in Figure 2.16. In the small deformation, the projections of a deformed capsule in x-y and y-z planes are assumed to be ellipsoidal. The Taylor parameter is defined as

$$D_{LS} = \frac{L-S}{L+S} \quad \text{and} \quad D_{WS} = \frac{W-S}{W+S} \tag{2.5}$$

in two observation views, respectively. For $Ca \ll 1$ (Ca is defined in Equation 1.12), the asymptotic theory describes the deformation of capsule in the extensional flow as

$$\frac{L}{R} = 1 + \frac{5}{2}\frac{2+\nu_s}{1+\nu_s}Ca, \quad \frac{S}{R} = 1 - \frac{5}{2}\frac{2+\nu_s}{1+\nu_s}Ca \quad \text{and} \quad \frac{W}{R} = 1. \tag{2.6}$$

where ν_s is the surface Poisson's ratio. By combining Equation 2.5 and 2.6, it generates

$$D_{WS} = \frac{1}{2}D_{LS} = \frac{5}{4}\frac{2+\nu_s}{1+\nu_s}\frac{\sigma R}{G_s}. \tag{2.7}$$

where the surface Poisson's ratio ν_s = 0.5 for incompressible membrane [57] (Indeed, this equation is the result of Equation 1.11 for k = 0). Therefore, for a given size of capsule, we can estimate the membrane shear elasticity, G_s, by interpreting the deformation and flow stress.

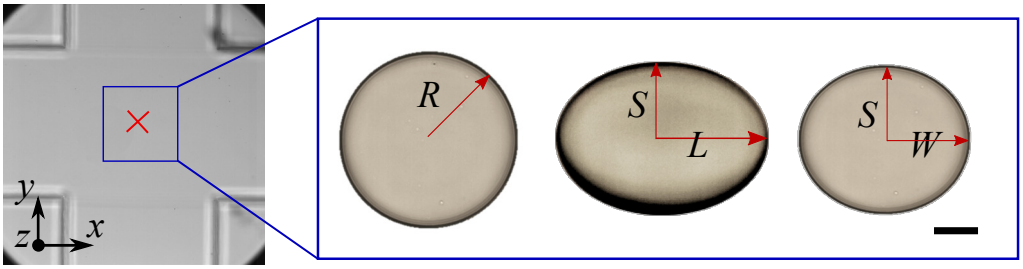

Figure 2.16: Deformation definition of capsule in extensional flow. Red cross represents the stagnation point of flow. The scale bar is 25 μm.

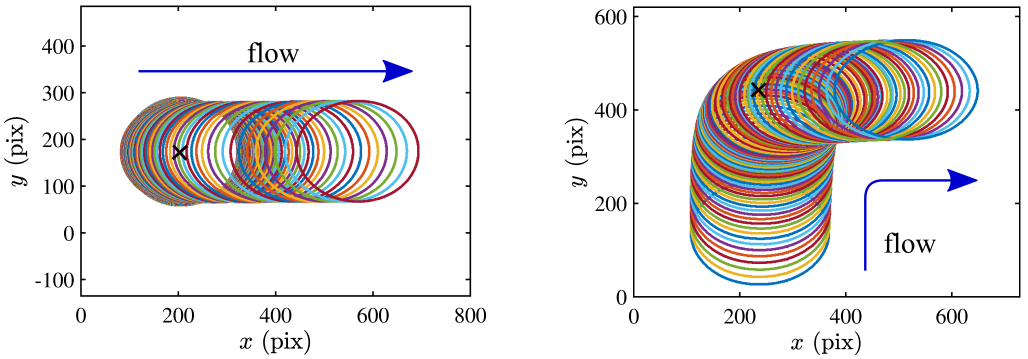

(a) (b)

Figure 2.17: Capsule trajectories in the vicinity of stagnation point. (a) Capsule starts to be stretched at the stagnation point, followed by moving away. (b) Capsule starts to be pushed passing the stagnation point from one of the branches, and then moved away. The black cross is the stagnation point.

Experimentally, to measure the global deformation of capsules, we used two ways to apply the flow. For soft capsules (generally with small G_s) and small deformation, we trapped them one by one at the SG point. Then, we suddenly applied the flow by pushing the syringe. Capsules were deformed from spherical to ellipsoidal, achieving steady-state deformation (Figure 2.17(a)). Alternatively, for stiff capsules (large G_s), to obtain the steady-state deformation, we suck up the capsule to one of the inlet branches 3-5 mm away from the SG point before applying the flow. The time should be enough for the capsule staying in ROI to develop its deformation competing with the flow stress (Figure 2.17(b)). These two different strategies of deforming capsules in extensional flow are equivalent according to previous work [25].

To understand the response of elastic capsules against viscous flow, we plotted the transient deformation, $D(\dot{\epsilon}t)$, as a function of dimensionless time, $\dot{\epsilon}t$, as shown in Figure 2.18. For the capsule starting deformation from the SG point (green circles in Figure 2.18), the Taylor parameter in x-y view increases from zero up to a plateau within the flow time. However, for capsules moving in from one of channel branches, the deformation begins with a value on the first image of the sequences in ROI, up to an asymptotic plateau (red triangles and blue squares in Figure 2.18).

We define the dimensionless response time of capsules to flow as τ_s, and the dimensionless residence time as τ_r. The process of deformation of capsules in the extensional flow can be described as

$$D(\dot{\epsilon}t) = D_\infty \left(1 - e^{-\dot{\epsilon}t/\tau_s}\right) + C, \tag{2.8}$$

where D_∞ is the asymptotic deformation, which can be measured in our experiment, and C is a constant which depends on the initial deformation of capsules at rest. In ideal, $C = 0$ for purely spherical capsules.

To estimate the response time, we used Equation 2.8 to fit experiment data by extracting steady-state deformation from the plateau. Experimental results are in good agreement with the prediction of Equation 2.8 for different asymptotic deformation and membrane elasticity, as shown in Figure 2.18. Through the fitting, we estimated that for example the response time $\tau_s \approx 1.8$ for extension rate $\dot{\epsilon} = 68.69$ s^{-1}, while the residence time of the capsule in ROI is $\tau_r \approx 4.0$ (estimated from images sequences). Therefore, the time is enough for the competition of membrane elasticity against the flow to achieve the balanced situation. Indeed, for stiff capsules, the response time may be larger. It is necessary to start to deform these capsules before they enter the ROI, to achieve the steady-state deformation.

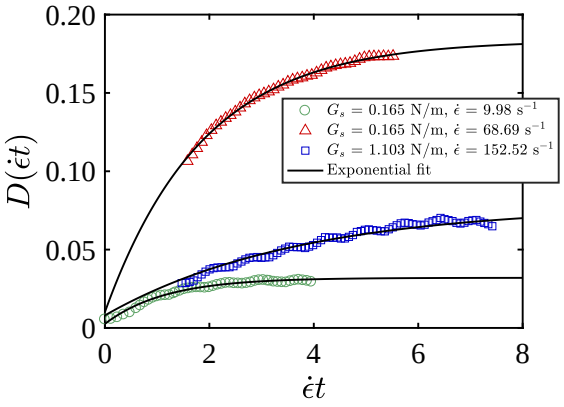

Figure 2.18: Evolution of deformation versus dimensionless time. Symbols are experimental data, and curves are exponential fit using Equation 2.8 with experimental steady-state deformation. The intercept on deformation is not zero because of initial deformation of capsules at rest.

2.7 Atomic force microscopy

Technically, it is difficult to measure *in situ* the membrane thickness of capsules. Optical methods, for instance ellipsometry and reflectometry, are used widely for measuring the thickness of flat membranes. However, for microcapsules with spherical shape, the distortion of light might cause large measurement errors. Thus, we use the atomic force microscope (AFM). First, capsules deposited on a glass-base substrate were left to dry for a week at 40-60°C in an oven (UF 55, Memmert), during which capsules collapsed onto themselves (Figure 2.19 left). The topology of surface of collapsed microcapsules was then studied by AFM [142]. The measurements were carried out by using a Dimension Icon (Bruker) and a Pico Plus (Molecular Imaging) equipped with silicon probes having a nominal spring constant of 0.2 N/m and a tip radius below 10 nm (from Budget Sensors). We used the standard procedure, the contact mode. Data were treated and analysed using Gwyddion software. Topographic variations were obtained after baseline correction via profile measurements on various microcapsules. The membrane thickness was estimated by measuring the height of the collapsed flat regions on the capsules (Figure 2.19 middle and right), and it ranges from dozens of nanometers to a few micrometers, depending on the process of capsules synthesis.

AFM measurement gives us the estimation of capsules membrane thickness in dry state. To estimate thickness in wet, we thus used a flat membrane to stimulate the dry process of capsule. Briefly, the flat membrane was prepared in a centrifuge tube (Greiner, ϕ = 2 cm) by covering aqueous phase with oil phase. Then, we deposited the

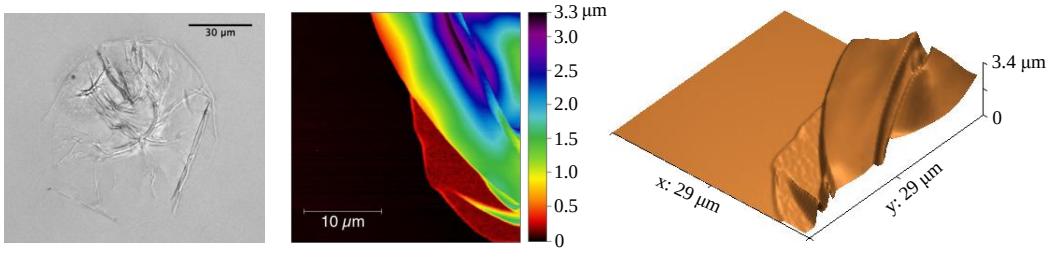

Figure 2.19: Measurement of membrane thickness by AFM. Left: Optical microscopy of a dried microcapsule on a wafer. Middle: Topographic image of a 30 μm x 30 μm area of a dried microcapsule. The membrane thickness is estimated by measuring the height of the collapsed flat regions on the capsules. Right: Three dimensional reconstruction of the topographic image.

after-washed membrane on a substrate placed in the oven (40-60°C). A precise balance was used to monitor the weight change of the membrane during drying. We assume that the loss of water in membrane mainly contributes the thickness, and density of membrane is very close to water. The difference in weight between wet and dry membrane is only due to thickness change (see details in Appendix D). We found that the compensation factor ψ = 1.2-1.4 for CHT/PFacidYN and HSA/TC membrane, which is consistent with PAH/PSS membrane [143].

2.8 Scanning electron microscopy

Although AFM scanning provides a way to estimate the capsule membrane thickness, there is a limit that it works well only for the membrane thickness $h \lesssim 3$ μm. While, particularly for the protein-based capsules (HSA/TC), the membrane in some cases has a large thickness, around 7 μm for a single layer. To overcome that, we use scanning electron microscope (SEM) to image the cross section of membrane (Figure 2.20). Visualization of samples is carried out using a GeminiSEM 500 (ZEISS) at high vacuum condition.

Since it requires conducting substrate for SEM imaging, we thus dry capsules on a glass (ITOSOL12 from Solems France) which has a thin conductive coating on the surface. The drying procedure is the same as that used in the AFM measurement. To improve the image quality, we spray a very thin layer of carbon powder on the sample surface (The carbon layer thickness is around tens of nanometers, which is much smaller than the membrane thickness. It thus can be neglected.). The detailed procedures for the preparation of capsule sample for SEM can be found in the Appendix D. For each batch of sample, we measure at least 4 different capsules.

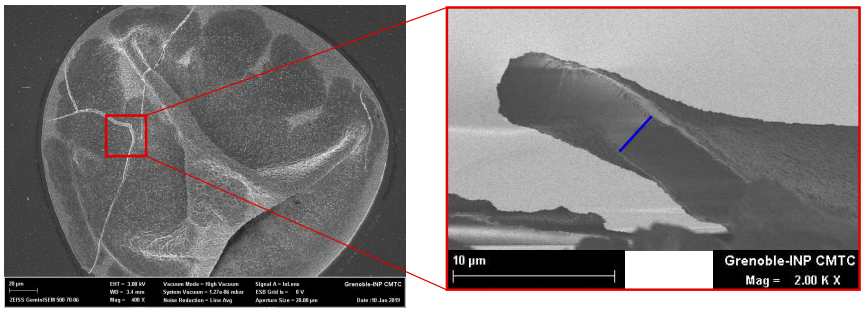

Figure 2.20: Scanning electron microscopic image for a HSA/TC capsule membrane. The blue line shows the position used to detect the thickness.

2.9 Discussion and conclusion

In this chapter, we addressed microcapsules synthesis with tunable membrane mechanical properties, and their characterization by using a hydrodynamic flow. Decoupling interface reaction allows us to assemble capsules membrane in one-step, and to control emulsion time more flexibly in contrast to traditional microfluidic methods. For water-in-oil emulsion, the stability of water-based microcapsules has been investigated to ensure no swelling or buckling occurrence. We proposed a simple way to control initial pre-stress on membrane by adding water content in the external suspending fluid.

To characterize the capsules, we developed a cross-slot flow chamber with two-view visualization. The flow extension rate is measured by PTV. The global deformation and membrane mechanical instabilities of capsules can be characterized directly. Finally, AFM and SEM were used to image membrane morphology, with which we can estimate the order of magnitude of membrane thickness.

Summary

- We developed a decoupling approach to fabricate microcapsules, with the control of size and membrane rheological properties.
- Stability of capsules during the fabrication is essential to control the pre-stress in membrane.
- A two-view visualization set-up was developed to image capsules in 3D, with which membrane elasticity and wrinkling profiles are obtained.
- AFM and SEM techniques are used to measure the membrane thickness.

Chapter 3

Interfacial rheology of microcapsules

Contents

3.1 Introduction

The interfacial rheology measurement is still a challenge up to now, particularly for complex geometries such as spherical capsules. Here, we discuss the estimation of the interfacial properties of microcapsules using the method proposed in Chapter 2. Figure 3.1 shows the relation between steady-state deformation, D_∞, of capsules and the applied flow stress, σ (calculated as $\sigma = \eta\dot{\epsilon}$, η is the viscosity of external fluid). As prediction of Equation 2.7, in the regime of small deformation ($D_\infty < 10\%$), the Taylor parameter has a linear increase with the applied stress for a given membrane property. Whereas, in the large deformation, it becomes non-linear and perhaps leads

to bursting. Yield deformation and relaxation might happen when the capsules are stretched up to very large deformation ($D_\infty > 30\%$).

In this Chapter, to control and modify the membrane mechanical properties, we discuss the effects of these parameters, for example, reaction time and concentration of the components in Section 3.2. In Section 3.3, we discuss the connection between membrane thickness and elasticity. Finally, yield stress and plasticity of capsule membrane are discussed, when the capsules are exposed to large extension rate.

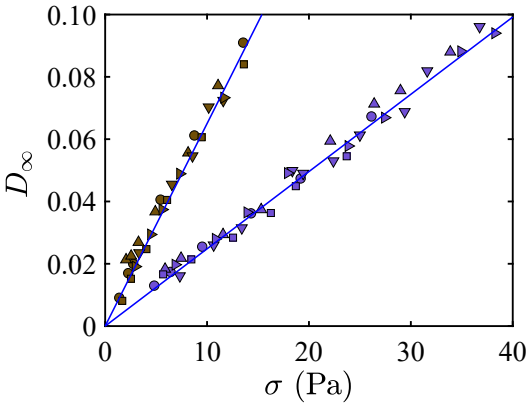

Figure 3.1: Steady-state deformation of capsules as a function of applied stress. Within small deformation, The steady-state Taylor parameter D_∞ increases linearly with the stress. Each symbol means one capsule stretched under different stresses. Lines are the linear fitting result.

3.2 Membrane shear elasticity

Unlike liquid droplets, elastic membrane of capsules plays important roles in protecting core media from the environment, and in targets delivering and releasing under controlled condition. For achieving different purposes, it has been necessary to understand the membrane properties, e.g., interfacial rheology, permeability and adhesion, etc. Among these, more interestingly, interfacial properties of such thin-membrane system determine the membrane behaviours as response to external flow stress. The membrane might loss its initial stability when the elasticity cannot balance the applied forces, resulting in bursting or wrinkling phenomenon. To address that, we first need to understand the strategies to tune and control the membrane elasticity.

3.2.1 Effect of capsule size

The first parameter that we need to control is the size of capsules. As mentioned in Section 2.3, the size control of microcapsules is achieved by modifying the dimension

of drop templates in the T-junction microfluidic chip. In our investigation, the radius of capsules can be tuned in a range of 30-300 μm by adjusting the flow rates of disperse and continuous phases in the process of fabrication.

The surface shear elasticity as a function of initial size is shown in Figure 3.2. The G_s value of HSA/TC capsules taken from the reference [25] shows strong dependence on the initial size. The larger size capsules have higher G_s value. Similarly, for HSA/TC capsules investigated in the thesis, when the size ranges from 90 μm to 150 μm, the G_s varies from 0.08 N/m to 0.42 N/m (data not shown in Figure 3.2).

However, it is more interesting that the dependence of G_s for CHT/PFacidYN capsules is little on the size. For CHT/PFacidYN-1 capsules in Figure 3.2, prepared with 0.25% w/v chitosan solution complexed with 0.36% w/w PFacidYN for 2 minutes, the mean G_s is about 0.11 N/m with a standard deviation of $\pm$ 0.02 N/m in a range of radii from 80 to 200 μm. CHT/PFacidYN-2 capsules have a mean G_s of 0.96 $\pm$ 0.07 N/m fabricated by using 0.3% w/v chitosan solution complexed with 3.3% w/w for 6 minutes, in the factor of 8.0 in size.

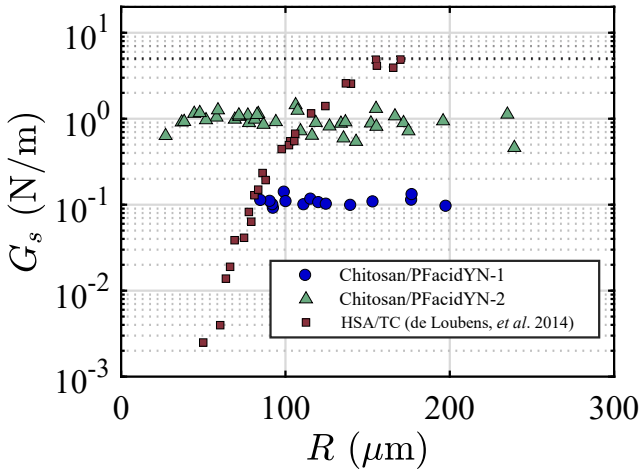

Figure 3.2: Surface shear elastic modulus G_s as a function of capsule radius R. For CHT/PFacidYN capsules, G_s shows independent on the dimension, whereas it varies several orders for HSA/TC capsules. Chitosan/PFacidYN-1 and -2 were fabricated using 0.25% w/v chitosan with 0.36% w/w PFacidYN for 2 minutes complexation time, and 0.3% w/v chitosan with 3.3% w/w PFacidYN for 6 minutes complexation time, respectively. Data from de Loubens *et al.* [25] is made with 10% w/w HSA.

In contrast, a factor of 3.5 in size leads to a factor of more than 2000 in G_s for HSA capsules in reference [25]. These obvious differences can be explained by the kinetics of membrane assembly. HSA molecules enclosed inside HSA/TC capsules have been

completely bonded at the water/oil interface within 30 minutes for 10% w/v concentration of HSA [117]. We assume that the membrane of HSA/TC capsules is homogeneous. In the view of mass balance of HSA molecules absorption, $(4/3)\pi R^3\ C^{bulk}_{HSA} = 4\pi R^2 h C^{surface}_{HSA}$, we thus obtain the thickness $h = (1/3)RC^{bulk}_{HSA}/C^{surface}_{HSA} = 3G_s/E$, where the C^{bulk}_{HSA} and $C^{surface}_{HSA}$ are the concentrations of HSA initially enclosed inside a capsule and bonded at the interface, respectively, and E is the 3D Young's modulus. Note that the concentration of TC is sufficient due to large volume of oil phase compared to the disperse phase in the water-in-oil emulsification. The surface shear modulus G_s should have a linear relationship with radius, $G_s = \frac{1}{9E}RC^{bulk}_{HSA}/C^{surface}_{HSA}$. Big size of capsules, of course, result in large G_s. However, in a real chemical process, this is more complex due to, for example, induced resistance of thickening membrane during HSA molecules cross-linking. G_s might be not perfectly proportional to the size.

Differently, for CHT/PFacidYN capsules, the growth of thickness of the membrane is scaled with time at power of 1/2 and weakly linear with concentration of surfactant that is in agreement with the growth driven by diffusion-controlled formation of surfactant, $h \sim C_{PFa}t^{1/2}$ (details discussed in Section 3.3 of Chapter 3). Here, the concentration of chitosan solution, 0.25% w/v or 0.30% w/v is sufficient for time scale investigated in our study (Figure 3.5(a)). For a given concentration of surfactant and reaction time, the membrane thickness will be independent on the size. Likewise, we simply consider the CHT/PFacidYN capsule membrane is formed homogeneously, $h \sim G_s$. Thus, we may conclude that the surface shear modulus G_s has little dependence on capsule size for the diffusion-driven membrane formation, verified with two formulas in Figure 3.2. This result might be interesting to synthesize microcapsules with uniform interfacial rheological properties for various sizes in the suspension study [144, 145].

3.2.2 Effect of reaction time

In the process of capsules membrane assembly, a first strategy to control the interfacial rheology of capsules would be to vary the complexation time at the interface.

For given concentrations of chitosan and PFacidYN, the shear elastic modulus G_s of CHT/PFacidYN microcapsules increases with the membrane formation time, shown in Figure 3.3. As discussed above, ideally, the surface modulus G_s is proportional to the reaction time at a power of 1/2. However, the process of membrane formation is dependent on many factors, for example, temperature, nano-scale structure and mixing, etc, which result in G_s deviation from the simple expectation. Complexed with 0.36% w/w PFacidYN, for complexation time ranging from 2 to 25 minutes, G_s increases a factor of 10, while with 3.3% w/w PFacidYN, it increases a factor of 7.5 from 3 to 40

minutes. This main difference is probably attributed to different batches of PFacidYN from the company (Note that this surfactant is not pure enough, concentration depending on the batch provided.).

We also monitor the morphology of CHT/PFacdiYN microcapsules with different membrane reaction (Figure 3.3(right)). After washing, the capsules made in different time stages (3 to 40 minutes) show smooth and clean surfaces. This is desired for studying the membrane mechanical instabilities, e.g., wrinkling, in flow, because small defects on the surface might introduce additional uncontrollable perturbation, further leading to the origination of wrinkling instability (discussed in Chapter 5, 6).

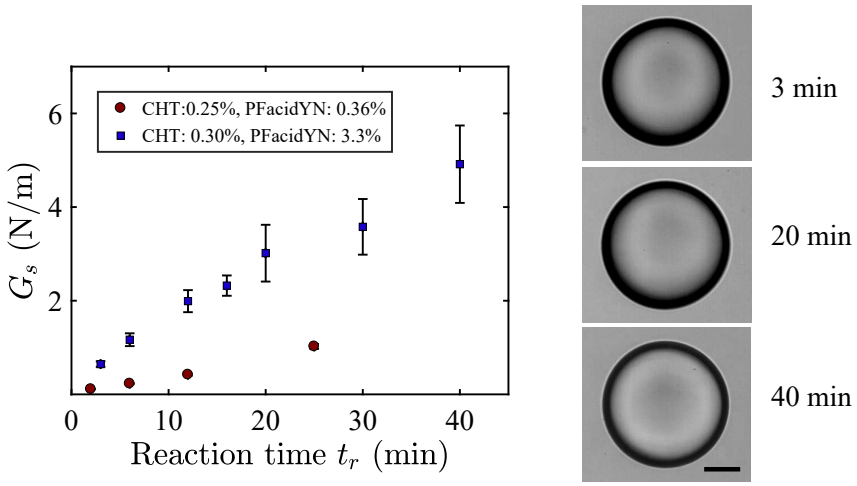

Figure 3.3: Surface shear elastic modulus G_s as a function of membrane complexation time t_r for CHT/PFacidYN microcapsules. Capsules in the images were fabricated by using 0.3% w/v chitosan reacted with 3.3% w/w PFacidYN. The error bars are the standard deviation from 4-8 different microcapsules from the same batch. Scale bar: 60 μm.

For HSA/TC microcapsules, the G_s does not change a lot within 2-20 minutes, as shown in Figure 3.4. According to the study of albumin membrane formation in the references [23, 117], amino group in HSA is bonded onto the interface by reacting with cross-linkers, e.g., TC. For concentration of HSA lower than 10% w/w, in a short time, HSA molecules are bonded with TC at the interface very quickly ($G_s \sim C_{HSA}$). With the presence of 2.5% w/v TC in the bulk solution, most of HSA molecules enclosed inside capsules are consumed completely at beginning of a few minutes. Consequently, the membrane almost stops growing in the rest of time. Mechanically, it shows little dependence of G_s on reaction time.

Different from the morphology of CHT/PFacidYN capsules, long interfacial cross-linking time gives rise to increase the surface roughness of HSA/TC capsules (Figure 3.4 (magnified images)). Similar situation has been observed on OTS capsules [126]

for long polymerization time. With the time of 20 minutes, for example, the surface becomes hairy. During the deformation in flow, we find that these floccules detach from the surface when the extension rate is large enough. This hairy surface can be explained by the acylation process of amino groups in HSA with TC [117], which is out of the scope of our discussion in this thesis. Again, we should avoid the hairy surfaced in preparation of HSA/TC microcapsules, in the study of membrane instability. In practice, we generally control membrane cross-linking time $t_r < 10$ minutes in the work of Chapter 6.

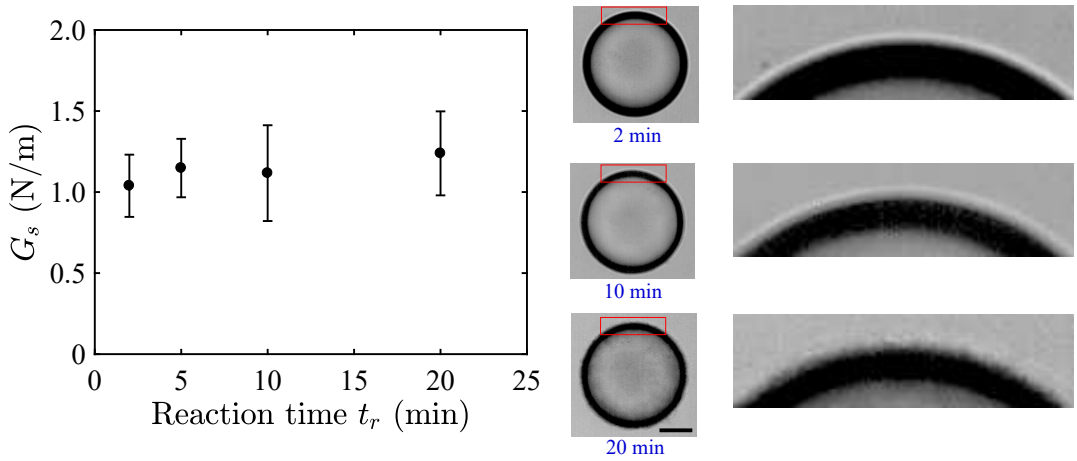

Figure 3.4: Surface shear elastic modulus G_s as a function of membrane complexation time t_r for HSA/TC microcapsules. Capsules were fabricated by using 6% w/w HSA cross-linked with 2.5% w/v TC (HSA dissolved in PBS solution II, see details in Appendix A). Capsules have a radius $R = 95 \pm 3$ μm. The magnified images indicate the part in red rectangles. The error bars are standard deviation. Scale bar: 60 μm.

3.2.3 Effect of concentrations

Another efficient strategy to control the interface properties of capsules is to modify the concentrations of involved molecules in the process of synthesis.

The surface shear modulus G_s increases with the concentration of chitosan solution in the range of low concentration, while it rises up to a plateau after the concentration of 0.5% w/v for two different concentrations of PFacidYN (Figure 3.5(a)). It means that above the critical concentration the amount of chitosan molecules is sufficient for membrane formation. The quantity of PFacidYN molecules, therefore, becomes the limiting factor for the plateau.

In Figure 3.5(b), the G_s has approximately linear correlation with the concentration of PFacidYN ($G_s \sim C_{PFa}$). The difference between two cases in Figure 3.5(b) is

due to preparing capsules with two batches of PFacidYN whose components naturally depend on the preparation process in the factory (Palsgaard). Moreover, for a given complexation time, more concentrated PFacidYN solution (6.6% w/w) brings more resistance for molecules diffusion, consequently leading to lower G_s. For PFacidYN concentration lower than 0.02% w/w, capsules are too weak to keep the shape, coalescence happening, and were not investigated.

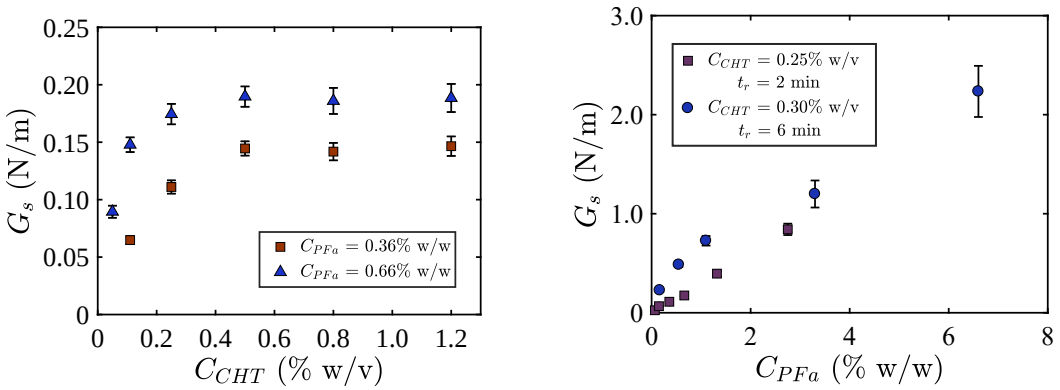

Figure 3.5: Surface shear elastic modulus G_s as a function of concentrations of involved molecules for CHT/PFacidYN microcapsules. (a) Effect of chitosan concentration. Capsules were prepared with two different concentration of PFacidYN solution at a fixed time of 2 minutes. (b) Effect of PFacidYN concentration. Capsules were prepared with reaction time of 2 and 6 minutes, and with 0.25% w/v and 0.3% w/v chitosan solution, respectively. The PFacidYN used in this figure were from different batches (AMP4448-ID21081102 and AMP4455-ID21297301). Error bars are standard deviation.

Enclosing more HSA inside capsules and cross-linked with more concentrated TC solution lead to larger G_s, as shown in Figure 3.6. It seems that G_s increases linearly with concentration of HSA. As discussed in reference [127], at pH 7.4 the free amino group $-NH_2$ content was observed slight decrease when increasing the TC concentration, which exhibits larger shear resistance of membrane in our work. However, limited by the solubility of TC in the organic mixture (see Methods), we use a mother solution maximum 5% w/v of TC in our experiments.

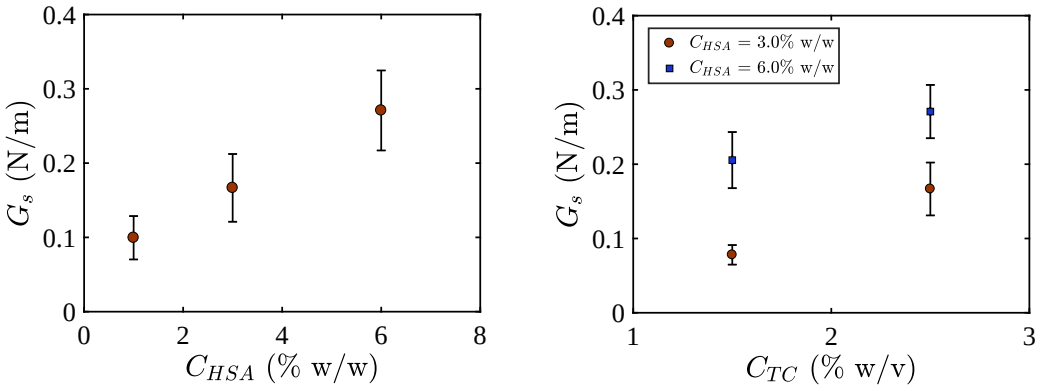

Figure 3.6: Surface shear elastic modulus G_s as a function of concentrations of HSA and TC for HSA/TC microcapsules. (a) Capsules were prepared by using 2.5% w/v TC for 10 minutes. (b) Capsules were prepared by using 3% w/w and 6% w/w HSA for 10 minutes. Note that, in this figure, HSA was dissolved in PBS solution I (see Appendix A). Error bars are standard deviation.

3.2.4 Effect of pre-stress

As experimentally observed in Section 2.4, the microcapsule membrane in our experiment is permeable for water. Under a positive pressure difference between inside and outside of capsules, the core liquid takes water from the outside, eventually achieving an equilibrium with inflation. Reversely, it looses water leading to flab of membrane. The more interesting situation is the case of capsules initially with inflation ($R > R_0$). Compared to the unstressed state ($R = R_0$), for pre-stressed capsules the energy U_s that strengthens the membrane is given by the elastic theory [146],

$$U_s = 4\pi \frac{E}{1-\nu} h(R - R_0) \tag{3.1}$$

where E is the Young's modulus, h is the thickness of membrane, and ν is the Poisson's ratio. R and R_0 are radius of capsule pre-stressed and unstressed, receptively. At rest, the energy increased in capsule membrane is attributed to the work done by the pressure difference Δp which is described in Equation 2.1. By balancing the work and stretching energy, $\Delta p\, 4\pi R_0^2 (R - R_0) = U$, we obtain

$$T' = \frac{Eh}{2(1-\nu)} \left[\left(\frac{R}{R_0} \right)^2 - \frac{R}{R_0} \right] \tag{3.2}$$

for the small deformation, $|R - R_0| \ll R_0$, and thin membrane, $h \ll R_0$. The induced tension by inflation in membrane T' not only correlates with the variation of capsule

size but also with the membrane properties.

When capsules subjected in a flow, the dimensionless tension T/G_s because of hydrodynamic stress is proportional to the Taylor parameter for small deformation, $T/G_s \sim D_\infty$. For unstressed and pre-stressed membrane with apparent G_{s1} and G_{s2}, and steady-state deformation $D_{\infty 1}$ and $D_{\infty 2}$, we have

$$\frac{T}{G_{s1}} \sim D_{\infty 1} \quad \text{and} \quad \frac{T+T'}{G_{s2}} \sim D_{\infty 2} \tag{3.3}$$

in small deformation [13]. When they achieve the same steady-state deformation in the flow, $D_{\infty 1} = D_{\infty 2} = D$, we may write Equation 3.3 as

$$T' \sim (G_{s2} - G_{s1})D \tag{3.4}$$

According to Equation 3.2, for inflation $T' > 0$. We, thus, obtain the apparent surface shear modulus $G_{s2} > G_{s1}$. This has been validated by experiment result in Figure 3.7 and numerical simulation [86].

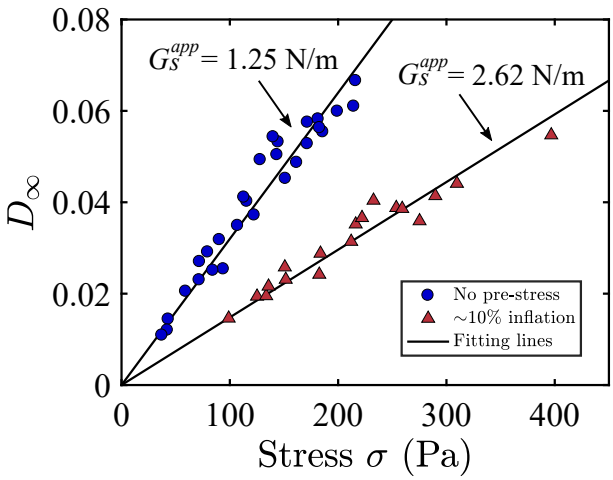

Figure 3.7: Deformation as a function of flow stress for unstressed and approximate 10% inflation of capsules. In small deformation, they both have linear correlation, but pre-stressed capsules show more stiff than the unstressed ones. G_s^{app} was measured by using real size. Capsules were prepared using 0.3% w/v chitosan with 3.3% w/w PFacidYN for 3 minutes. To inflate capsules, we seeded them in a silicone oil treated with excess water.

Pre-stress globally decreases the deformation of capsules which makes them more 'stiff' in response to the viscous stress. To achieve the same level of deformation, we have to impose higher stress for the pre-stressed capsules. This is expected because

the viscous stress traction on membrane must balance the elastic tension as well as the pre-stress. Consequently, we measure a larger apparent G_s for pre-stressed capsules, compared to the unstressed capsules (Figure 3.7). Moreover, for different degree of inflation, we expect to obtain different apparent G_s, and this is not discussed in this thesis. Here, we just discuss qualitatively the effect of pre-stress on the measurement of surface shear elasticity. Experimentally, it is impossible to obtain the real tension induced by pre-stress during the deformation, due to its dependence on the location on the surface. Numerical simulation [86] provides a good way to get insights into the distribution of tension during the capsule deformation.

3.3 Membrane thickness and elasticity

In addition to the elasticity, another property of membrane, thickness h, also dominates the mechanical response of capsules to the flow. Combining the surface shear modulus and the thickness, we can estimate the stiffness of membrane, which is essential in the study of membrane instability. In this section, we discuss mainly the growth of membrane and the shear resistance of the wall materials.

3.3.1 Membrane thickness

As discussed in Chapter 2, the membrane of CHT/PFacidYN capsule is formed by the electrostatic absorption. This process is mainly driven by the diffusion of PFacidYN molecules because the mobility of chitosan molecules is very limited due to their long carbohydrate chains. In a simple way, the diffusion obeys the Fick's second law

$$\frac{\partial C}{\partial t} = D\frac{\partial^2 C}{\partial h^2} \tag{3.5}$$

where the h is the direction orthogonal to the tangential direction of the membrane, and $C(h,t)$ is the local concentration of surfactant that close to the membrane, and D is assumed as a constant diffusion coefficient. Up to time t, the amount of surfactant across membrane onto the surface is given by

$$\Gamma = 2C_0\sqrt{\frac{Dt}{\pi}} \tag{3.6}$$

where C_0 is the bulk concentration of surfactant. If we see the extreme edge of initial drop size R_0, with surface area $A_0 = 4\pi R_0^2$, the molecules that bonded on the surface

has a balance

$$\Gamma A_0 = \frac{\rho A_0 h}{M_n} \tag{3.7}$$

where h is thickness, and M_n is molar mass of the surfactant. Assuming that it has constant density, we thus obtain the thickness $h \sim \sqrt{t}$. This is consistent with our experiment measurement (Figure 3.8) and the observation of gel-like capsules [147].

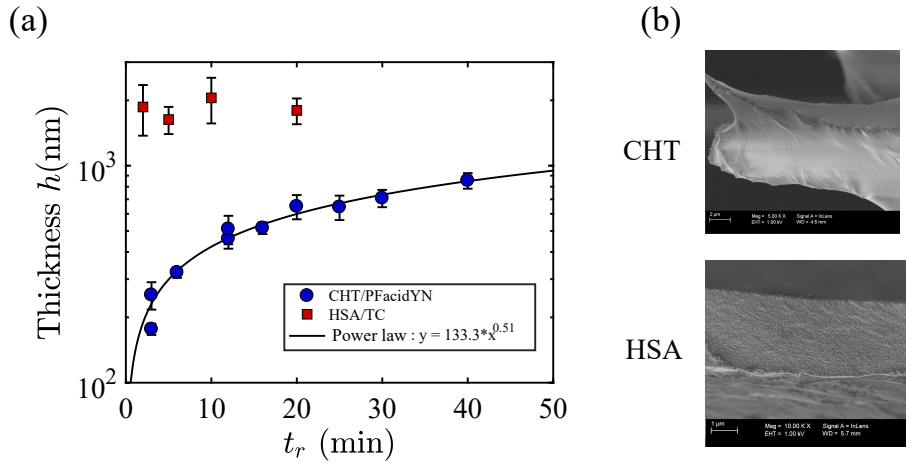

Figure 3.8: Growth of CHT/PFacidYN and HSA/TC microcapsules membrane thickness with time. (a) Membrane thickness as a function of reaction time at interfaces. The growth of CHT/PFacidYN membrane is consistent with the diffusion prediction in short time, whereas HSA/TC membrane is mainly determined by the enclosing HSA molecules. CHT/PFacidYN capsules were prepared by using 0.3% w/v chitosan complexed with 3.3% w/w PFacidYN, and HSA/TC capsules were prepared by using 6% w/w HSA cross-linked with 2.5% w/v TC solution. Error bars are standard deviation. (b) SEM image of cross section of CHT/PFacidYN and HSA/TC dry flat membrane. See details in Appendix D.

In our experiment, we find that in the time scale of our experiment (2-40 min), membrane thickness growth has a power of 0.51 of reaction time ($h \sim t^{0.51}$). For longer time, previous work [147] shows that the thickness growth slows down due to the barrier for diffusion induced by the forming membrane layers. The scanning electronic microscope (SEM) images in Figure 3.8(b) show that the CHT/PFacidYN membrane has smooth surface and cross section.

However, for HSA/TC capsules there is no obvious difference of the membrane thickness for the reaction time t_r = 2-20 minutes (Figure 3.8(a)). This is consistent with the measured G_s value in Figure 3.4. The cross-linking of membrane can finish within a few minutes. The SEM image (Figure 3.8(b)) shows that the cross section of HSA/TC is more rough than CHT/PFacidYN. In addition, it is observed, based on SEM image

of flat membrane, that the side near HSA solution is more smooth than the other one exposed to the oil phase (not shown here).

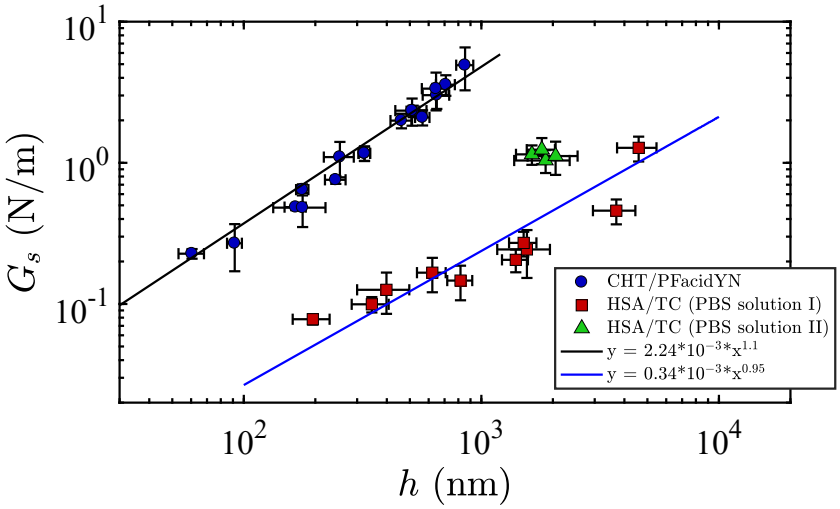

Figure 3.9: Surface shear modulus G_s as a function of membrane thickness h. In both cases, the powders are close to 1. We thus assume that the membranes are isotropic, with shear modulus $G = G_s/h \approx 2.2 \pm 0.4$ MPa for CHT/PFacidYN, and $\approx 0.34 \pm 0.1$ MPa for HSA/TC (PBS solution I). Error bars are standard deviation.

3.3.2 Shear modulus

As discussed above, for homogeneous and isotropic material, it has surface shear modulus $G_s = Gh$, where G is called 3D shear modulus. To know the relationship between elasticity and thickness of capsules membrane, we, here, plot the surface shear elastic modulus G_s as a function of thickness h (see Figure 3.9). By fitting the data, we found that the $Gs = 2.24\times10^{-3}h^{1.1}$ for CHT/PFacidYN capsules, and $Gs = 0.34\times10^{-3}h^{0.95}$ for HSA/TC capsules (Units are not unified here). Since the both powders are close to 1, we assume the membrane as homogeneous and isotropic materials. But, it seems that the PBS concentration has effect on the G_s value (green triangles in Figure 3.9, solution prepared seen in Appendix A). We, finally, enable to tune the shear stiffness as well as the thickness in the process of synthesis. The shear modulus of CHT/PFacidYN membrane has a factor of 6 times larger than that of HSA/TC membrane (prepared in PBS solution I).

3.4 Yield stress and plasticity

The surface elasticity of microcapsules is detected by measuring the global deformation varying linearly with imposed stress in the range of small deformation (D_∞ < 10%), shown in Figure 3.1. If we, however, continuously stretch the capsules up to a large deformation (e.g., D_∞ > 40%), prior to membrane bursting, we observed yield deformation where the deformed capsules are unable to recover back to their initial spherical shape (Figure 3.10(a)). Few examples of these behaviours are presented in a quantitative way. Chang *et al*. [3] observed residual deformation of polymeric capsules after elongated in a four-roll mill device. It is found that the residual deformation, after the flow was stopped, increased with the elongation rate (the one just before the flow cessation). However, the observation time in their experiment was within a few minutes which is not sufficient for membrane relaxation. Longer relaxation time of stretched membrane was not investigated. Residual deformation after flow cessation is also observed in polysiloxane microcapsules in linear shear flow [11], but relaxation process was not presented in that work. In this section, we discuss the residual deformation of CHT/PFacidYN and HSA/TC microcapsules just after the flow is stopped, and their relaxation process in long observation time ($\sim \mathcal{O}(1h)$, in Figure 3.11 and 3.12).

3.4.1 Yield deformation

To describe yield deformation, we measure the Taylor parameter of capsules at rest, after the flow is stopped, defined as residual deformation D_{res}. When applied small flow stress, D_{res} is less than 0.01, where we define that the capsules can return to spherical shape without residual deformation. However, as soon as the stress exceeds the elastic limit of membrane material, capsules are observed not immediately relaxing to their initial spherical shape after the flow cessation.

In fact, most of the recovery in shape of capsules take place in a few seconds after the flow is stopped. However, due to that capsules move out of the observation window in our experiment when the flow is stopped, it takes us 20-30 seconds to re-find the capsules back. In this process, we cannot record the shape change of capsules, resulting in data missing shown in Figure 3.12. Therefore, the residual deformation D_{res} in Figure 3.10 are measured 20-30 seconds delayed after the flow cessation. For given membrane properties, D_{res} increases non-linearly with the value of applied stress σ just before the flow stopped (Figure 3.10(b)), and the orientation of all capsules parallelly point to the direction of principle strain axis (Figure 3.10(a)). If we define a critical stress σ_p where the residual deformation D_{res} = 0.01 after flow cessation, we find that the critical stress σ_p is increased with the surface shear modulus G_s both for

CHT/PFacidYN and HSA/TC capsules. It means that higher shear resistance of membrane makes a capsule 'more elastic' in response to applied flow. This is in agreement with our observation that capsules with $G_s > 1.5$ N/m can return their spherical shape without residual deformation.

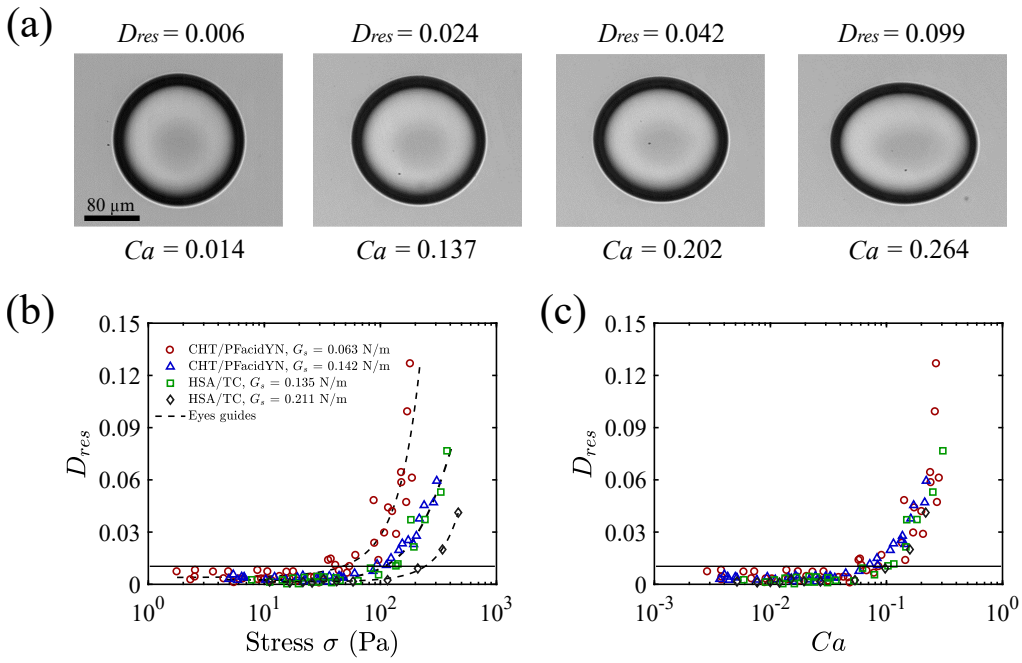

Figure 3.10: Residual deformation of CHT/PFacidYN and HSA/TC microcapsules after extension flow cessation. (a) Micrograph of CHT/PFacidYN capsules after different flow strengths stopped. Images were captured around 30 sec after the flow cessation. (b) Residual deformation as a function of flow stress. (c) Residual deformation as a function of capillary number. The demarcation between elastic and plastic deformation is defined by D_{res} = 0.01, above which it means that deformed capsules cannot recover to spherical shape immediately. The maximum elongated steady-state deformations of CHT/PFacidYN and HSA/TC capsules in (b) and (c) are 0.4-0.55 and 0.7-0.8, respectively.

Considering the applied flow stress and the membrane elasticity of capsules together, we plot the residual deformation D_{res} as a function of Ca number (Figure 3.10(c)). It collapses into a single curve for different membrane materials and surface elasticity. Capsules begin to exhibit yield deformation at a certain critical capillary number, $Ca_p \approx 0.1$. This is counterintuitive that the yield deformation is supposed to be dependent on the materials. Note that, in our experiment, it is still unclear whether the critical Ca_p is uniform or not for various stiffness of capsules.

3.4.2 Relaxation

As discussed before, after the flow is stopped, capsule deformation relaxes rapidly at the beginning of a few seconds (Figure 3.11). To know the process of relaxation in long time, we record *in situ* the residual deformation. The final residual deformation is dependent on the steady-state deformation for give membrane properties (Figure 3.12(a)). Capsules with larger steady-state deformation leads to larger residual deformation, and takes longer relaxation time. Since membrane with large G_s shows large resistance, the final residual deformation is expected small.

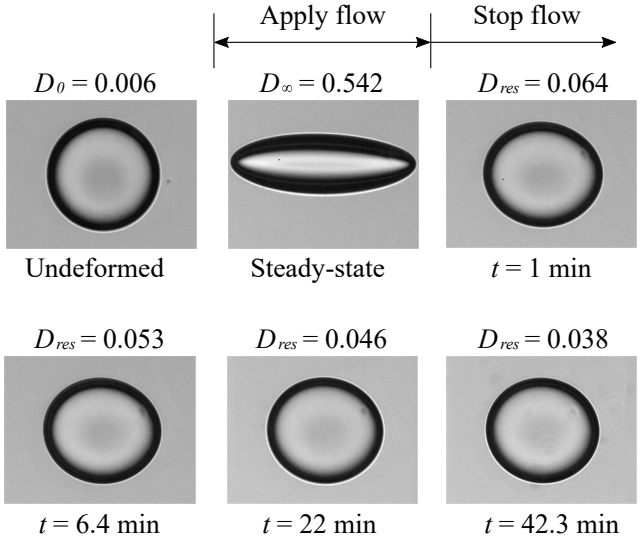

Figure 3.11: Micrograph of a CHT/PFacidYN microcapsule deformed from a spherical shape up to steady-state deformation in a flow of $Ca = 0.172$, and its relaxation at rest after the flow cessation. Capsule membrane $G_s = 0.082$ N/m.

Indeed, the relaxing process that we discuss here is different from that a capsule passes through a narrow-wide channel, for example described in the references [148, 149]. In our case, when the capsule is stretched up to an equilibrium deformation, the flow is stopped, followed by the relaxation which is determined by the membrane elasticity and the viscous resistance from the inside and outside of the capsule. However, the flow is always on in their experiments, in which there exist relaxation and elongation processes when the capsule transfers from the narrow to the wide cross sections of the channel [149].

In dimensionless, we scale the transient deformation by using steady-state deformation, D/D_∞, and observation by using Equation 3.8,

$$t^* = \frac{t}{\eta R/G_s} \tag{3.8}$$

where η is the viscosity of suspending fluid. The characteristic time-scale $\eta R/G_s$ represents the contribution between the membrane elasticity which drives a deformed capsule towards a spherical shape, and the viscosity of the suspending fluid which induces resistance for capsule shape motion. Here, we don't consider the influence of the viscosity of enclosed phase on relaxation. Figure 3.12(b) illustrates that the dimensionless relaxation approximately falls into a single curve, apart from a little difference for the blue triangles. This is due to that the capsule is stretched too much (D_{max} > 0.6). For drops, it is found that drops with initial deformation larger than 0.45 show relaxation dependent on the initial deformation [150]. Reversely, for the not very large steady-state deformation, e.g., D_∞ = 0.2 in Figure 3.12, capsule can return its spherical state in the time scale of our observation.

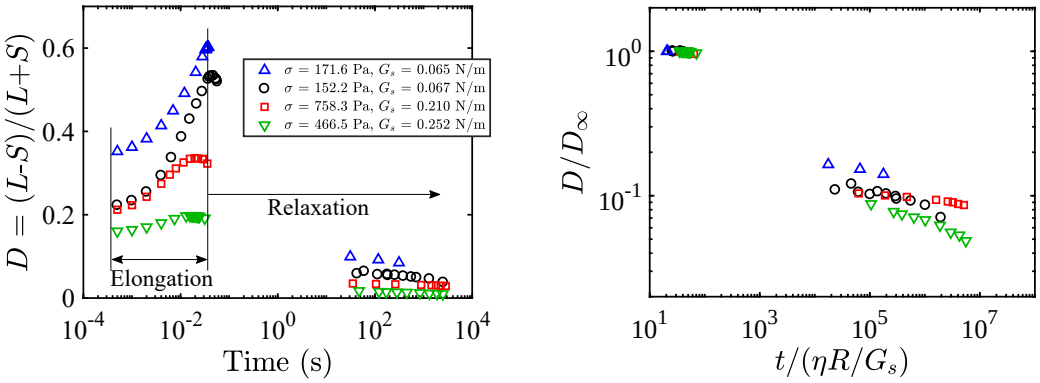

Figure 3.12: Transient deformation of CHT/PFacidYN microcapsules with time in the period of stretching and relaxing. (a) Taylor parameter D as a function of time t. In the region of elongation, the flow is applied to deform spherical capsules up to steady-state deformation (the peak in x-log scale), and the flow is stopped in the range of relaxation. (b) Dimensionless plotting of (a). The viscosity ratio is fixed, $\lambda_\eta \approx 0.04$.

In summary, there exist two relaxing processes for capsules. The first relaxation undergoes within a few seconds, just after the flow is stopped. Release of the stored energies due to stretching deformation is expected to dominate this process. When the capsule releases most of the deformation, it comes the second relaxing process where is indeed the polymer relaxation in membrane (we discussed in this chapter). After undergoing large deformation (plastic deformation), the polymeric layers of the capsule membrane might be changed. Even though the flow stress is removed, the deformation of membrane still retracts due to the residual stress in the membrane. To study these two relaxations, the four-roll mill device [3, 150] might provide a continuous observation.

3.5 Discussion and conclusion

The interfacial rheological properties of CHT/PFacidYN and HSA/TC microcapsules have been investigated in this chapter. In the framework of interfacial properties of capsule membrane, our work generalizes the relevance of planar extension flow method to probe the full scale of deformation of different kinds of microcapsules.

To control and tune membrane properties of microcapsules in a wide way, we decouple the drops generation and membrane emulsification. By combining microfluidic tools, it allows us to assemble capsules in a single-step interfacial complexation, which typically have uniform mechanical properties. Varying concentration of surfactant and complexation time is more efficient to modify the membrane properties of CHT/PFacidYN capsules. In contrast, tuning concentration of HSA solution plays more important for the modification of properties of HSA/TC capsules. Residual deformation and its relaxation for long time scale also have been investigated in this chapter. For given membrane properties, capsules with larger steady-state deformation takes longer time to relax.

Summary

- We have investigated the effect of size, reaction time and concentration of chemicals on the shear elasticity of capsule membrane.
- The membrane assembling of CHT/PFacidYN capsule is dominated by the molecules diffusion, but not the HSA/TC capsule.
- CHT/PFacidYN capsule has larger shear modulus than HSA/TC capsule.
- Residual deformation is observed at capillary number $Ca_p \approx 0.1$, but this still reminds questionable. The relaxation after the flow cessation, indeed, is the polymeric network relaxation in membrane.

Chapter 4

Microcapsules breakup

Contents

4.1 Introduction

Specific and precise therapeutics are receiving a lot of interest towards the development of drugs therapies for diseases [47, 151]. However, several limits such as low solubility, high sensitivity to surroundings and side effects of these new drugs, can impact strongly the efficacy and potential for commercialization as much as the nature of the drugs themselves [17]. Drugs encapsulated inside microgels or microcaspules offer a potential route to overcome such defects, which is commonly designed to provide the therapeutic drug in a right location at proper time with a controlled amount. This requires not only the biodegradablility and compatibility of microspheres, but also the

controllability of the specific drug release [152]. To achieve controlling the release, two prototypic strategies are proposed: self-diffusion across the membrane to prolong the efficiency, and membrane breaking in short time. In the former, the release rate can be controlled by tuning the temperature [98, 130], pH values [41, 45] and enzymes [153], while in the later it requires to know the membrane mechanical properties [5] and the types of breakup.

In practice, these two releasing approaches might be coupled; capsules are broken, followed by the encapsulated contents diffusion out through daughter capsules, with advantage of self-healing wall material [154]. Breakup increases the surface area-to-volume ratio of capsules. For a given diffusion rate, the flux rate into the surroundings is much larger via forming daughter capsules than the parent capsules [17]. Therefore, understanding the breakup and post breakup of microcapsules is playing important roles in controlling of contents release.

Breakup of liquid droplets dominated by the interfacial tension has been investigated well [14, 15, 72, 101, 128, 155, 156], including the rupture threshold and modes, surfactant modification of interfacial tension and rheological nature of liquids. In flows, it is found that droplets might undergo various breakup: bulbous (BU), cylindrical (CY), tip-streaming (TS) and stretched tip-streaming (STS), depending on the viscosity ratio and flow capillary number. At threshold, Grace [101] proposed quantitatively the critical breakup capillary number of droplets as a function of viscosity ratio, both in shear and elongation flows.

In contrast, breakup of capsules dominated by elastic or viscoelastic membrane has been rarely reported, except the examples reviewed in Section 1.6 of Chapter 1. In summary, experimentally rupture near the tips of capsules in large deformation is generally observed, in shear flow [11, 16], elongation flow [102], as well as in an electric field [100]. The remarkable difference between deforming a droplet and a capsule in flow, is the viscous stresses balance arising from the internal and external fluids. Numerical simulations [13, 53, 89] suggested several mechanisms of breakup: membrane thinning, excessive tension and tip-buckling. However, only Chang *et al*. [16] qualitatively speculated that it is most likely membrane thinning inducing the polymeric capsules breakup in shear flow.

Up to now, no other breakup modes (except near the tips) and better explanation of capsules rupture in flows have been reported. In this chapter, we focus on the capsules deformed in a planar elongation flow until breakup. Both viscosity ratio and initial flow strength are considered. We also explore the critical breakup and breakup modes quantitatively.

4.2 Parameters definition

We consider the configuration of a droplet or a capsule with radius R, viscosity η_{in} and density ρ_{in} that is freely suspended in another Newtonian fluid of viscosity η_{ex} and density ρ_{ex}. The interfacial tension of droplet and surface shear elastic modulus of capsule are referred to as γ and G_s, respectively (see Figure 4.1). For capsule, thickness of membrane is quite small (< 300 nm according to Figure 3.9). In both cases, we assume there is no mass transfer between interior and exterior liquids due to immiscibility of these two phases; droplet or capsule preserves its initial volume. Note that, for the aim of comparison, the droplet has the same inner liquid as capsule for a given viscosity ratio. Reynolds number based on the droplet or capsule size is quite small ($Re < 1$), we thus only focus on the regime of viscous effects in our experiment.

To demonstrate the deformation and breakup of droplet and capsule in a planar extensional flow (as discussed in Chapter 2), we remind the main dimensionless parameters used in this chapter are defined as following,

$$\lambda_\eta = \frac{\eta_{in}}{\eta_{ex}} \quad \text{(viscosity ratio)} \tag{4.1}$$

$$Ca = \frac{\eta_{ex}\dot{\epsilon}R}{\gamma} \quad \text{(capillary number for droplet)} \tag{4.2}$$

$$Ca = \frac{\eta_{ex}\dot{\epsilon}R}{G_s} \quad \text{(capillary number for capsule)} \tag{4.3}$$

where the interfacial tension γ and shear modulus G_s are estimated based on the small deformation theory (see Chapter 2 and Appendix E).

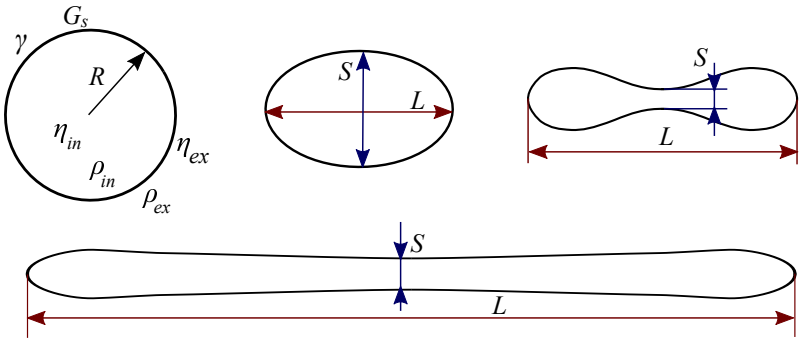

Figure 4.1: Schematic of parameters definition for capsules: Top-left, undeformed state; Top-middle, ellipse-like state; Top-right, bulbous breakup; Bottom, quasi-cylindrical breakup. Capsules are deformed in planar extensional flow.

Prior to breakup, a capsule or a droplet shows quasi-ellipsoidal shape with the major axis L and minor axis S in the planar extension flow (see Figure 4.1). The deformation can be described by the Taylor parameter $D = (L - S)/(L + S)$. However, when it is close to breakup, the apparent shape is far from ellipsoid, shifting into other types, i.e. bulbous. We thus redefine L and S as the maximum elongation length and minimum width at the waist, respectively (Figure 4.1).

Experimentally, we use the cross-slot flow chamber that described in Chapter 2 to deform the droplets or capsules. To exclude the effect of channel wall confinement on breakup, we thus only select small droplets or capsules ($R < 80$ μm, more than ten times smaller than the channel size). We perform a set of experiments ranging in viscosity ratio from around 10^{-3} to 2, and in shear elastic modulus from about 0.02 to 0.3 N/m. Solution and suspending fluids preparation for breakup experiment can be found in Appendix E. Suspending fluids show perfectly Newtonian behaviours up to a shear rate of 1500 s^{-1} which covers the shear rates range used in our experiments. Droplet or capsule fluids are chitosan-based solution with sucrose, glycerol or polyethylene glycol (PEG) adjusting the viscosity ratio, showing quasi-Newtonian feature in the range of shear rate $\dot{\gamma}$ = 1-100 s^{-1} (details seen in Appendix E). HSA capsules are prepared according to Chapter 1. Density is well matched between droplet or capsule and suspending fluids, thus negating the buoyancy effect.

4.3 Comparison of drops and capsules

4.3.1 Overall observation

Figure 4.2 illustrates the moment of breakup for a droplet and a capsule when exposed into a planar extensional flow. Cusped tips are found to form on the droplet, followed by thin threads separating away from the parent droplet. The threads are then broken into many tiny daughter droplets, while the major part of the droplet maintains stable shape after the tiny droplets generation is terminated. This process is generally referred to as tip-streaming (TS) breakup. In contrast, the capsule with the same viscosity ratio as the droplet has never been observed TS breakup. When the applied Ca is slightly larger than the threshold Ca_c, it is found that a narrowing waist forms approximately in the middle section of the capsule (sometime it is asymmetric, see Figure 4.2(b)). Two major daughter capsules finally are produced. However, when the applied Ca is initially much larger than threshold, a cylinder-like shape appear prior to breakup (discussed later).

The observation shown in Figure 4.2 demonstrates that under the similar condition the presence of membrane around the capsule prevents the occurrence of tip streaming. While, droplets are found to avoid tip streaming when the viscosity ratio is sufficiently large [101]. Tip streaming occurs when there exists interfacial tension gradient, which is induced by the distribution of surfactants [156, 157]. However, the elastic resistance of capsule membrane is considered as uniform, and breakup happens when the deformation achieves the limit of wall material.

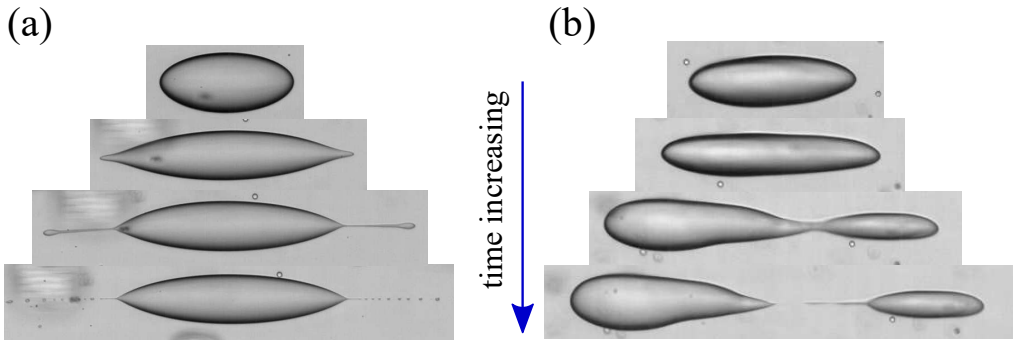

Figure 4.2: Breakup at low viscosity ratio, $\lambda_\eta = 3.5 \times 10^{-3}$. (a) Droplet at $1.8Ca_c$. (b) Capsule at $1.2Ca_c$.

4.3.2 Interfaces deformation

When a droplet or a capsule is subjected into the extensional flow, interfacial tension (for droplet) or elastic modulus (for capsule) preserves the shapes. The interface for droplets is flowing under the effects of internal and external flow fields, while the membrane of capsules might be motionless.

To observe directly the interfaces deformation, we decorate the droplet interface and capsule membrane with hydrophilic poly(methyl methacrylate) (PMMA) particles (Diameter $\approx$ 8-10 μm) [158] or hydrophobic polystyrene (PS) particles (Diameter $\approx$ 8 μm) [28] (details in Appendix E).

In Figure 4.3, by tracking the motion of particles on the droplet and capsule, we thus confirm that the interface of droplet undergoes updating, old interface swept towards the tip, meanwhile new interface formed. The interface motion is then compensated by a circulation inside the droplet driven by a pressure gradient [159]. This updating process continuously proceeds even though the deformation has already became an equilibrium state. However, capsule membrane has finite shearing and area-dilatation resistance [13], which can balance the exerted load by being stretched or bent. The decorative particle, at early stage, moves due to the stretching of membrane itself. Once the deformation reaches a steady state, the particle is motionless which shows the membrane has been stabilized.

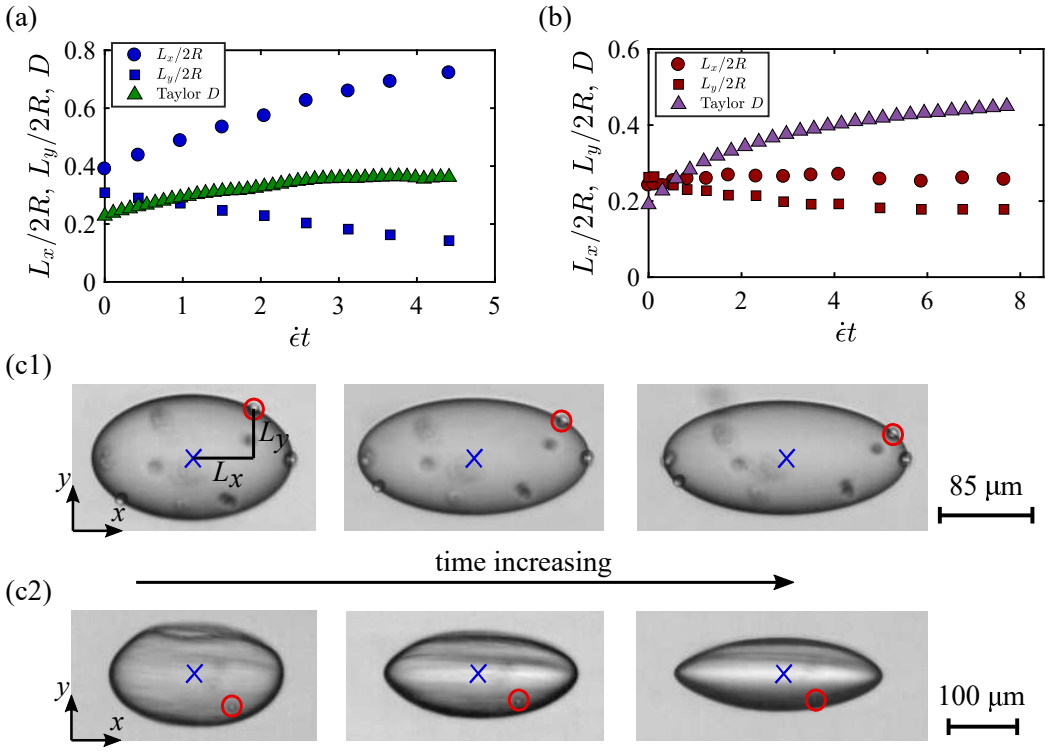

Figure 4.3: Particle tracking on the interfaces of a droplet and a capsule. Dimensionless distance of the particle from the centre and Taylor deformation as a function of dimensionless time on (a) a droplet, and (b) a capsule. (c1) and (c2) show the images of particles decorated on the droplet and the capsule, respectively. Red circles show the location of particles, and blue crosses indicate the centres of the deforming droplet or capsule.

4.3.3 Steady-state and time-dependent deformation

We compare the steady-state deformation of droplets and capsules as a function of applied Ca in the extensional flow (Figure 4.4). As defined in Equation 2.7, the deformation D here is the Taylor parameter. For droplet, the Ca is calculated using Equation 4.2, where the interfacial tension γ is estimated in Appendix E. For capsule, the Ca is calculated using Equation 4.3, assuming the Poisson ratio $\nu_s = 0.5$.

Droplets with viscosity ratio $\lambda_\eta = 2.6 \times 10^{-2}$ shows the same behaviour as a Newtonian droplet with $\lambda_\eta = 1.1 \times 10^{-2}$ in the work of Bentley & Leal. [15]. In the same order of viscosity ratio, droplets breakup in our experiment is found to happen earlier than that observed in reference [15], which will be discussed later. Both of our work and Bentley's work follow well the second-order theory of droplet deformation in the extensional flow (black solid line in Figure 4.4(a)). The details of the theory of droplet deformation can be found in references [15, 160, 161].

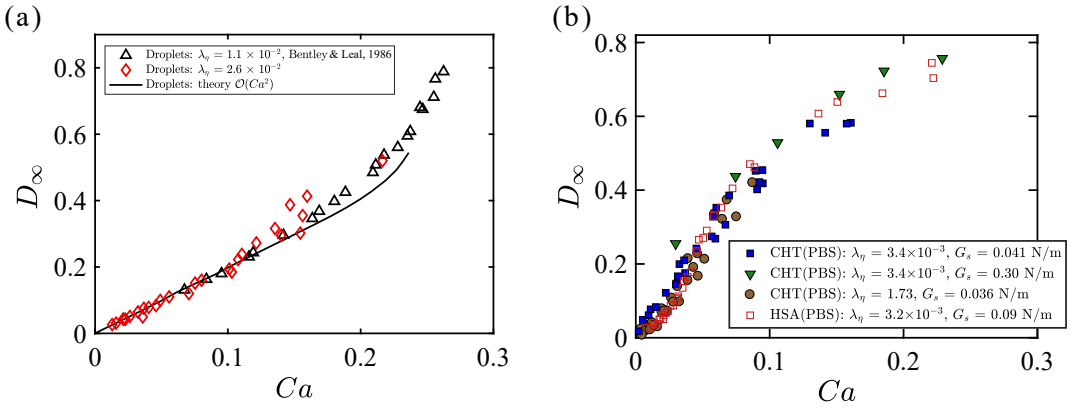

Figure 4.4: Steady-state deformation as a function of capillary number, just prior to breakup. (a) Droplets, compared with results in reference [15]. (b) Capsules with different viscosity ratio and G_s. After the last point in each curve, breakup appears.

In Figure 4.4(b), we can see that the viscosity ratio, as expected, has no significant influence on the Taylor deformation for CHT/PFacidYN capsules, but it does slightly affect the capillary number at breakup. Large value of G_s seems to inhibit the membrane breakup, resulting in large criical capillary number. Another material of capsule membrane is also showed. HSA capsules prepared by PBS solution (solution I) have the similar behaviours with CHT capsules (PBS). In small deformation (D < 20%), all kinds of capsules show linear deformation with the capillary number. We, therefore, might conclude that the deformation and breakup of capsules in flow are closely dependent on the rheology and materials of membrane. In this chapter, we mainly focus on the CHT/PFacidYN capsules breakup.

At the moment of breakup occurring, the deformation can not achieve a steady-state but becomes time-dependent. Figure 4.5 shows two typical time-dependent deformation of capsules. When the initial applied Ca is close to the critical one Ca_c, BU breakup is observed. The capsule is first elongated gradually to large aspect ratio (L/S), but close to the ellipsoid-like shape. Shortly, a waist forms in the middle section of the capsule, and narrows with time. While two main parts form at the ends (inserts in Figure 4.5(b)). Further, the waist is stretched to become a thread, followed by breaking into a number of smaller daughter 'capsules'. The decreasing rate of S/R is much faster than the increasing of L/R (Figure 4.5(a), blue points).

In contrast, if the initial Ca is much higher than the Ca_c (i.e. $Ca \approx 3Ca_c$), we observe that the capsule can be stretched up to a slender geometry with almost the same width along the elongation direction (inserts in Figure 4.5(b)). The variation rates of L/R and S/R are similar (Figure 4.5(a)). We name it as cylindrical breakup (CY). This breakup produces a number of daughter 'capsules' with similar size. Indeed, for droplets, we

observe BU, CY, TS and even STS breakup in our experiment, depending on the viscosity ratio and flow capillary number.

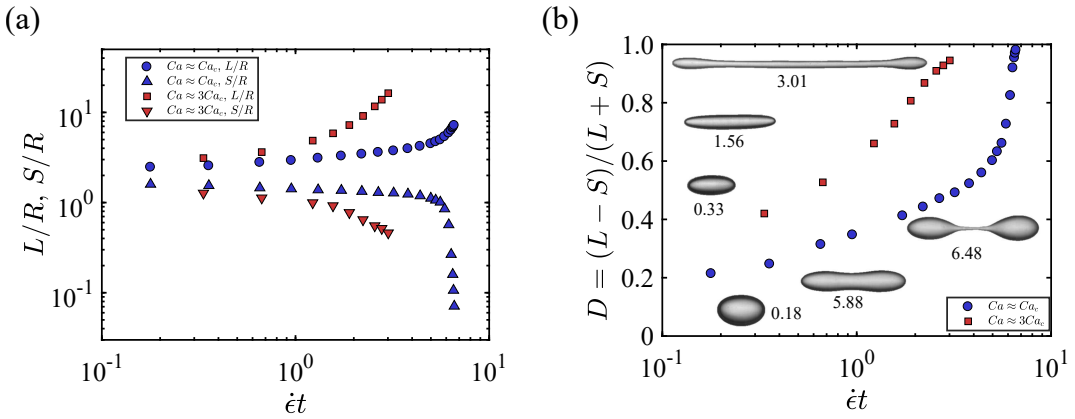

Figure 4.5: Time-dependent deformation and breakup types of capsules. (a) Dimensionless length of elongation and width at waist as a function of time. (b) Deformation as a function of time. The breakup is achieved at two initial applied Ca. Blue points: $Ca \approx Ca_c$; Red points: $Ca \approx 3Ca_c$. The number below inserted images indicate the dimensionless time. Here D is based on the definition in Figure 4.1.

4.3.4 Critical breakup in various viscosity ratios

The breakup point is defined as the steady-state deformation of capsule first time becoming time dependent, as shown in Figure 4.5. Indeed, the time history of velocity gradient that a droplet or capsule experiences has been reported closely relative to the moment of breakup. Torza *et al*. [162] showed that breakup occurrence for droplets in shear flow by a sudden increase of shear rate requires lower critical value of shear rate than that in a flow increasing the shear rate step-by-step. In our experiment, we apply the flow suddenly at a certain value of extensional rate, as shown in Figure 2.17. This is different from the set-ups of four-roll mill [15, 72] and Couette cell [11], in which they can impose the flow stress on droplets or capsules gradually and continuously until approaching the critical situation.

We, here, compare the critical capillary of breakup, defined as $Ca_c = \eta_{ex}\dot{\epsilon}_c R/G_s$ (where $\dot{\epsilon}_c$ is the critical extensional rate), for droplets and capsules, as a function of viscosity ratio λ_η, shown in Figure 4.6. Droplets and capsules in our experiment share the similar inner phase in each viscosity ratio.

The critical capillary number Ca_c of droplets in our work follows well the second-order theory prediction ($\mathcal{O}(Ca^2)$), but has a slight lower than the prediction and Bentley's results. This might be due to the ways of applying the extension flow rate. In

Bentley's experiment, four-roll driven set-up allows to increase the extension rate gradually (from zero to $\dot{\epsilon}_0$, $d\dot{\epsilon}/dt$ is quite small) while always to keep the droplet immobilized at the stagnation point. In this process, each state of the droplet could be considered as quasi-equilibrium up to breakup. It thus has long enough time to compete the viscous stress with a given interfacial tension. In contrast, in our experiment, in each time of deforming the droplets we set the target extension rate $\dot{\epsilon}_0$ by giving a sudden flow ($d\dot{\epsilon}/dt$ is quite large, $\sim \mathcal{O}(10^4)$ s^{-2}). This makes our droplets exposed to strong flow perturbation prior to breakup. For example, the perturbation of asymmetry in deformation (e.g., droplets not exactly at the stagnation point) can induce the droplets breaking at the extensional rate lower than the theoretical predication.

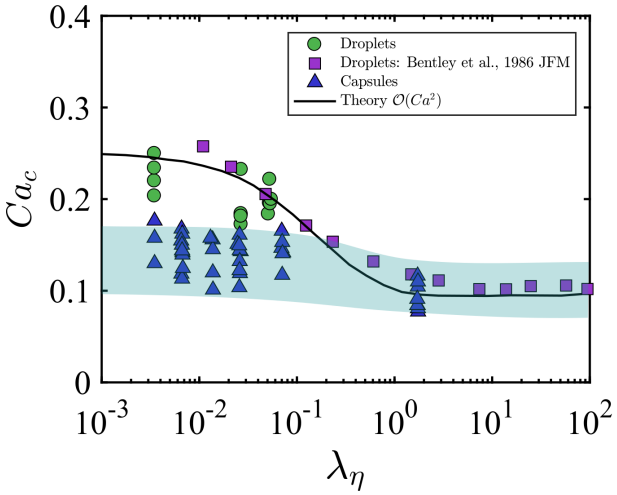

Figure 4.6: Critical capillary number Ca_c as a function of viscosity ratio λ_η in extensional flow. Solid line is based on the small deformation theory [15, 163] for droplets. Capsules studied here have an average G_s of 0.035 N/m. The band indicates the range of critical breakup of capsules. Each point is the mean value.

Compared to droplets, capsules with the same inner phase are found to be broken more easily, requiring lower critical capillary number, particularly in the range of low viscosity ratio (Figure 4.6). When the λ_η is smaller than 0.1, we observe that the critical capillary number Ca_c of capsules is independent on the viscosity ratio, with a mean value around 0.14. While, for $\lambda_\eta > 1$, the Ca_c decreases a little, with a mean value of 0.1. Larger viscosity ratio is not investigated in our experiment. Unlike droplet, the viscosity ratio of capsule does not have big influence on the critical breakup. We think that this is mainly due to the contribution of elasticity (even it is weak) in the membrane, making no interior flow circulation prior to breakup.

4.4 Breakup phase diagrams

In the last section, we know that the capsules might undergo different types of breakup. To understand that, we investigate capsules with various viscosity ratio and membrane shear elastic moduli, exposed to different flow capillary numbers.

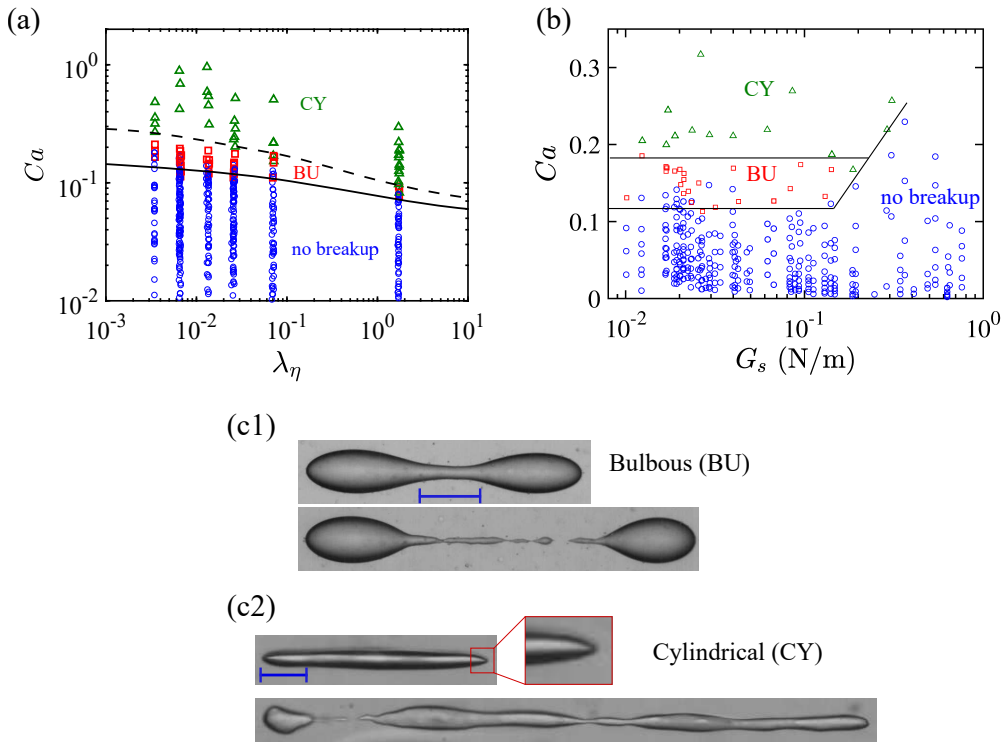

Figure 4.7: Phase diagrams of capsule breakup. (a) Mapping of breakup modes with different viscosity ratios. Capsules have a mean value of $G_s \approx 0.035$ N/m. Solid and dashed lines are th eye guidance. (b) Mapping of breakup modes with different value of G_s. The viscosity ratio is around 0.07. (c1) and (c2) are the snapshots of bulbous breakup at $Ca = 0.1$ with $\lambda_\eta = 2.6 \times 10^{-2}$. Scale bar: 130 μm, and cylindrical breakup at $Ca = 0.36$ with $\lambda_\eta = 3.5 \times 10^{-3}$. Scale bar: 85 μm.

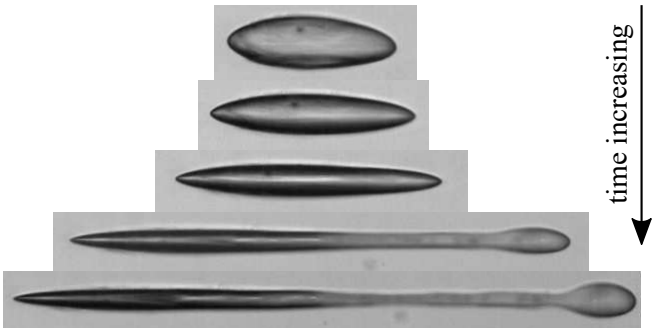

Figure 4.8: Sequences of a capsule with $G_s = 0.3$ N/m, $\lambda_\eta = 3.4 \times 10^{-3}$, at a flow capillary number $Ca = 0.25$, broken in CY mode.

Figure 4.7(a), (b) show the mapping breakup in the extensional flow. For a given viscosity ratio, when the applied stress $\eta_{ex}\dot{\epsilon}$ is smaller than the elastic tension G_s/R of the membrane, stable deformation can be achieved. Once the flow stress is close to the limit of membrane elasticity, a waist is found to appear in the middle section of the capsule, and to narrow with time (described as before, BU breakup). Eventually, a thin filament forms connecting two main lobes, reminiscent of the recent numerical simulation [64]. Thereafter, thin filament is unstable as expected from the Plateau–Rayleigh instability [164] driven by the interfacial tension of droplets, producing a number of much smaller daughter capsules compared to the main lobes after rupture (Figure 4.7(c1)). Since membrane tends to protect the integrity and prevent leakage of the encapsulated liquid, new mixture structure of broken membrane and liquid-liquid interface is formed around daughter capsules which are generally not spherical just after breakup (discussion later).

In contrast, if the applied flow capillary number is initially much larger than the critical one, the capsule can be elongated into a cylinder-like shape with large aspect ratio (We only discuss the x-y view. Indeed, it might be pie-like shape in 3D large deformation, seen in reference [57, 64]). In Figure 4.7(c2), the applied Ca is around three times larger than the Ca_c. The capsule is stretched suddenly up to deformation with almost the same width, except two tips, along the horizontal direction, followed by random breakage of the cylinder forming several daughter capsules with approximately same order of magnitude of size. In the range of low viscosity ratio, at the moment of prior to breakup, capsules are found pointed ends, which is observed on droplets [101, 128, 165]. However, as soon as the rupture occurs, the pointed ends are released.

In both breakup cases, the proceeding time is generally quite small [71], hundreds of milliseconds, depending on the viscosity ratio. Capsules with large viscosity ratio appear to more easily form cylindrical breakup mode (Figure 4.7(a)). More viscous capsule phase induces larger viscosity resistance against deformation, thus it might lead to increase the time scale. The range of capillary number to form bulbous modes is narrowed when the viscosity ratio is increased. We speculate that BY rarely happens in very high viscosity ratio (e.g., $\lambda_\eta > 10$).

Figure 4.7(b) shows capsule breakup modes at various shear moduli and flow capillary number. In the range of small value of G_s (< 0.1 N/m), similar to Figure 4.7(a), high flow capillary number makes it easier to form the CY breakup, while near the threshold more frequently forming BU breakup. The threshold of breakup is found independent on the shear elastic moduli. However, when the G_s exceeds 0.1 N/m, we found that the threshold value increases. In most cases, only CY breakup can be

observed. Limited by our experimental set-up, the breakup of capsules with G_s larger than 0.4 N/m are rarely observed, even by using very viscous suspending fluid ($\eta_{ex} \approx$ 3 Pa·s). The rupture process of a capsule with G_s = 0.3 N/m is shown in Figure 4.8. The capsule first is elongated into a slender-like configuration with pointed ends, followed by a CY breakup.

Indeed, when the G_s is in excess of 0.1 N/m, we often observe wrinkles with small wavelength appearing on the capsule surface (see wrinkling in Figure 5.7), which is significantly different from droplets. But, breakup happens only when the wrinkles disappear completely on account of extremely large deformation vanishing compression in membrane (see Chapter 6).

4.5 Mechanism of breakup

To understand what happens on the membrane at the moment of breakup, we dye the capsules by using fluorescence (Hostasol Yellow 3G, from Clariant, see details in Appendix E). We also use interfacial rheometer system to simulate the membrane rupture under various strains (see Appendix E). In this section, we discuss the breakup of capsules with low G_s (< 0.1 N/m) and high G_s (> 0.1 N/m), respectively.

4.5.1 Low G_s (< 0.1 N/m)

Preliminary simulation result shows that the maximum tension on the deformed capsule is located at the middle part, where the membrane most likely is tore, as shown in Figure 4.9. When the applied Ca is close to the threshold, as described above, the capsule is stretched slowly. Consequently, the capsule has relatively large time scale to adjust it shape ($t \sim \mathcal{O}(0.1s)$). As soon as the middle area is dominated by the liquid-liquid interface (after rupture), drop-like behaviour, pinch-off, happens (red band in Figure 4.9(b)). However, if the applied Ca is much larger than the threshold, the time scale for capsule deformation is much small ($t \sim \mathcal{O}(0.01s)$). The capsule is suddenly stretched into a slender geometry with large aspect ratio. Areas on the capsule undergo membrane rupture almost at the same time, forming liquid-liquid interface (long red band in Figure 4.9(c)). In this two cases (BU and CY), the membrane is deformed continuously (fluorescent video confirming, not shown here). This means that most likely the membrane has a behaviour of soft-solid to liquid transition, due to the slippage between multiple layers [28]. Figure 4.10(a) shows that storage modulus (G' representing the elasticity of membrane) decreases rapidly after the crossover point, which means the surface is governed by the viscosity resistance rather than elasticity.

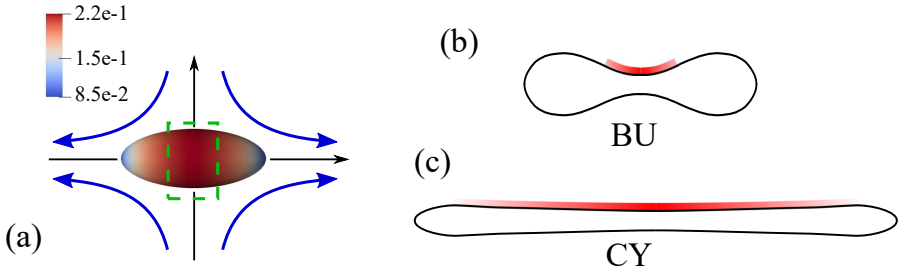

Figure 4.9: Capsule breakup with small value of G_s in the extensional flow. (a) Simulation schematic of a capsule in extensional flow. Colours indicate the tension distribution, and the green dashed frame indicates the maximum tension area. Simulation is performed by M. Leonetti. (b) and (c) show the bulbous and cylindrical breakup, respectively. Red bands illustrate the membrane broken area (in 2D).

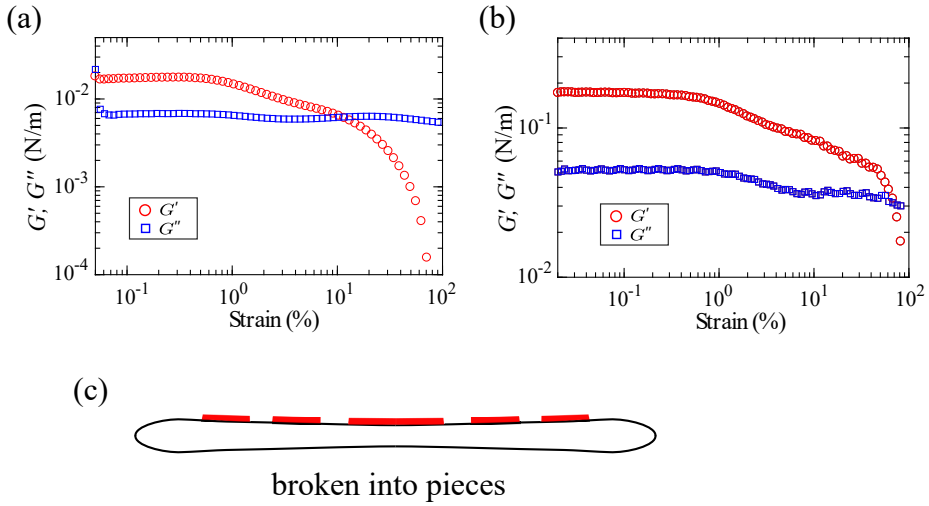

Figure 4.10: Strain-sweep interfacial rheology measurement at frequency 0.5 Hz. Aqueous solution: 0.3% w/v CHT; oil solution: 0.4% w/v PFacidYN. (a) Reaction time 10 min. (b) Reaction time 90 min. In the small deformation (< 1%), $G^{'} \approx 0.02$ N/m in (a), while $G^{'} \approx 0.2$ N/m in (b). The crossover point means the membrane is broken. (c) Membrane rupture randomly in CY mode (high G_s).

4.5.2 High G_s (> 0.1 N/m)

Figure 4.10 shows membranes with different reaction time undergo rupture in the strain-sweep experiment. To break the membrane with higher elasticity ($G^{'} > 0.1$ N/m), we have to apply larger strain. However, it has to input the higher extensional rate to achieve the large deformation for capsule in the flow cell, resulting in small scale time. As discussed above, this again makes capsules having CY breakup mode. Different from the capsule with low G_s, capsule with large G_s shows membrane rupture

randomly and it is not stretched continuously (Figure 4.10(c), also seen in Appendix E). We therefore think that there is no soft-solid to liquid behaviour transition exiting. In contrast, the membrane is broken like a solid elastic sheet.

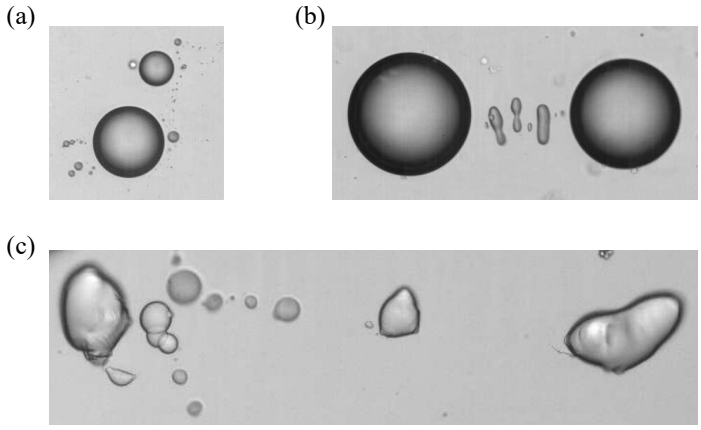

Figure 4.11: Post breakup of droplets and capsules. (a) Droplet with λ_η = 2.7 $\times$ 10^{-2} at $Ca \approx 1.5Ca_c$. (b) Capsule with λ_η = 6.5 $\times$ 10^{-3}, G_s = 0.024 N/m at $Ca \approx Ca_c$. (c) Capsule with λ_η = 3.3 $\times$ 10^{-3}, G_s = 0.15 N/m at $Ca \approx 3.5Ca_c$.

4.6 Post breakup

Figure 4.11 shows the overall shapes of droplets and capsules after breakup. With presence of membrane, the capsule is expected to have irregular shape, while the daughter droplets are found to have perfectly spherical shape. This can be explained from different roles of liquid-liquid interface and membrane.

When the liquid-liquid interface of the parent droplet is broken, new interfaces form immediately around the daughter droplets with the same interfacial tension γ. Total energy of the system is $\sum_{i=1}^{N} \gamma S_i$, where S_i is the surface area for each daughter droplet, and N is the number of daughter droplets. For a given volume, a sphere has the minimum surface area, which makes the system to have the lowest energy (Figure 4.11(a)).

However, with the presence of membrane for capsule, it depends on the elasticity. For low degree of elasticity, daughter capsules are found to be covered by membrane completely in most cases (see Figure 4.12(a) and (c)). As the broken membrane can not cure by forming new membrane without PFacidYN, it most likely means that the membrane has a fluid behaviour. In contrast, capsules with medium degree of elasticity (Figure 4.12(b) and (d)), are found to have non-spherical shape for the daughter capsules. The membrane distribution after rupture begins to show heterogeneous, especially in the generation of CY breakup. We think that the membrane behaviour of

these capsules is between fluid and solid. For the high elasticity, as discussed above, we only observe CY breakup with random shapes of daughter capsules post rupture (Figure 4.12(e)). On the surfaces of some daughter capsules, it is hardly to see the membrane in fluorescent field view. We believe that the membrane has a solid behaviour.

The final shape of daughter capsules is mainly determined by the interfacial tension and elasticity of the membrane. When the membrane has low elasticity, interfacial tension plays an important role, which makes daughter capsules having spherical shape to minimize the surface energy. However, if the membrane has high elasticity (solid like), competition between interfacial tension and elasticity has to be considered. After breakup, membrane undergoes extremely large deformation, which generally has residual deformation. Interfacial tension tends to make daughter capsules to minimize the surface area, but it has to compete with the energy of bending broken membrane [166]. That is why we can observe some capsules with apparent corners. If we apply flow again upon one of the daughter capsules, we find that some of them have the same behaviour as droplets (e.g., tip-streaming), while some of them have behaviour close to parent caspules.

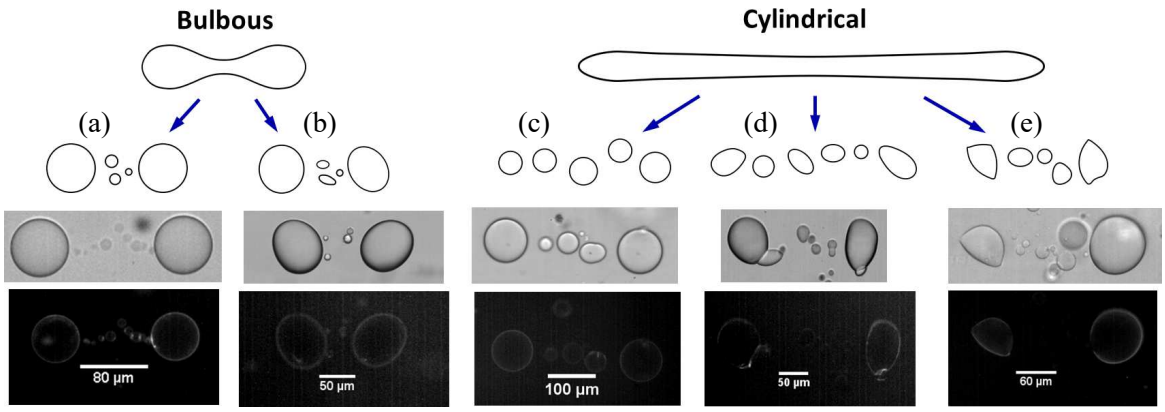

Figure 4.12: Comparison of daughter capsules after breakup. (a) Bulbous breakup: $G_s \approx 0.012$ N/m. (b) Bulbous breakup: G_s = 0.02-0.1 N/m. (c) Cylindrical breakup: $G_s \approx 0.012$ N/m. (d) Cylindrical breakup: G_s = 0.02-0.1 N/m. (e) Cylindrical breakup: G_s > 0.1 N/m. In each column, from top to bottom, it shows the sketch, bright field microscopic graph and fluorescent field image, respectively.

4.7 Discussion and conclusion

We report microcapsules with elastic/viscoelastic membrane undergoing breakup in a planar extensional flow. In contrast to droplets (sharing the same phase as inside capsules), capsules show membrane motionless once their deformation achieve the

steady state. TS, BU, CY and STS breakup modes have been observed for droplets in our experiment (not discussed deeply in this thesis). In contrast, only BU and CY breakup were observed for capsules. The types of breakup and shapes of post breakup are related to the viscosity ratio, membrane shear resistance and initial flow capillary number.

Intefacial rheology and fluorescent images show that capsules with different degrees of membrane elasticity might have different mechanisms of rupture. In the low value of G_s (< 0.1 N/m), it is more reasonable that soft-solid to liquid transition induces membrane rupture. Differently, membrane with large value of G_s is broken like solid sheet, in which membrane thinning would happen [16].

Our experimental results provide fundamental guidance for designing and controlling capsules breakup in flow. Size of daughter capsules can be achieved by types of breakup. BU breakup generates two main lobes with several satellites, while CY breakup produces daughter capsules with similar size.

Summary

- Deformation and interface dynamics of droplets and capsules are compared, confirming that capsule membrane has elasticity even for low G_s.
- Viscosity ratio has slight influence on the Ca_c of capsules in the extensional flow.
- For the G_s < 0.1 N/m, both BU and CY breakup are observed. But, more frequently only CY breakup can be obtained when the G_s larger than 0.2 N/m.
- Solid to liquid transition happens in low G_s. In contrast, membrane thinning induces the breakup for large G_s.

Chapter 5

Wrinkling instability in the Near-Threshold regime

Contents

5.1 Introduction

Thin-membrane systems often involve in spontaneously re-organizing their morphologies and shapes in response to the applied constraints such as hydrodynamic flow fields. In particular, particles with liquid cores and thin shells, such as red blood cells (RBCs) [21, 77], vesicles [167] and capsules [10], are expected to show shape oscillation or shells buckling in flows. These responses are considered as the consequences of coupling effects between flow stress and shell rheological properties.

The global deformation and complex dynamics of such soft particles in flow have been investigated well in past decades [5, 39, 56, 57]. It, for example, concerns overall elongation, tank-treading [51] and tumbling [11] motions. However, the local shape modulation, such as wrinkling, during the deformation has received rare investigation, except several preliminary examples discussed in Chapter 1. Indeed, the mechanism of shape modulation of soft particles is more complex than that on flat elastic

sheets [90, 91, 97, 168]. This is attributed to the interplay between the deformation and applied flow, and the curved-closed geometry [12]. Such wrinkling modulation on deformable particles is essential for evaluating the membrane properties or the failure limit of materials in bioengineering applications.

In this chapter, we study the emergence of wrinkling on CHT/PFacidYN microcapsules in a planar extensional flow (see experimental set-up in Chapter 2). The aim is to understand mechanism of wrinkling on the curved and closed geometry, and to characterize quantitatively the threshold of wrinkling and even the transition to folding. Here, we focus on the membrane instability of microcapsules in Near-Threshold region (NT), where the capillary number Ca is not far from the critical value Ca_c^w. Capsules with various size and shear rigidity were investigated.

5.2 Wrinkling induced by flow

Soft microcapsules with thin membrane were first experimentally observed wrinkling in a shear flow [10]. Since several types of dynamics of capsules (e.g., tank-treading and tumbling) exist in the shear flow, it makes more difficult to characterize the wrinkling, if for example with the presence of time-dependent shape oscillation [11]. Although there exists stable shape of capsules in the shear flow, tank-treading motion of the membrane makes the analysis and visualization of wrinkles challenging, due to varying stress distribution in membrane. For the sake of simplicity, we thus use a simple planar flow to deform the capsules: viscous traction induced by the extensional flow (Figure 5.1(a), more detailed methods in Chapter 2). Two observation views (x-y and y-z) allow us to examine how the membrane wrinkling initiates and develops on capsules during the deformation (Figure 5.1(b) and (c)).

Figure 5.1 illustrates the experimental sketch and overall observation of capsules deformed in the extensional flow. At the stagnation point of flow, the capsule is stretched along x-axis, while it is under compression along the azimuthal direction in y-z plane (see details later). In small deformation, the shape is generally ellipsoidal. The regularly-spaced wrinkles are pointed towards two ends of the capsule, and meanwhile distribute periodically in the azimuthal direction. Capsule with large membrane thickness is found to have large wavelength (arc distance of two adjacent peaks in azimuthal direction, defined in Figure 5.9). But, oppositely, the capsule with small thickness is always found stable without wrinkles. If under large enough stretching, the well-defined distribution of such undulation is broken up, in which the distortion is strongly localized at the cost of merging neighbouring wrinkles (red arrows in Figure 5.1(b) and (c)); folds appear [90]. Indeed, it is found that the length of wrinkles or folds on the x-y

view is limited, which is due to the existence of closed shape that induces additional geometrical confinement.

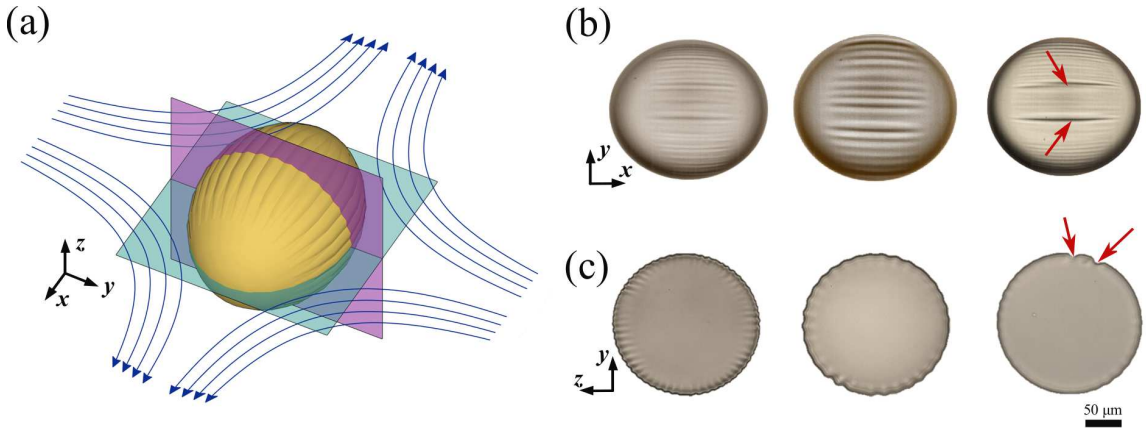

Figure 5.1: Wrinkling and folding on capsule membrane induced by a planar extensional flow. (a) Schematic of stretching the microcapsule in the flow with two perpendicular observation views. (b) Micrograph of capsules with well-defined wrinkles and local folds on the membrane in x-y view. (c) Micrograph of capsules profile in y-z view. The red arrows indicate the occurrence of folds under further stretching the capsule.

In our observation, when the applied flow stress $\sigma \sim \sigma_c$, a critical stress, the membrane of capsule buckles suddenly into multiple undulations, thereafter grows from the centre towards two ends in x-y view as flow strength increases. Whereas, the areas near two the ends of a deformed capsule always keep smooth. This is the result of the two-end areas under positive tension, due to the curved and closed geometry.

To confirm the stretching and compressing area on the deformed capsule, we consider a geometry in Figure 5.2(a), in which the capsule has an ellipsoid-like shape constructed by the axes L, S and W. The volume of capsule is considered as conservative during deformation, due to no mass transfer through the membrane. During deformation, the membrane surface area can be dilated.

We monitored the perimeters, P_{LW}, P_{LS} and P_{WS} of the three principle cross sections with the axes L, W and S, as a function of the capillary number Ca (Figure 5.2(b)). It is found that P_{LW} increases with the increasing of Ca while the P_{WS} decreases and the P_{LS} almost keeps constant. This is consistent with the prediction of asymptotic theory in Equation 2.6 for $Ca < 0.04$. We thus conclude that the compression is near the meridional loop P_{WS}, while it is under stretching along the latitude loop, maximum at the equator loop P_{LW}.

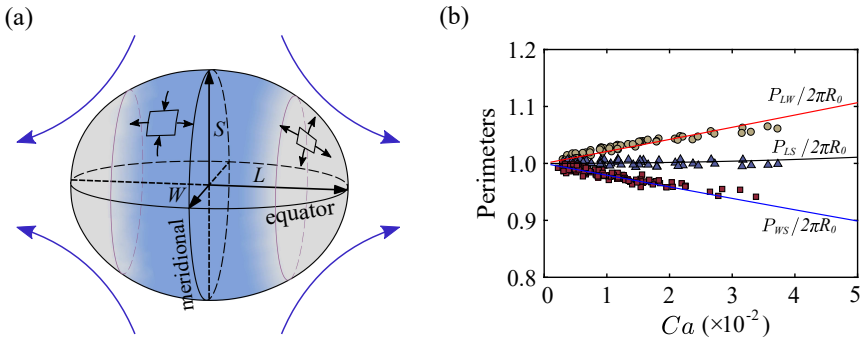

Figure 5.2: Stretching-induced compression on the ellipsoid-like capsule surface. (a) Schematic of compressing and stretching areas on the deformed capsule. Light blue area indicates the negative tension happening ($T_2 < 0$) due to external flow stretching. However, the rest area at two tips are under tension omnidirectionally ($T_1 > 0, T_2 > 0$), where T_1 and T_2 are along the equatorial and meridional directions, respectively. Equatorial loop: L-W; meridional loop: W-S. (b) Scaled perimeters as a function of capillary number Ca. The perimeter P_{LS} and P_{WS} were directly measured from two views, while the P_{LW} was estimated by assuming $W \approx R$ in small deformation (Appendix F). The solid lines are theoretical prediction of Equation 2.6.

However, only taking the perimeters into account cannot explain no wrinkles at the two tips of the deformed capsule. We further consider the curved and closed geometry. It has been observed that compressing a flat sheet from two parallel boundaries produces wrinkles which cover the entire sheet [90, 91]. This is due to weak geometric boundaries confinement. In contrast, on a capsule, curved surface modifies the distribution of stress tension. In small deformation, the principal tensions in membrane are given by [56]

$$\frac{T_{11}}{G_s} = 5Ca\cos(2\phi), \quad \frac{T_{12}}{G_s} = -5Ca\cos\theta\sin(2\phi), \quad \frac{T_{22}}{G_s} = -5Ca\cos^2\theta\cos(2\phi) \tag{5.1}$$

where ϕ and θ are the defined in spherical coordinates. $\theta = \pi/2$ corresponds to the extensional plane L-S, and $\theta = 0$ corresponds to another plane L-W. For the L-W plane, non-zero principle tensions become $T_1 = -T_2 = 5Ca\cos(2\phi)$. Thus, the negative tension only occurs in the range of $\phi \in (\pi/4, 3\pi/4) \cup (5\pi/4, 7\pi/4)$, a region close to the meridional loop. In the area of two ends, all stress tensions show positive value. In further step, we can define the curvature [169] at the ends of a deformed capsule,

$$\Omega = \frac{1}{r} \tag{5.2}$$

where r is the radius of equivalent circle at two ends. Large value of Ω at the ends

vanishes the negative tension. Following this, we speculate that the wrinkling extent on the deformed capsules would be decreased in large deformation, and eventually vanished, which will be discussed in Chapter 6.

5.3 Wrinkling at threshold

As mentioned above, a capsule deforms into an ellipsoid-like shape accompanied with wrinkles on the surface. In Chapter 2, we have discussed that before achieving steady-state deformation it is time-dependent arising from the competition between the membrane and flow. Similarly, the development of wrinkles also shows time dependence during the deformation (see Figure 5.3). We define a characteristic arc length Λ_w of wrinkling extent to describe the wrinkles development (see details in Appendix F). When the deformation is approaching the steady state, the capsule surface is wrinkling with a growing characteristic length, and eventually reaching a stable length (red rectangles in Figure 5.3). In the following, the characteristic length achieves the steady-state value.

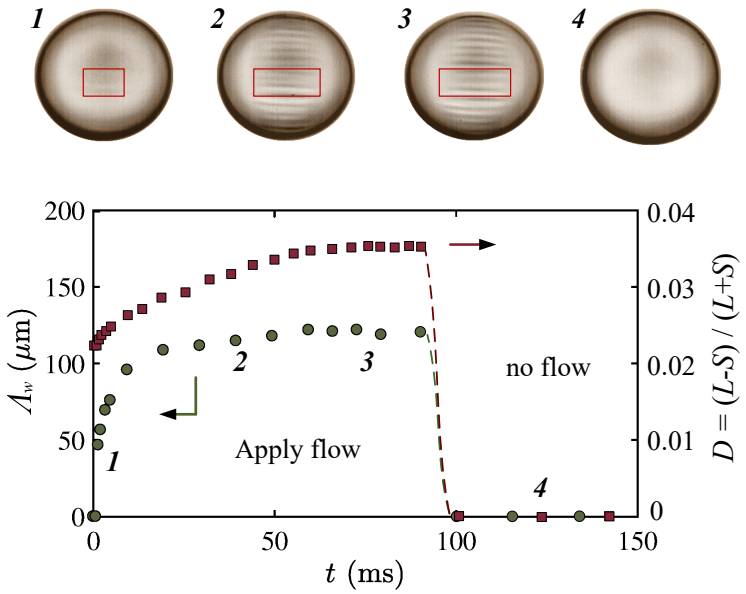

Figure 5.3: Time-dependent development and recovery of capsule deformation and wrinkling. When the extension flow is applied, both the deformation D and wrinkling length Λ_w grow until approaching the plateaus, and fully developed wrinkles are concurrent with the steady-state deformation. When the load is removed, the capsule recovers back to its spherical shape without wrinkles and residual deformation. The red boxes show the wrinkling length growth. Note that the characteristic length is the arc length (calculation in Appendix F).

To examine whether the wrinkling is reversible and reproducible, we stopped the flow and retrieved the capsules after deformation. It is found that all the capsules recover to their initial unwrinkled state without membrane flab, indicating that the membrane is mainly elasticity-determined (Figure 5.3).

In this section, we mainly focus on the onset and development of wrinkling of capsules with various membrane properties, as well as the transition between well-defined wrinkles to localized folds. A critical scaling law and stability phase diagram will be obtained.

5.3.1 Critical wrinkling stress

We now quantitatively focus on the critical wrinkling stress on capsules, $\sigma_c = \eta\dot{\epsilon}_c$. We, here, mainly consider the effects of membrane thickness and capsule size. To do that, we deform capsules with various size ($R \approx$ 30-350 μm). Smaller and bigger capsules, which are out of the size range, were not investigated in our work, due to the limitations of capsules fabrication and flow chamber configuration. Small capsules are found to delay the wrinkling instability. Quantitatively, the critical stress is found scaled as $\sigma_c \sim 1/R$ for a given membrane stiffness (Figure 5.4(a)). This can be explained that smaller size of capsule induces stronger geometric confinement, requiring larger elastic energy to deform.

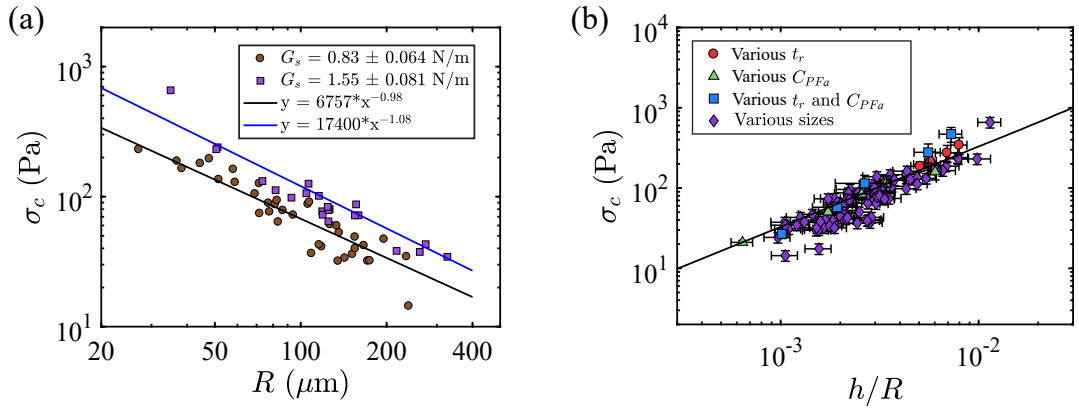

Figure 5.4: Critical wrinkling stress. (a) The critical stress σ_c plotted with various initial size for two membrane shear rigidity. (b) Critical stress σ_c plotted with thickness-to-radius ratio h/R for capsules assembled membrane in different controlled parameters. The line is least-square fitting result.

Although the membrane has small thickness ($h/R \ll 1$), the bending modulus can not be neglected in practice. The thickness is thus another important parameter dominating wrinkling emergence. In Figure 5.4(b), the critical stress is found to be scaled as

$\sigma_c \sim h/R$, which is consistent with the observation of critical buckling of a thin sheet surrounding on a stiff cylinder [170]. Thicker membrane thus has high ability to inhibit the wrinkling by increasing the resistance for bending.

Our results show the necessary condition for membrane wrinkling occurrence on initial spherical capsules; this provides not only experiment foundation for existing numerical models [13, 56, 88], but also some strategies on how to control morphology of close-curved surfaces in applications, for example, biofilm synthesis[171] and drug carry-release system [172].

5.3.2 Onset and development

We next quantify the onset and development of the wrinkles on capsules with different sizes and shear moduli (Figure 5.5). For capsules with the same initial radius, the final wrinkles length stops growing at the same plateau ($\Lambda_w \approx 170$ μm for $R \approx 95$ μm). The onset of wrinkling, however, is dependent on the membrane shear resistance. Large value of G_s requires large flow stress (Figure 5.5(b)). To check initial geometry effect, we stretched a set of capsules with radii in the range of $R \approx$ 40-250 μm but with approximately same membrane shear modulus. We found that large capsules are more susceptible to be wrinkled, and have large wrinkling area on the surface. Therefore, we may conclude that both the initial geometrical confinement and membrane shear resistance have influence on the onset and development of wrinkles.

Considering the flow stress and the membrane compliance together, we now show the extent of wrinkling zone, but for a number of capsules of varying shear resistance and size, plotted versus the capillary number Ca (Figure 5.5(c)). The data collapse well into a master curve for Ca < 0.04, indicating that the onset and growth of wrinkling eventually can be determined by the Ca. We found that capsules begin to wrinkle almost at the same capillary number, $Ca_c^w \approx 0.01 \pm 0.003$, independence on the size and shear elasticity. Again, we recall here the deformation studied for capsules is small (Large deformation will be discussed in Chapter 6). Folds are observed when the capillary number is approximately larger than 0.02.

In the early stage of wrinkling ($Ca_c^w < Ca < Ca_*$), we plot the wrinkling length $\log \Lambda_w/R$ as a function of $\log(Ca - Ca_c^w)$ (Figure 5.5(c) insert), where the Ca_* is around twice larger than Ca_c^w. By fitting the experimental data, we find that it follows well $\Lambda_w/R \sim (Ca - Ca_c^w)^n$ with n = 0.18 $\pm$ 0.04. We define the wrinkling occurrence in this range as Near Threshold (NT). For $Ca > Ca_*$, it is gradually divergent from the fitting relation above. If the $Ca \gg Ca_c^w$, we defined it as the Far from Threshold (FT) (discussed in Chapter 6). In this chapter, we mainly discuss membrane wrinkling in

the NT regime. According to our experiment, the value $Ca_* \approx 0.022$, and it corresponds to the Taylor parameter $D_* \approx 0.12$, which is within the linear deformation [13].

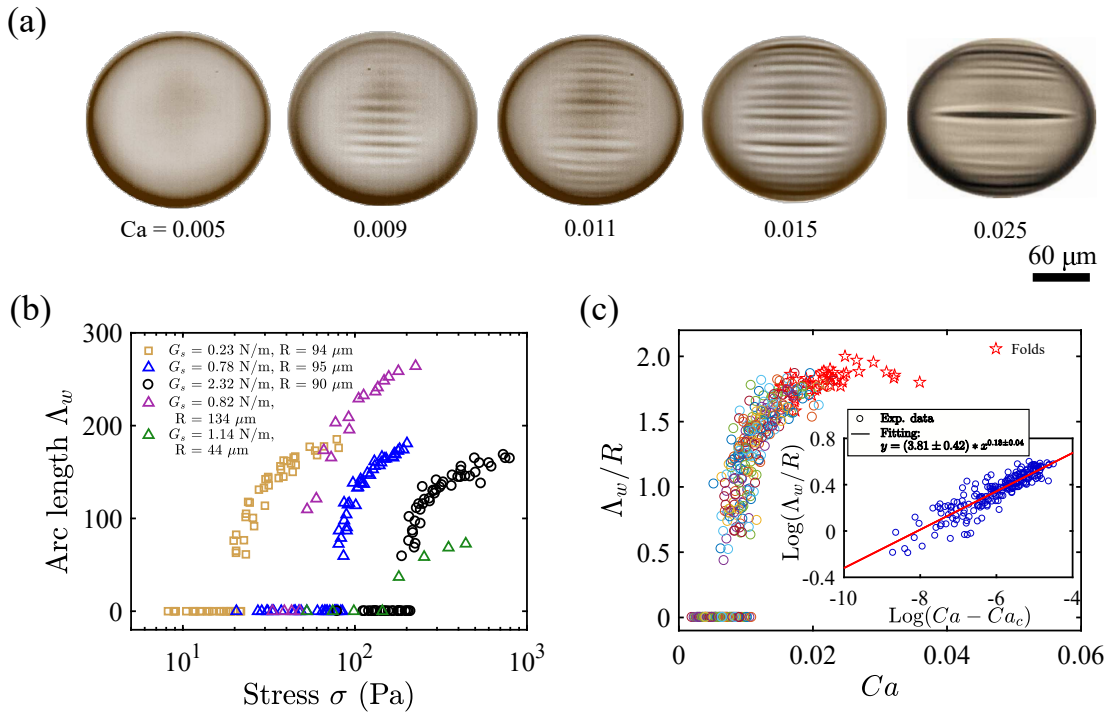

Figure 5.5: Onset and evolution of steady-state wrinkling. (a) Micrographic images of a capsule with time-independent deformation and full-development wrinkling at different Ca number. An apparent fold occurs localizing the membrane at Ca = 0.025. (b) Wrinkles arc length Λ_w plotted versus imposed viscous stress σ for capsules with different shear resistance and size. Arc length Λ_w = 0 represents membrane stable. (c) Scaled arc length Λ_w/R plotted with capillary number Ca. Inset: scaled wrinkling length plotted at $Ca \lesssim 2Ca_c^w$, where mostly the deformation $D < 12\%$.

The limited length of wrinkles on capsules observed in our experiment is $\Lambda_w/R \approx$ 1.78. Wischnewski and Kierfeld [173] deduced an asymptotic value of central angle ϕ_w following $\cos^2(\phi_w) = 5/9$ where wrinkling happening for ferrofluid-filled capsules in magnetic fields. If we consider the length of wrinkled region is $\Lambda_w = R_0\ (\pi - 2\phi_w)$; $\phi_w = \pi/2$ means no wrinkling. We can know the limited length in their work is $\Lambda_w/R \approx$ 1.68, which is a little lower than our result. This is attributed to that we estimate the arc length of wrinkling based on arc length on the deformed capsule (see Appendix F).

In Figure 5.5(b) and (c), some points seem to miss at the place where it is very close to the threshold of wrinkling. Several explanations can be provided. Firstly, it is mainly due to the way of applying flow and the limit of resolution of the fast camera. The amplitudes of wrinkles are too small to be visualized ($\sim 1\ \mu$m, see Figure F.2 in Appendix

F), and the optical contrast is too weak to visualize the black lines along the stretching axis. Secondly, the jump in the wrinkling length is physical arising from the nature of bifurcation. Indeed, if the bifurcation is subcritical, it is well known that the order of the parameter jumps from one branch (no wrinkles) to another for the solutions (Figure 5.6(b)). However, the wrinkling instability is usually considered as supercritical in many examples, such on a semi-spherical shell [174]. Moreover, preliminary numerical results show that this instability is supercritical in our configuration (data not shown). Thirdly, the jump is due to the confinement. Indeed, a microcapsule is under compression in the azimuthal direction (meridional loop direction in Figure 5.2(a)), when the flow is applied, even small. The domain of compression grows from a finite value which determines the initial length of wrinkles as discussed in Equation 5.1). In our opinion, this geometrical argument is the most plausible explanation.

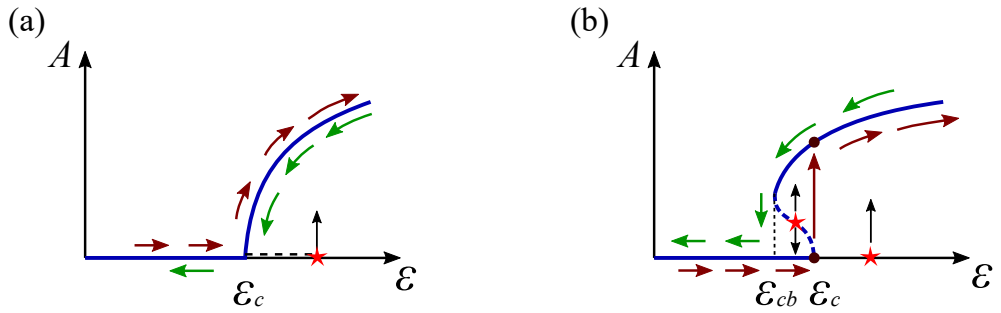

Figure 5.6: Illustration of pitchfork bifurcations, increasing step by step the control parameter ε from zero (stable system) up to the values larger than the threshold ε_c. (a) Supercritical. (b) Subcritical. The red stars are the points where the strains are applied.

5.4 Phase diagram

In context, membrane wrinkling on a capsule involves the imposed flow, membrane shear stiffness and geometrical confinement. Taking together, we can summarize in a phase diagram, as shown in Figure 5.7. For a given membrane shear modulus (G_s), capsules keep stable, showing no wrinkles if the $\sigma R < \sigma_c R_c$. However, well-defined wrinkles appear when the value of σR is large enough. In further, localized shape deformation, folding, might appear. Therefore, during the deformation, there exist two transitions: smooth-to-wrinkles and wrinkles-to-folds. Large membrane rigidity G_s requires large value of σR to show wrinkles or folds.

For the first transition, it is found that all the capsules begin to wrinkle at a same slope $\sigma R/G_s$, which is indeed defined as the capillary number Ca. In accordance with

Figure 5.5(c), the critical slope $Ca_c^w = \sigma_c R_c/G_s$ is constant, and approximately 0.01 $\pm$ 0.003, independent on the shear modulus and thickness.

The second transition, wrinkles-to-folds, appears in order to lower the global energy of the system via the localization of strain. This process enhances the local amplitude of wrinkles, but erases the neighbouring wrinkles, which is more complicated due to the strong nonlinearity. Similarly, it is found that the onset of wrinkles-to-folds transition does not explicitly depend on membrane stiffness. There seems to be a critical value, capillary number $Ca_c^f \approx 0.019 \pm 0.004$ instead.

However, experimentally it is difficult to conclude the transition of wrinkles-to-folds is supercritical or subcritical because they coexist at the threshold (Figure 5.7 and Figure 5.1(b),(c)). For large G_s (> 5.0 N/m), capsules are too stiff to deform. Limited by our experiment set-up, we cannot stretch such capsules more until the wrinkles-to-folds transition.

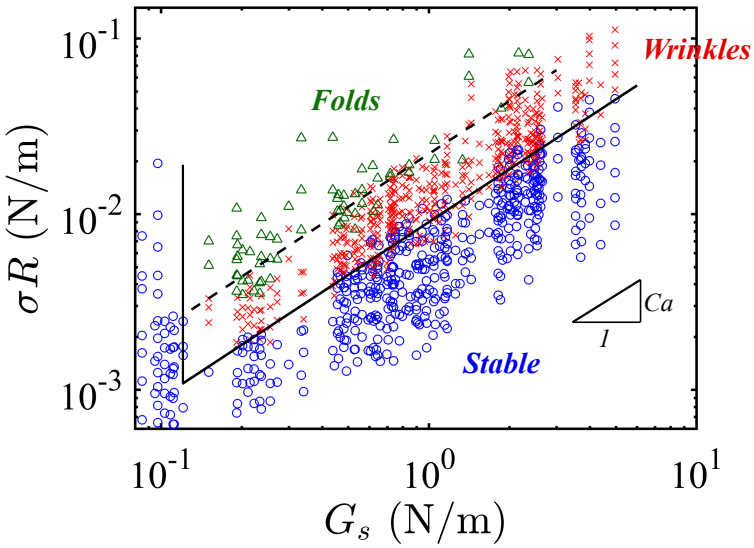

Figure 5.7: Phase digram. Blue circles: stable, no wrinkles; red crosses: well-defined wrinkles; green triangles: folds. The slop represents capillary number, $Ca = \sigma R/G_s$. Solid line: Ca_c^w = 0.01; dashed line: Ca_c^f = 0.021. On the left of vertical line, capsules are found always stable.

The transition of a curved membrane instability has been reported in axisymmetrical configuration [168, 175, 176]. Here, we define the Foppl-von-Kármán (FvK) number κ^{-1} as

$$\kappa^{-1} = \left(\frac{G_s R^2}{B}\right) \tag{5.3}$$

which is the stretching energy relative to the bending energy, where $B = Eh^3/[12(1-\nu^2)]$ is bending modulus of membrane, and h is the thickness. We assume that the

Poisson ratio $\nu = 1/2$ in our case. The large value of FvK number means that the membrane is more easily bent.

In the range of large value of κ^{-1}, which is corresponding to the small G_s in Figure 5.7, we find small wavelength of wrinkles. When the $\kappa^{-1} > 10^8$, capsules are found no wrinkling instability on the surface no matter how large the flow stress is (left of the vertical line in Figure 5.7). In this range, the $G_s < 0.1$ N/m. The interfacial tension of liquid-liquid droplet (same as capsule phase) is around $\gamma \approx 0.022$ N/m (see Appendix F). The shear modulus G_s and interfacial tension perhaps have the same order of magnitude. The membrane, thus, exhibits high extensibility responding to the stretching or compressing, which in return vanishes all tangential strains. Consequently, only in-membrane deformation happens, no out-of-membrane bending. This is also consistent with the general knowledge that a water droplet in the oil phase never show the interface wrinkling in deformation [14].

Oppositely, small value of κ^{-1} is corresponding to the large G_s, where the membrane has high stiffness. When the $\kappa^{-1} < 5 \times 10^4$, we cannot observe the wrinkles-to-folds transition. We hypothesize there exist two cases. One is that the critical capillary number of wrinkles-to-folds transition Ca_c^f is increased, and our experiments have not achieved that threshold value. Another one is that the residence time of the capsule at flow stagnation point is not long enough to fully develop the wrinkles. It, perhaps, takes time to trigger the wrinkles-to-folds transition [97]. Again, limited by our experiment set-up, it is difficult to trace the time-dependent transition.

5.5 Wavelength and wave number in NT

Thanks to the direction visualization of wrinkling profile (y-z view), we now quantify the well-defined wrinkles characterized by wave number N_w and wavelength λ_w (Figure 2.11). The wavelength is mainly measured in the NT regime, where the Ca ranges from 0.008 to 0.02, smaller than the Ca_* (≈ 0.022). Note that the we only measure the wavelength at the meridional loop (W-S plane) which is weakly influenced by the confinement at the end boundaries.

We define a small deflection $\xi \ll R$ on the membrane when wrinkling occurs. The stretching and bending energy per unit area on the membrane can be written as

$$U_s \sim T\left(\frac{\partial \xi}{\partial x_1}\right)^2 \quad \text{and} \quad U_b \sim B\left(\frac{\partial^2 \xi}{\partial x_2^2}\right)^2 \tag{5.4}$$

respectively, where x_1 and x_2 are the directions along equatorial loop and meridional loop (in Figure 5.2(a)). B is the membrane bending modulus, while T is the tensile tension, $\sim CaG_s$ at the meridional loop according to Equation 5.1. Although the bending energy U_b is much smaller than the stretching energy U_s, typically $U_b/U_s \sim \mathcal{O}(10^{-6})$, the increasing for U_b is as expected two-order larger than U_s when the thickness grows, due to $B \sim \mathcal{O}(h^3)$ while $T \sim \mathcal{O}(h)$. Hence, bending energy U_b progressively plays conspicuous roles in thick membrane, which is in accordance with our observation that capsules with thick membrane exhibit more stable when elongated. Figure 5.9(a1-a5) show the various wavelength on different thickness of capsules.

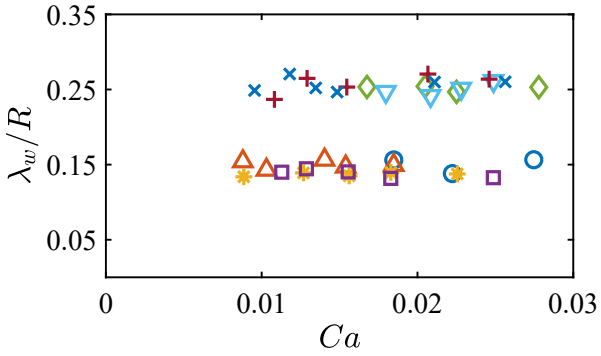

Figure 5.8: Wavelength as a function of Ca. Two typical wavelength are plotted. Each symbol represents a capsule. Wavelength is determined by the arc length between neighbouring peaks (see details in Appendix F).

If we assume that wrinkles around the meridional loop have a sinusoidal undulation with amplitude A_w and wavelength λ_w, Equation 5.4 can be simply scaled as $U_s \sim T\left(\frac{A_w}{R}\right)^2$ and $U_b \sim B\left(\frac{A_w}{\lambda_w^2}\right)^2$. Balancing these two energies [90] gives the wavelength of wrinkles as

$$\lambda_w/R \sim \left(\frac{B}{G_s R^2}\right)^{1/4} \tag{5.5}$$

where the tension $T \sim G_s$. In the small deformation, the Ca has no influence on the wavelength (Figure 5.8). For a homogeneous material, the bending modulus $B \sim G_s h^2$, we can rewrite Equation 5.5 in the form of $\lambda_w \sim \sqrt{hR}$, which is similar to the theoretical analysis [12, 96].

As shown in Figure 5.9(b), for a given size of capsules, e.g., $R \approx 95$ μm, the average wavelength is scaled well as $\lambda_w \sim h^{0.49}$, which is consistent with above scaling law. The wave number of wrinkles on thicker membrane will be decreased due to $N_w \sim 2\pi R/\lambda_w$, as shown in Figure 5.9(a). However, the amplitude of wrinkles A_w is too small to detect from image processing in our experiment ($A_w \approx 1\mu$m, while the resolution of our camera is 0.851 μm/pix for magnification x20). We did not observe

obvious difference for amplitude in given membrane properties of capsules during deformation. According to the study of Cerda and Mahadevan [96], amplitude is scaled as $A_w \sim \lambda_w \varepsilon^{1/2}$, where ε is the strain. Probably, we can detect the amplitude variation for large wavelength by applying high compression and using high resolution photography.

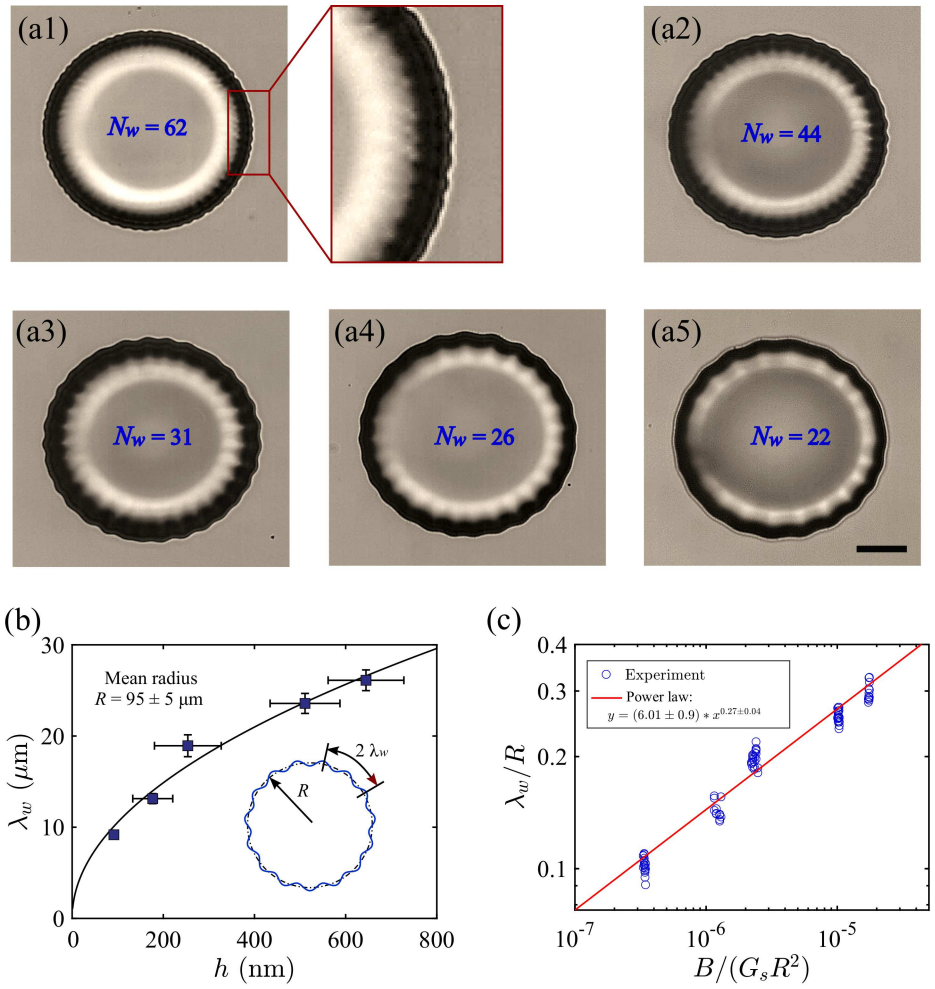

Figure 5.9: Wavelength of wrinkles in the NT regime. (a) Micrographic images of capsule profile at the meridional loop (P_{WS}). a1-a5 correspond to the points in (b) from small to large thickness, respectively. The wave number shown on images is counted manually. Scale bar: 45 μm. (b) Average wavelength as a function of capsule membrane thickness. The radius of capsules is around 95 μm. Solid curve is the experimental data fitting: y = 1.1*$x^{0.49}$. Insert: illustration of wavelength. (c) Scaled wavelength as a function of membrane stiffness.

Scaled wavelength is shown in Figure 5.9(c), relating to the stiffness of membrane. We find the experimental data are close to the scaling $\lambda_w/R \approx 2\pi[B/(G_s R^2)]^{1/4}$. Since

there are no wrinkles at the two ends, there exist decreasing transition both for wavelength and amplitude along the equatorial direction. But, the wave number is fixed (no folding).

5.6 Discussion and conclusion

We present membrane wrinkling instability on CHT/PFacidYN microcapsules induced by stretching in a planar extensional flow. Well-defined wrinkles originate from the middle section of capsules (meridional loop), and expend towards the two ends, characterized by scaled length Λ_w/R. However, limited by the curvature at the ends, the length growth stops at $\Lambda_w/R \approx 1.78$ in our observation. Physically, wrinkles appear when the in-plane deformation cannot support the transverse strain because of the limit of the extensibility of membrane. Energetically, bending out of membrane deformation induces the bending energy but releases the stretching energy. Thus, we might observe the relaxation of compression when wrinkles appear. However, in our experiment we did not observe an obvious relaxation of the perimeter P_{WS} after wrinkles appearance. We think that this is due to the wavelength for CHT/PFacidYN capsules is too small (less than 30 μm), and the variation is likely within the experimental measurement error.

At the critical condition, wrinkling stress is found to be scaled as $\sigma_c \sim h/R$ on capsules. However, this is different from the theoretical prediction, $\sigma_c \sim E(h/R)^2$, in shear flow [12]. We think that this is due to the flow types. In dimensionless, capsule membrane are found to begin wrinkling at a constant capillary number, $Ca_c^w \approx 0.01 \pm 0.003$. In further stretching, folds appear at $Ca_c^f \approx 0.019 \pm 0.004$. The phase diagram of instability proposed in our work suggests a scalable route for predicting membrane wrinkling on intrinsically spherical objects, for example biological cells [92] and bacteria [177], when they are exposed to external constraints.

By simply balancing stretching and bending energies, wavelength laws are obtained, which is in accordance with the general description by Cerda and Mahadevan [96]. For a given size of capsule, $\lambda_w \sim h^{1/2}$. In scaled, it is found $\lambda_w/R \sim [B/(G_s R^2)]^{1/4}$, relating to the stiffness of capsule membrane. Interestingly, we find that wavelength has little dependence on the Ca in the NT regime. This, however, might be not true for the large deformation in the FFT regime.

Folds on capsules are found different from those on flat sheet (Figure 5.10). On flat sheet, extremely large strain leads to very deep folds (also referred to as creases), with large localized amplitude. However, this is not observed on microcapsule. We think that on one hand the curved-closed surface induces additional confinement to weaken

the growth of folds; on the other hand, deep folds consume relative large amount of membrane, while to sustain the closed shape, the reservoir of membrane is finite.

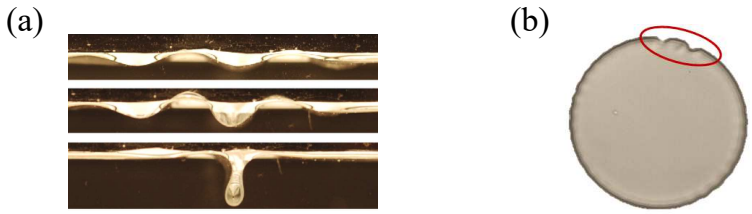

Figure 5.10: Comparison of folding on flat sheet and on capsule. (a) A polyester film floating on water under compression[90]. (b) Two folds forming on capsules (in the red area). Radius of the capsule is around 97 μm.

Our work demonstrates the membrane wrinkling instability dependence on the flow and membrane stiffness for thin-shell spherical microcapsules. It might provide an alternative strategy for characterizing the deformable particles via wrinkling features, for example thickness and bending stiffness. In application, wrinkling might be helpful to develop a new approach to diagnose and filtrate living cells in bioengineering. Moreover, it gives quantitative model for numerical simulation [13, 55, 65], where the membrane bending resistance is often neglected.

Summary

- The wrinkles originate at the middle section (meridional loop) of the capsule, and propagate towards two ends.
- Curved-closed geometry limits the growth of wrinkling extent.
- Critical wrinkling stress is scaled as $\sigma_c \sim h/R$.
- In the range of our experiment, capsules are found to begin well-defined wrinkles at Ca_c^w = 0.01 $\pm$ 0.003, and wrinkles-to-folds transition at Ca_c^f = 0.091 $\pm$ 0.004.
- Well-defined wavelength is scaled as $\lambda_w \sim h^{1/2}$ or $\lambda_w/R \sim [B/(G_s R^2)]^{1/4}$, independence on the Ca in the NT regime.

Chapter 6

Wrinkling instability in the Far-from-Threshold regime

Contents

6.1 Introduction

In the Chapter 5, we mainly discussed the wrinkling instability of capsules in the limit of small deformation. However, wrinkling features might be changed if the deformation is large, as shown in Figure 6.1, where we define it as Far-from-Threshold (FT) regime. Since CHT/PFacidYN capsules have relatively large shear modulus (see Figure 3.9), resulting in more stiff, it is difficult to achieve large deformation for thick membrane. We thus stretch the HSA/TC capsules which have lower shear modulus, to investigate the wrinkling development from the NT to FT regimes (small to large deformation).

In this chapter, we will focus on the HSA/TC capsules wrinkling from the NT to the FT. In the NT, we check the universality of results of CHT/PFacidYN capsules obtained in Chapter 5. While in the FT regime, we focus on the second bifurcation of wrinkling as well as the wavelength.

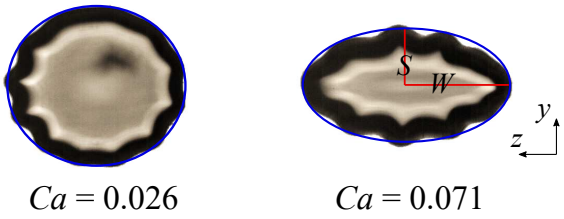

Figure 6.1: Wrinkling profiles from Near-Threshold (NT) to Far-from-Threshold (FT) regions at the meridional loop of a HSA/TC microcapsule. Left: NT. Right: FT.

6.2 Relaxation of compression

As discussed in the section 5.2, capsule membrane shows wrinkles to release the compression energy, but inducing the bending energy. Consequently, the compressed membrane would relax. However, due to small wavelength of CHT/PFacidYN capsules, it does not allow to detect this relaxation process. To verify the hypothesis, we stretch several HSA/TC capsules which have different shear moduli. By image processing, we can extract the perimeter of wavy boundary on the W-S view (Figure 6.1). The perimeter variation at the meridional loop P_{WS} is plotted in Figure 6.2. We find that the perimeter decreases gradually for all the capsules before wrinkles appear (Ca < Ca_c). For the capsules without wrinkles, the perimeter P_{WS} is found continuously decreased (black squares in Figure 6.2). Once the wrinkles appear, an increase of P_{WS} is observed. This is the signature of the wrinkling instability which relaxes the azimuthal compression. It is worthy to note that the relaxation might not make the loop release all the compression because in most cases the perimeter is smaller than that without deformation (Ca = 0).

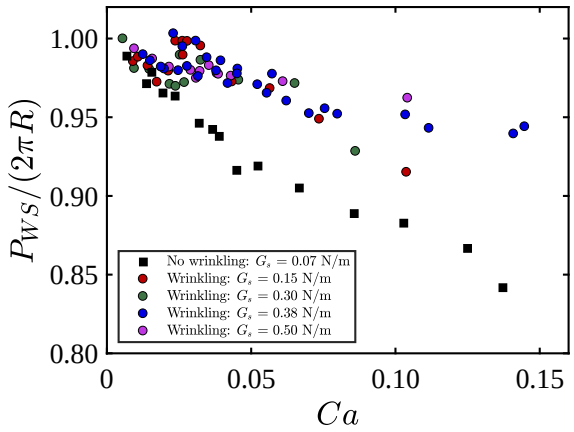

Figure 6.2: Scaled perimeter P_{WS} at the meridional loop as a function of capillary number Ca. Wavelength $\lambda_w \approx$ 40-70 μm.

With further stretching (at high Ca), we found that loop perimeter for wrinkling cases appears to stop decreasing with Ca, after which wrinkles might disappear (discuss later). If continuously stretched, the membrane rupture might occur (Chapter 4). In contrast, membrane without wrinkling shows non-stop decreasing of the loop perimeter.

6.3 Wrinkling length development

In Chapter 5, wrinkling length grow towards two ends of capsules, but saturated by the geometric confinement for CHT/PFacidYN capsules. In the NT regime, we observed the similar process for HSA/TC capsules; wrinkling length of capsules with different shear moduli collapse well into a master curve in the range of $Ca < 0.04$. However, it begins to diverge when Ca is increased; the length decrease until being vanished completely (Figure 6.3(a)). Note that, the wrinkling length, L_w, here is the projected length on x-y plane (L-S), because the conversion of arc length used for small deformation (in Appendix F) is not suitable for large deformation.

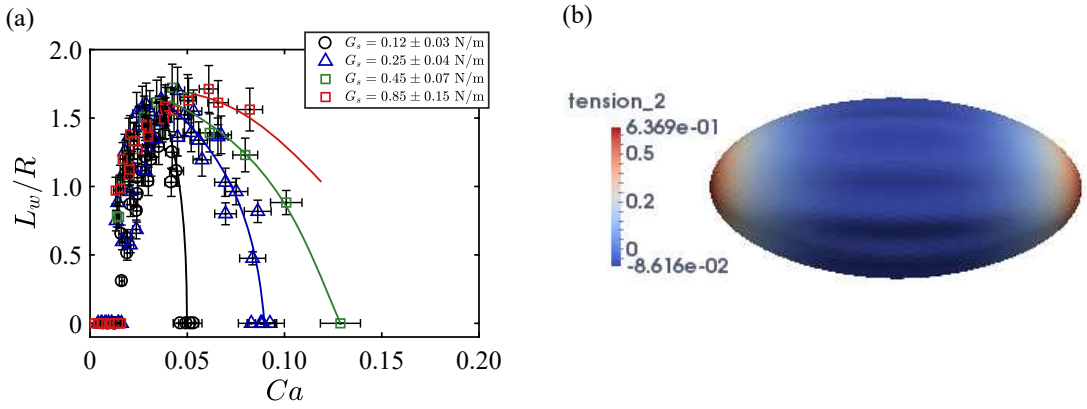

Figure 6.3: The development of wrinkling projected length in x-y plane with Ca and the tension distribution. (a) Before the lengths decay, they collapse into a general curve regardless of shear moduli. High enough Ca leads to vanishing the length. Error bars are 10% deviation. (b) Simulation result of azimuthal tension distribution in x-y plane (performed by M. Leonetti).

In large deformation, wrinkles are found to disappear, where the principal tensions in the membrane become positive everywhere, even near the meridional loop. As shown in Figure 6.3(b), the negative tension at the middle section of deformed capsule sustains the surface wrinkling. However, with increasing deformation, the area of negative tension is narrowed and finally vanished, followed by wrinkling length reduction to zero.

Experimentally, we observe the emergence of wrinkles on HSA/TC capsules at the critical capillary number, $Ca_c^w \approx 0.014$, which is close to the CHT/PFacidYN capsules. However, the second critical capillary number, Ca_c^d, where wrinkles disappearing seems to depend on the shear elasticity of membrane. Wrinkles can be vanished at low capillary number for capsules with low shear resistance membrane. While, wrinkles disappearing is inhibited for capsules with high shear resistance (Figure 6.3)(a). Before the wrinkles disappearing completely, the wrinkling length is decreased from the maximum value. The compression area is narrowed towards back the middle section of capsule.

6.4 Wavelength

In Chapter 5, we discussed the wavelength λ_w and wave number N_w at the meridional loop (middle section of capsules) in the NT regime, where the applied capillary number is not far from the critical one. In this section, we check the scaling laws obtained from CHT/PFacidYN capsules with HSA/TC capsules, working in the NT regime. Thanks to low shear resistance of HSA/TC capsules, we are able to deform them in the large range of deformation but with large wavelength (see Figure 6.5(a)). This makes it possible to study the variation of wavelength and number of wrinkles in the FT region.

6.4.1 In the NT regime

We plot the wavelength of HSA/TC capsules as a function of membrane properties in the NT regime, shown in Figure 6.4. As the deformation is small (in y-z view, close to a circle), wrinkles are distributed almost uniformly in the profile (Figure 6.5, Ca = 0.026). For a given size $R \approx 100$ μm, HSA/TC capsules follow the scaling $\lambda_w \sim \sqrt{h}$ with a prefactor 1.1. In dimensionless, the wavelength scaling is close to $\lambda_w/R \sim (B/G_sR^2)^{1/4}$, alternatively confirming the scaling in Equation 5.5.

Combining the result in Chapter 5, by fitting the experimental data both for HSA/TC and CHT/PFacidYN capsules, we obtain the relationship as following

$$\lambda_w/R \approx (5.7 \pm 0.65)\left(\frac{B}{G_sR^2}\right)^{0.27\pm0.04} \tag{6.1}$$

Compared to the wrinkles scaling of a flat polyethylene sheet [96], we have obtained different prefactors. This is probably due to different geometries. In our case, the capsule surface is closed and curved without free boundary. When it is stretched

in one direction above the critical value, the formed wrinkles spontaneously interplay each other which might redistribute the wavelength.

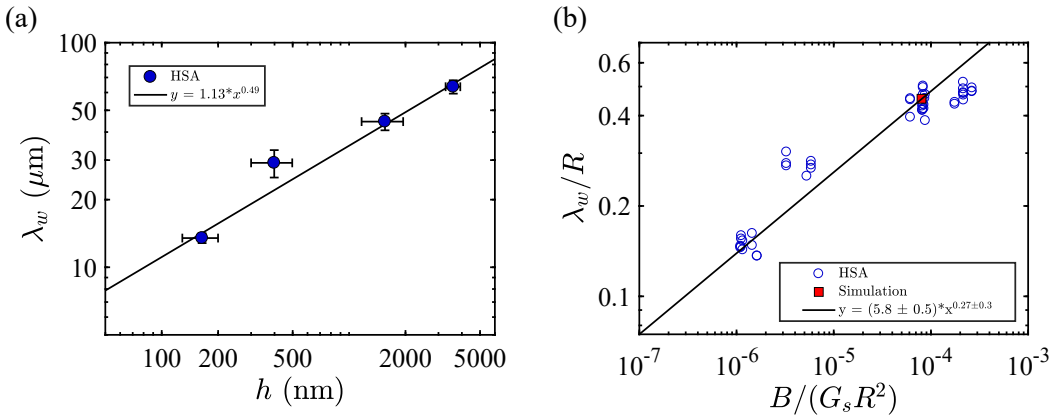

Figure 6.4: Wavelength of wrinkles in the NT regime. (a) Average wavelength as a function of membrane thickness. The radius of capsules is 92-110 μm. (b) Scaled wavelength. The simulation point is performed by M. Leonetti, which is consistent with our experimental result.

6.4.2 In the FT regime

When the applied capillary number is far from the critical value, it is defined as the FT regime, where the symmetrical wrinkles are broken, redistributing the undulations to adapt the compressing and stretching areas. An example of wrinkles evolution is shown in Figure 6.5(a). Sinusoidal wrinkles first appear almost homogeneously along the circumference when $Ca \gtrsim Ca_c^w$. The capsule has a slight deformation. However, large capillary number deforms the capsule more, resulting in modifying the distribution of stress field in membrane. Wrinkles are found to gradually vanish first at the two poles, and eventually at the mid-section area (the denotation of poles and mid-section is shown in the insert of Figure 6.6(a)). Larger deformation (Taylor parameter D_{WS}) results in higher curvature at the poles where global bending of membrane neutralizes the compression. We note that emergence of neighbouring wrinkles coalescence exists at the poles (Figure 6.5(a)), which decreases the number of wrinkles (Figure 6.5(b)). Nevertheless, initially when the capillary number is close to the first critical value, the number N_w is weakly dependent on Ca, until the first wrinkles collapse happen.

The reduction of wrinkles number is often accompanied with folds emergence which localizes the undulation by increasing the local amplitude [90, 175]. However, in our HSA/TC capsules we did not observe the obvious folds appearing at the poles when wrinkles collapse (amplitude is not seen going up a lot). We think that this is the joint result of increasing curvature at poles and membrane mechanical properties, when the

deformation is enlarged. Unlike folding in flat membrane, stress field modified by global curvature does not allow amplitude growth when wrinkles merge at poles. In contrast, in the mid-section part, wrinkles collapse occurs in the later stage where the Ca is extremely large (e.g., $Ca > 0.1$). As mentioned above, finally we believe that all wrinkles are vanished, due to membrane being under positive tension everywhere in very large deformation.

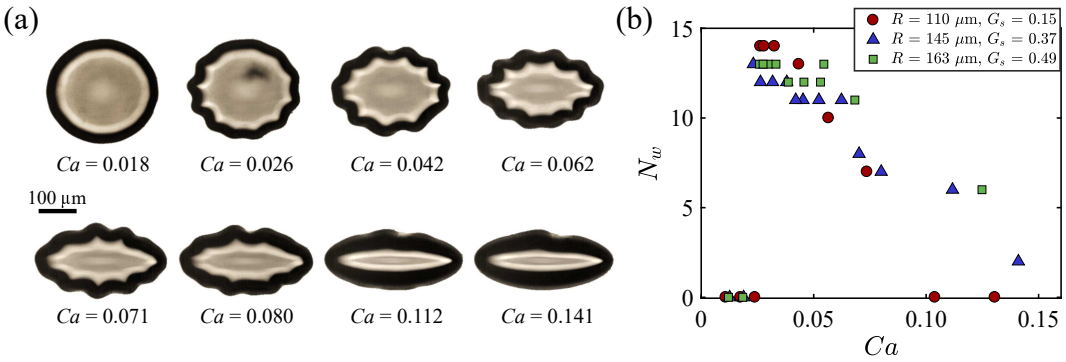

Figure 6.5: Wrinkling profiles and wave numbers. (a) Micrographic images of wrinkling profiles under different capillary numbers. (b) The number of wrinkles as a function of capillary number for different membrane surface shear moduli. We denote that zero means no wrinkles.

In Figure 6.6(a), we thus plot the mean wavelengths λ_{w1}/R and λ_{w2}/R at the poles and mid-section areas, respectively. As expected, wavelengths λ_{w1} and λ_{w2} have similar values when Ca is close to Ca_c^w. However, λ_{w1} and λ_{w2} gradually diverge in high Ca values; λ_{w1} decreases until no wrinkles at poles, while λ_{w2} remains almost constant before the entire surface becomes stable again.

In the FT regime, the capsules generally have large deformation in y-z view. The wavelength is thus not in accordance with Equation **??** and Equation 6.1; there is no general wavelength scaling law. The distribution of wrinkles on capsules is not uniform, as a result of interplay between wrinkles and curvature. In the axisymmetric extensional flow [178], the cross section (W-S plane) of deformed capsule has similar curvature along the circumference. The two wavelengths λ_{w1} and λ_{w2} might vary similarly with the capillary number.

A rough comparison between experiment and simulation is shown in Figure 6.6(b) and (c). At the same order of FvK number ($\sim \mathcal{O}(10^4)$) and Ca number (~ 0.07), numerical wrinkling profile has a good agreement with experimental image, only with slight difference at the poles. The numerical simulation was carried out using two-dimensional Hooke's law with assuming Poisson ratio $\nu = 0.4$. Quantitatively, the scaled wavelength at mid-section from simulation is $\lambda_{w2}/R \approx 0.45$, which is close to

the experimental measurement λ_{w2}/R shown in Figure 6.6(a). Simulation for small wavelength has not been carried out because it requires building very fine mesh to detect the small undulations of surface, in which the computation time is quite long.

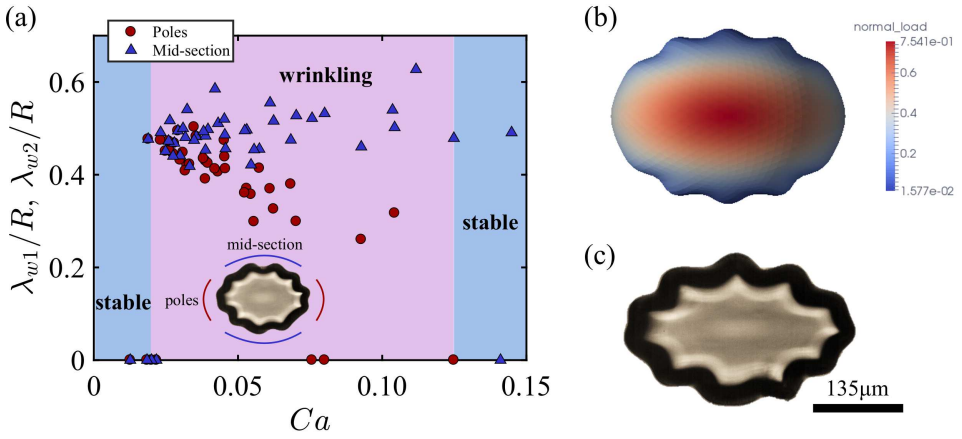

Figure 6.6: Wrinkling in FT region. (a) Scaled wavelength as a function of capillary number. We measure the wavelengths at poles and mid-section areas separately. λ_{w1} and λ_{w2} are corresponding to the poles and mid-section. The thickness of membrane h = 3.65 $\pm$ 0.75 μm. Zeros mean no wrinkles. (b) Rough simulation result of wrinkling profile at Ca = 0.07 and κ^{-1} = 1.2 $\times$ 10^4. Colours are the normal stress. (c) Micrographic image of a HSA/TC capsule at Ca = 0.068 and $\kappa^{-1} \approx 0.7 \times 10^4$.

6.5 Phase diagram

Similar to CHT/PFacidYN capsules, we plot the phase diagram of HSA/TC capsules in Figure 6.7. For a given shear modulus of capsule, the surface maintains stable if the σR is below the critical value. Wrinkles appear when the σR is large enough. In further stretching (large deformation), wrinkles disappear where the surface becomes stable again.

We found that at the first transition capsules begin to show wrinkles approximately at the same slope $\sigma R/G_s$, corresponding to the critical capillary number, Ca_c^w = 0.015 $\pm$ 0.004 (solid line in Figure 6.7). However, as discussed above, the second transition (from wrinkling to stable) occurs dependently on the stiffness of capsules. The critical capillary number, Ca_c^d, increases with the value of G_s. By fitting the experimental data, we found it follows the relation $\sigma R \approx 2.4\ G_s^{1.8}$. If we substitute the σR with the definition of capillary number $\sigma R = CaG_s$, we obtain $Ca_c^d \sim G_s^{0.8}$.

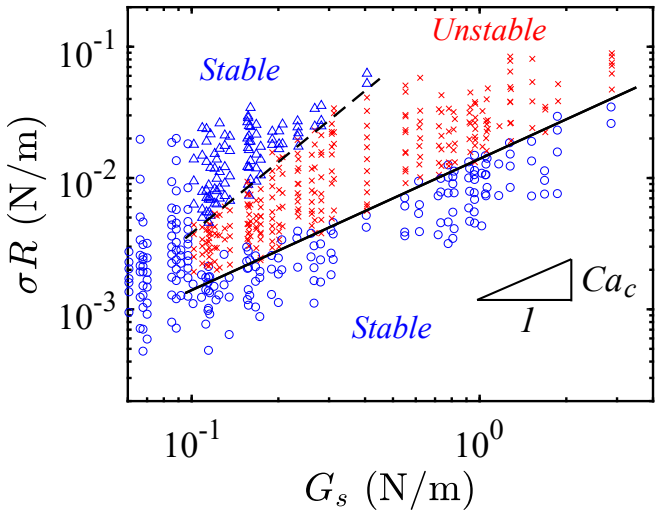

Figure 6.7: Phase diagram of HSA/TC capsules. For high G_s of capsules, we are not able to deform them up to large deformation where wrinkles disappear, due to the limit of the maximum flow rate of our pump. Blue circles: no wrinkles; red crosses: wrinkles; blue triangles: wrinkles disappearing. Solid line: Ca_c^w = 0.014; dashed line: $\sigma R \approx 2.4 G_s^{1.8}$.

In this phase diagram, we focus on the first instability in small deformation and re-stabilization in large deformation. Thus, we do not show the folding on HSA/TC capsules. Indeed, for the small value of G_s (corresponding to thin membrane), similar to CHT/PFacidYN capsules, we observe folding appearance on HSA/TC capsules. However, in large thickness, it is rare to observe membrane folding. We think that this is attributed to different material properties. For HSA/TC capsule, the membrane has several times of lower of Young's modulus than that of CHT/PFacidYN capsule (see Figure 3.9). But, the thickness of HSA/TC membrane is generally larger than that of CHT/PFacidYN. This leads to large value of inverse FvK number of HSA/TC membrane (see Figure 7.1). Membrane bending to localize deformation becomes more difficult [90].

6.6 Discussion and conclusion

Following the study in Chapter 5, we investigate the wrinkling on another wall material of capsules, HSA/TC, from the NT to the FT regimes. In the NT, wrinkles development on HSA/TC capsule has the same behaviour as CHT/PFacidYN capsule in extensional flow; membranes begin to wrinkle approximately at a constant critical capillary number Ca_c^w, followed by the propagation of wrinkling length towards two ends. Wavelength is found to follow the scaling $\lambda_w/R \sim (B/G_s R^2)^{1/4}$ obtained

from CHT/PFacidYN capsules. Differently, in the FT regime, wrinkles are found disappearing at high capillary number; the critical capillary number Ca_c^d is dependent on the membrane stiffness. Wrinkles distribution is not uniform at the cross section, due to the interplay between wrinkles and curvature (curvature induced by the ellipsoidal deformation in y-z view). For HSA/TC capsules, apparent folds like observed on CHT/PFacidYN capsules have not been detected, but wrinkles merging was observed. Increasing curvature at the poles of cross section deformation vanishes the wrinkling and folds instabilities.

In the simulation work of Lac *et al.* [13] and Walter *et al.* [65], it is found that there exists a critical capillary number Ca_L, above which the membrane is stable, no compression, in the extensional flow. For the membrane obeying neo-Hookean (NH) law, Ca_L = 0.14, while for SK (C = 0.5) the Ca_L = 0.21. However, in our experiment we found that the wrinkles can disappear at $Ca_c^d \approx 0.05$ for low value of G_s. For stiffer membrane (large G_s = 0.45 N/m), the wrinkling disappearance happens at $Ca_c^d \approx 0.15$. Note that those simulations do not consider the membrane bending resistance, thus can not describe the physical wrinkling instability.

Summary

- Wrinkling on CHT/PFacidYN capsules obtained in the NT regime have been checked by HSA/TC capsules; wavelength and wrinkling length for both kinds of capsules have similar features.
- In the FT regime (large deformation), wrinkles are found disappearing. But, the critical capillary number Ca_c^d is dependent on the membrane stiffness.
- In the FT regime, wavelength distribution at the cross section is not uniform, with increasing of capillary number. Wrinkles merging has been observed at the poles.

Chapter 7

Conclusions and perspectives

Contents

7.1 General conclusions

This dissertation focuses on the capsules fabrication and their mechanical instabilities in a planar extensional flow. We have proposed a simple strategy to assemble monodispersed microcapsules surrounded by elastic membrane with tuning mechanical properties in a large range. The initial size of capsules is controlled by microfluidics. In the flow, capsules are deformed into ellipsoidal shape with stable surface, if the flow capillary number is low. Once the capillary number is above the critical value, Ca_c^w, capsules exhibit well-defined wrinkles along the azimuthal direction. Wrinkling length grows towards the two ends, originating from the centre of capsules, when the capillary number increases. However, if the capillary number is greater than the second critical value, Ca_c^d, wrinkles are vanished, surface becoming stable again. Membrane rupture happens, when the capillary number is extremely large where the capsules are elongated into very large deformation ($D > 0.7$), existing the third critical capillary, Ca_c^b. The phase diagram is plotted in Figure 7.1. Capillary number Ca and inverse of FvK number (defined in Equation 5.3) are essential parameters to determine the capsules states in flow.

In Figure 7.1, it is found that critical wrinkling capillary number Ca_c^w = 0.008-0.015, while the second and third capillary number, Ca_c^d, Ca_c^b, are correlated to the membrane

properties. In Equation 5.3, the inverse of FvK number is defined as the bending number $\kappa = B/G_s R^2$, related to the ratio between the bending and stretching resistance of the membrane. It seems that high bending number κ can inhibit the membrane wrinkles disappearing and rupture. In contrast, for the low bending number, $\kappa < 10^{-8}$, the membrane has high extensibility; the membrane can be stretched largely without out-of-plane deformation. In this case, we think the interfacial tension (≈ 0.022 N/m) is not negligible [173]. Unfortunately, it is difficult to measure the contribution of interfacial tension to the elasticity on capsules in experiment. In summary, apart from the capillary number, we might conclude that the membrane having enough elastic contribution is necessary to show wrinkling instability.

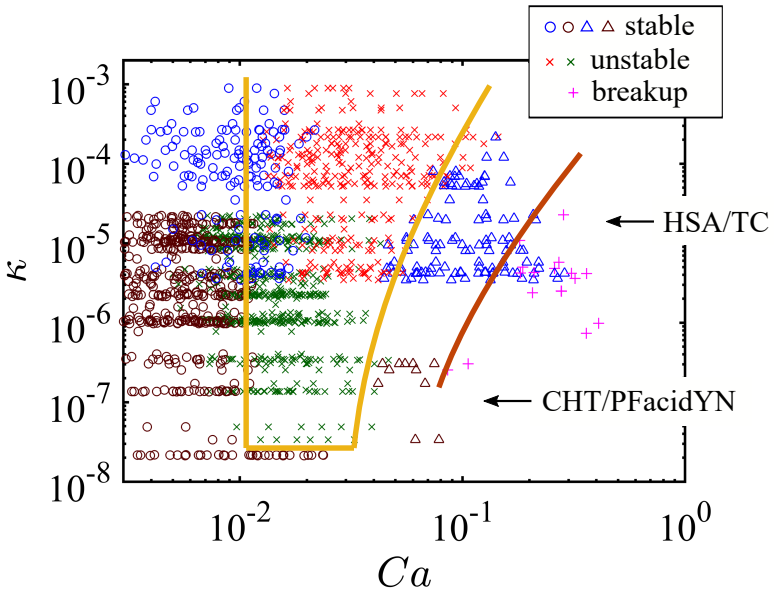

Figure 7.1: General phase diagram. For breakup, we do not plot many points here using the data in Chapter 4, because we don't know the membrane thickness of capsules in Chapter 4. Solid lines are eye guide.

In the process of microcapsules fabrication, stability, morphology, and rheology of capsule membrane have been paid much attention. First issue that we encountered is the stability of capsules during emulsification. Mass transfer process happens, due to existing of amphiphilic surfactant in the outside bulk fluid (W/O emulsion). Consequently, volume reduction of capsules induces the membrane collapse. This will become worse if the oil phase has large solubility of water. To avoid that, chemical potential balance and high membrane resistance for mass diffusion have to be required. However, from the other side of view, if the mass transfer proceeds from oil bulk phase to capsule phase, swelling of membrane happens. This leads to additional pre-stress

initially on the membrane. In all of our experiments, we have carefully controlled the capsules stability.

Membrane rheological properties have been discussed. Linear theory of small deformation allows us to estimate the surface shear elastic modulus. By tuning the complexation process, i.e. polycondensation time and concentrations of involved substances, we are able to modify the membrane properties in a large range, from 0.02 N/m to 5 N/m of G_s value, and from 40 nm to a few micrometers of thickness. In the large deformation, we have observed plasticity existing for membrane with low value of G_s, verified both for CHT/PFacidYN and HSA/TC capsules. The relaxation of such membrane depends on the rheological properties as well as the viscosity ratio. Large deformation (prior to breakup) results in permanent residual deformation, where the capsules can not return back to initial spherical shape. Capsule morphology has been controlled to prevent inhomogeneity and hairy impurities, especially for albumin capsules, by cross-linking the amino groups in short time.

Breakup of capsules then has been investigated in the planar extensional flow. The critical breakup capillary number Ca_c is found little dependence on the viscosity ratio when the shear modulus is below 0.1 N/m. High viscosity ratio decreases Ca_c slightly. In general, critical capillary number of capsules are slightly lower than that droplets who have the same inner phase as capsules. The shear elastic modulus G_s has no apparent influence on the Ca_c when the G_s < 0.1 N/m, but it appears to result in large Ca_c if the G_s > 0.2 N/m. For capsules with low shear modulus, bulbous and cylindrical breakup are observed, which are mainly dependent on the initial applied capillary number and viscosity ratio. More viscous capsule phase and high initial capillary number make it more susceptible to be stretched into a large aspect ratio (cylindrical breakup). In contrast, a capsule is most likely to form a narrow waist, consequently broken in bulbous-like shape, if the flow capillary number is close to the critical value. However, capsules with large shear resistance (G_s > 0.3 N/m) are expected to only show CY breakup.

Wrinkling and folding of capsules in the extensional flow finally have been explored, focusing on the Near-Threshold and Far-from-Threshold regimes. Wrinkles occurrence, indeed, is the competition result of the stretching energy and bending energy in membrane. To demonstrate wrinkling features in these two regimes, we have used two different wall materials of capsules, polymer-based (CHT/PFacidYN) and protein-based (HSA/TC). When deformed in the flow, both of these capsules begin to show well-defined wavelength once the flow strength applied is in larger than the threshold. The critical wrinkling stress is scaled as $\sigma_c \sim h/R$. Wavelength in the Near-Threshold regime has been checked by a scaling law $\lambda_w/R \sim [B/(G_s R^2)]^{1/4}$ (Figure 7.2).

Ca number does affect the wavelength in NT regime. However, in the FT regime, the wavelength shows non-uniform; at the cross section, wrinkles near the poles are observed decreasing and eventually disappearing, while the wrinkles at the mid-section are found almost constant before disappearing.

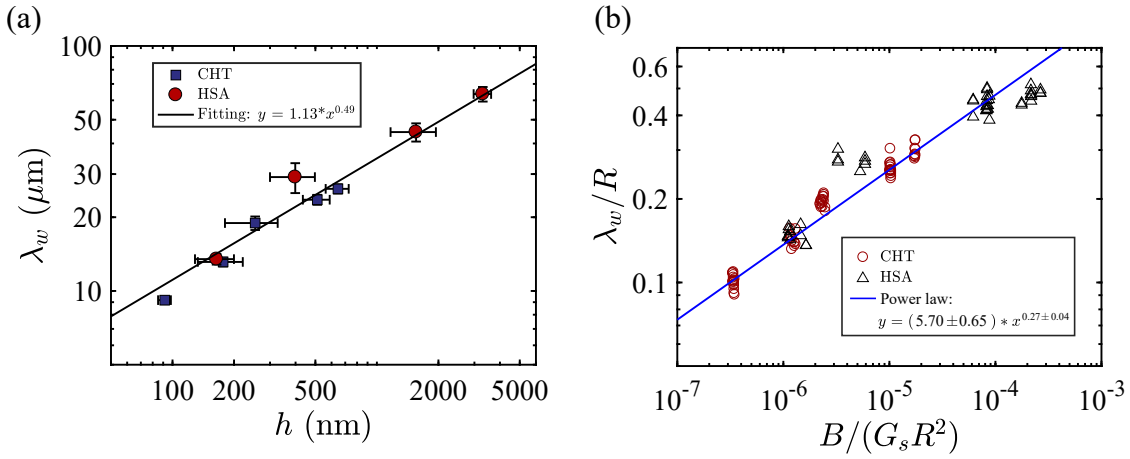

Figure 7.2: Wavelength of wrinkles in the NT regime for two kinds of capsules. (a) Mean wavelength as a function of membrane thickness. The radius of capsules is 92-110 μm. (b) Scaled wavelength as a function of κ number.

7.2 Perspectives

Our work opens numerous perspectives about microcapsules for the future studies. In this section, we will propose some potential ideas that may be carried out in the future work. Since we have developed a recipe for producing monodisperse microcapsules with tunable properties, it will allow us to study some other physical phenomena from the experimental point of view.

7.2.1 Interfacial rheology

We have estimated the membrane shear elastic modulus by using the asymptotic theory of small deformation in the extension flow. However, the membrane, indeed, involves two-dimensional dissipation (dilation and shear surface viscosity), specifically for the weak degree of chemical polycondensation. This is known as viscoelasticity. In this thesis, we can not estimate the order of magnitude of viscosity in membrane. To describe the contribution of elasticity and viscosity, a dimensionless parameter, $\chi = \eta_m \dot{\gamma}/E_s$, is defined in a shear flow. Barthès-Biesel [62] developed a model that capsule with viscoelastic membrane is expected to undergo inclination oscillation in the

shear flow, $\theta \sim f(\chi)$ (see Equation 1.13). Therefore, based on that, when we know orientation and membrane modulus, we might obtain the order of magnitude of viscosity of the membrane. In small deformation, the Taylor deformation is a function of χ, $D \sim Caf(\chi)$. By fitting the experimental date, de Loubens *et al*. [51] deduced the surface shear viscosity of HSA capsules is 1.3-2.5 N·s·m^{-1}, depending on the size of capsules. To confirm these models, a double wall-ring geometry of rheometer [179] can be used to provide a reference measurement, but for flat W/O interface.

7.2.2 Relaxation of elastic capsules

Relaxation happens after a capsule is stretched into large deformation and the flow is stopped. There might exist different steps of relaxation. For example, at beginning, the retraction of shape undergoes very fast ($\sim$ milliseconds), followed by the rate reduction. The relaxation of an elongated droplet has been reported by Stone *et al*. [14]. While, they focused on the capillary-induced end-pinching breakup during the shape retraction. In contrast, we speculate that end-pinching breakup can not happen on capsules because the elasticity prevent the fluid-like motion of membrane. Since we missed the fast retraction step of capsule shape in this thesis, it would be interesting to understand whether there exists a universal scaling for this relation process. Membrane properties and viscosity ratio could be the variables.

7.2.3 Wrinkles-to-folds transition

In this thesis, we just reported the threshold of wrinkles-to-folds transition in steady-state deformation of capsules. Indeed, the transition is time dependent (Figure 7.3). When exposed to a certain extension rate, the deformation of the capsule first reaches the steady-state deformation, but the wrinkles still develop. Folds, thereafter, might form and evolve. Based on that, there are several questions raised. For example, what will happen if the time is long enough? Does the pattern formation of wrinkles evolve by secondary bifurcations? Do the folds transfer into another bifurcation? According to the work of flat elastic membrane on soft substrate [91], there exist several bifurcations for folds. Unfortunately, it has little understanding about these transitions on initially spherical microcapsules.

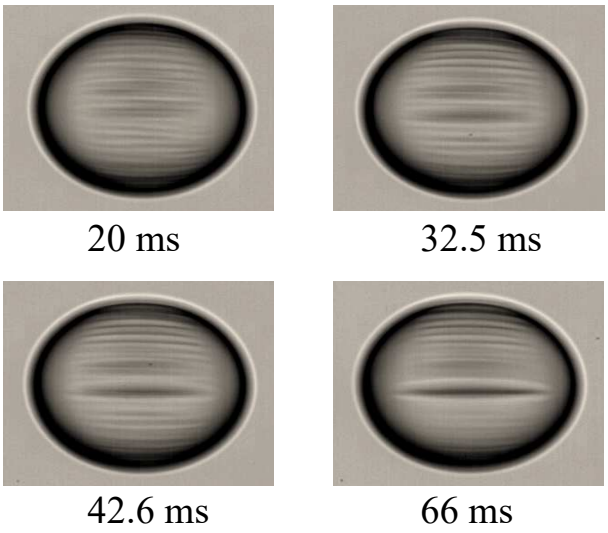

Figure 7.3: Time-dependent transition of from wrinkles to folds on CHT/PFacidYN microcapsules. Numbers indicate the time of taking the snapshot.

Appendix A

Protocol of solutions preparation

A.1 Chitosan solution (CHT)

Chitosan obtained by alkaline or enzymatic deacetylation of chitin, naturally has a pKa value of 6.5 of amino group in solution that pH value below 6.5. In our experiment, chitosan powder was dissolved in deionized water at a high concentration (e.g., 1.0% w/v or 2.0% w/v, referred to as 'Mother Solution') in acid condition. Stirring kept 12-14 hours on a magnetic platform to dissolve all the chitosan flakes at a room temperature of 22 $\pm$ 2 °C. Thereafter, this 'Mother Solution' was filtered with a sheet of 4-layer of 20 μm gauze to remove impurities. Before using, it relaxed 3-4 hours at 4-8 °C. To obtain desired concentration of chitosan, we thus diluted the 'Mother Solution' with water and glycerol. Again, to minimize impurities in solution we used Minisart syringe filters (pore size 5.0 μm) to filter the diluted solution.

Table A.1: Viscosity of different concentrations of chitosan solution mixed with glycerol

Conc. of chitosan (w/v)	**Perc. of glycerol (v/v)**	**Viscosity (mPas)***
0.05%	31.3%	13.87
0.11%	30.0%	28.27
0.25%	28.8%	53.48
0.50%	28.0%	138.56
0.80%	27.5%	300.41
1.20%	25.8%	794.07

* The data were measured within a range of shear rate 1-50 s^{-1} by a rheometer (Mars III). The chitosan solution is prepared in deionized water.

To avoid sedimentation or buoyancy when capsules are subjected in suspending fluids, we thus added glycerol in chitosan diluted solution to balance the density. Finally, the solution was adjusted at pH = 3.00 $\pm$ 0.02 by using hydrochloric acid (1

mol/L, from Sigma) and sodium hydroxide (1 mol/L, from Sigma). We stored chitosan solutions at 4-8 °C, and we re-checked the pH value with a pH meter (HANNA HI 8424) before using.

Different concentration of diluted chitosan solution mixed with glycerol is listed in Table A.1. The viscosity increases a factor of 60 times when we increase concentration of chitosan from 0.05% to 1.20% w/v.

A.2 Phosphatidic fatty acids solution (PFacidYN)

The groups R1 and R2 in the structure of PFacidYN represent fatty acid moiety bonded with fatty acid and hydrogen atoms, which makes it very poorly soluble in water, but well soluble in vegetable oils, for example rapeseed oil and sunflower oil. We thus dissolved PFacidYN in rapeseed oil at different concentrations. Practically, we prepared the PFacidYN solution at a fixed environment temperature (35 $\pm$ 1°C set in an oven) under mechanical stirring for 2-3 hours. In mass, the PFacidYN has around 55% w/w of phosphatidic acids, 40% w/w of neutral triglycerides and 5% w/w of ammonium salts (more detailed in references [28, 180]). Note that the fraction of ingredients might change a little for different batches of PFacidYN. Undissolved impurities were removed by centrifugation at 3000 rpm for 15 minutes (Centrifuge, Biofuge®Stratos).

Table A.2: Viscosity of different concentrations of PFacidYN solution.

Conc. of PFacidYN (w/w)	Viscosity (mPas)*
0.066%	65.04
0.15%	64.88
0.36%	66.44
0.66%	67.25
1.32%	68.63
2.75%	71.42

* The data were measured at a shear rate 100 s^{-1} by a rheometer.

A.3 Human serum albumin solution (HSA)

Like preparation of chitosan solution, we dissolved HSA powder in phosphate buffered saline at a high concentration ('Mother Solution', i.e., 20% w/w) under gentle stirring. Since the amino groups (-NH_2) in HSA structure are sensitive to ions strength and pH value of PBS, and plays important roles for membrane cross-linking, we thus carefully

pay attention to preparation of PBS. To obtain two different ions strengths with same pH value, we dissolved one tablet of PBS in 200 mL deionized water (PBS solution I), and one tablet of PBS in 100 mL deionized water (PBS solution II). Both of them have a pH $\approx$ 7.2 at temperature of 22 $\pm$ 2 °C. Similarly, we used deionized water and glycerol to dilute the Mother Solution for desired concentration and density of HSA solution. The final pH of diluted solution were adjusted at around 7.2 again, and used in all of our experiments. Afterwards, HSA solution was stored at temperature of 4-8 °C. Viscosity of various concentration of HSA solution is listed in Table A.3.

Table A.3: Viscosity of different concentrations of HSA solution mixed with glycerol.

Conc. of HSA (w/v)	**Perc. of glycerol (v/v)**	**Viscosity (mPas)***
1.0%	35%	3.0
3.0%	31%	3.1
6.0%	28%	3.5
12%	27%	3.7

* The data were measured within a range of shear rate 100 s^{-1} by using capillary (Lovis device).

A.4 Terephthaloyl chloride solution (TC)

Terephthaloyl chloride was dissolved in a mixture of chloroform : cyclohexane: mineral oil at a ratio of 1:1:4 by volume for stirring 10-12 hours. Here, we used mineral oil in the organic phase to reduce the possibility of capsules adhering on the reservoir wall during the cross-linking step, as well as to increase the viscosity of organic phase. As TC solution is turbid liquid, each time before using, we need to stir it for tens of minutes.

A.5 Suspending fluids

Silicone oil DC200, AP1000 and AR1000 were chosen as suspending fluids to load microcapsules for different purposes in our experiment. Their main physical and chemical properties are listed in Table A.4. To minimize the light fraction on capsules visualization, we used silicone oil with low refractive index (DC200) and added more glycerol inside capsules. However, the density between capsules and DC200 cannot be balanced because of low density of silicone oil in that case. One another side, to balance the density, we used AP1000 and AR1000 but with unmatched refractive indexes.

We chose AP1000 and AR1000 to quantitatively characterize capsules behaviours in extensional flow, for instance wrinkling and folding, but used DC200 to qualitatively investigate capsules.

Table A.4: Chemical structures and physical properties of silicone oils.

Chemicals	**Molecular structure**	**Density (g/cm^3)**	**Viscosity (mPas)**	**Refractive index**	**Surface tension**
DC200	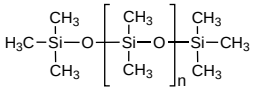	0.97	1000	1.40	19.5
AP1000	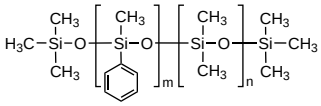	1.09	1000	1.51	22.7
AR1000	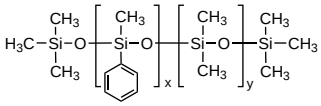	1.07	1000	1.46	22.4

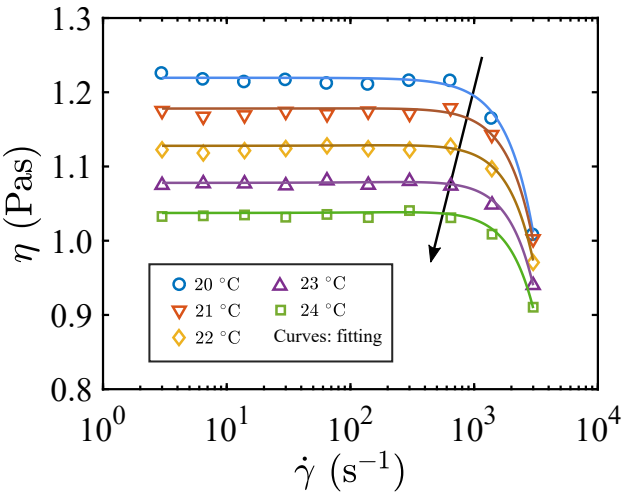

Figure A.1: Viscosity of silicone oil AP1000 as a function of shear rates at different temperature. Curves are the polynomial fitting results calculated with Equation A.1.

In the range of shear rate $\dot{\gamma} < 1000\ 1/s$, silicone oil shows constant viscosity at a given temperature, while it starts to descend for higher shear rates. The viscosity is also temperature dependence (Figure A.1). In our experiment, we use the Equation A.1 to calculate the viscosity.

$$\eta = -0.0459 * T + 2.15 \tag{A.1}$$

Indeed, AP1000 has same monomers as AR1000. Equation A.1 is also good for AR1000.

A.6 Physico-chemical properties of the chemicals

All the chemicals and their phyisco-chemical properties are shown in Table A.5. Density, viscosity and refractive index of chemicals were measured by Anton Paar DMA 4500, rheometer Mars III and Anton Paar refractometer, respectively. For some types of powder or flakes, data is not available.

Table A.5: Chemicals and basic properties.*

Chemicals	**Density (g/cm^3)**	**Viscosity (mPas)**	**Refractive index**
Glycerol	1.26	1000	1.46
Chitosan	~ 1.0	–	–
PFacidYN	0.92	230	1.42
Rapeseed oil	0.94	60	1.40
PBS solution	0.99	1	1.33
Human serum albumin	~ 1.0	–	–
Terephthaloyl chloride	0.92	–	–
Cyclohexane	0.94	0.93	1.40
Chloroform	1.48	0.55	1.46
Span85	0.94	300	1.48
Mineral oil	0.84	100	1.47
Medium chain triglyceride (MCT)	0.94	53	1.42
Sucrose acetate isobutyrate (SAIB)	1.15	–	1.45

* The measurements were carried out at 22 °C. The hyphen '-' means no data available.

Note that SAIB should be placed in a temperature above 90°C to become liquid, and mixed quickly with MCT oil or rapeseed oil.

A.7 Treatment of silicone oil

To avoid buckling and control pre-stress of capsules in suspending fluid, we treat silicone oil (viscous, $\eta \sim 1000$ mPas) using the same procedures as following:

(1) Add 15 μL distilled water in 40 mL silicone oil in a glass bottle and seal it with parafilm;

(2) Stir the oil for at least one week on a magnetic platform;

(3) Before using, centrifuge a quantity of oil at 1200 rpm for 10 minutes (Biofuge®Stratos).

(4) To avoid evaporation, we always keep silicone oil (treated) in a closed reservoir.

Appendix B

Microfluidics system

B.1 Configuration of T-junction chip

A T-junction 3D microfluidic chip was fabricated by a 3D printer (Formlabs Inc, Form 1+) with hydrophobic resin (clear, FLGPCL03, Formlabs). The detailed dimension is shown in Figure B.1.

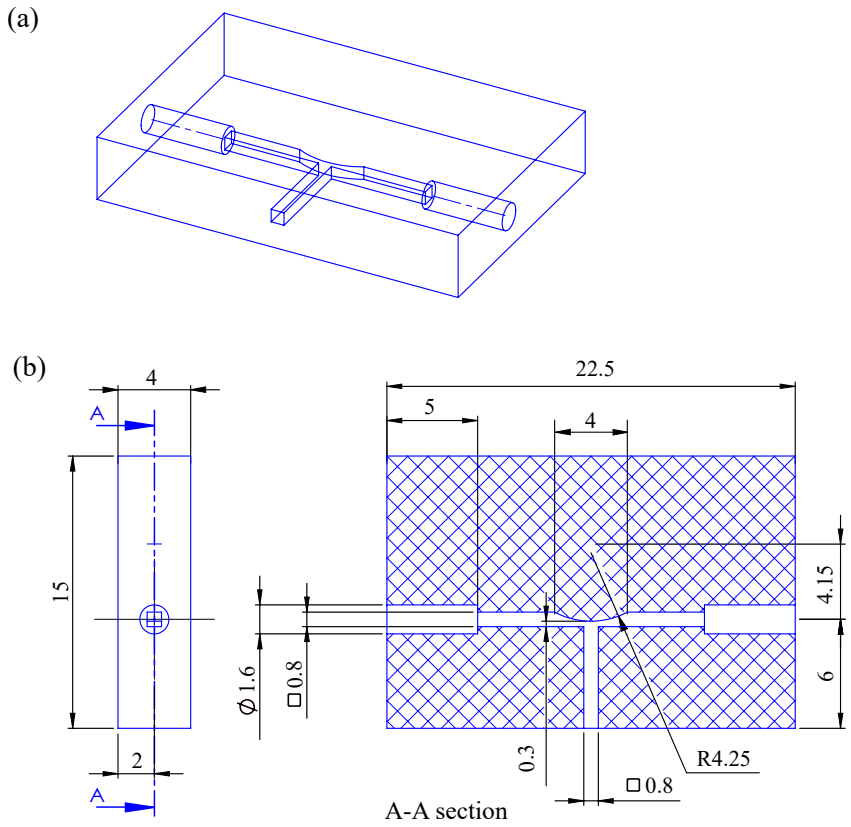

Figure B.1: Configuration of T-junction microfluidic chip. (a) 3D configuration. (b) Detailed dimension on 2D.

The branch perpendicular to the main channel is used for inserting a capillary. The two ends of the main channel are connected to Fluigent system via plastic tubes (see

details in next section). Tubes and capillary are stuck on the chip with UV glue (NOA 61) cured when exposed to ultraviolet light.

B.2 Flow rate controlled system

Two immiscible phases were driven by a pressure controlled pump to enter the microfluidic chip (schematic system shown in Figure B.2). The system consists of a pressure pump MFCS-EZ (0-1000 mbar), two flow rate controllers (model L and M), and the T-junction chip. The size of microcapsules generated in the chip is controlled by adjusting the flow rates of aqueous and oil phases. Typically, for producing diameter of 200 μm microcapsules, the flow rates of oil and aqueous phases are 240 μL/min and 5 μL/min, respectively. To prevent occurrence of aqueous phase stuck on the inner wall of the chip, we first introduce continuous phase (oil phase) into the chip, followed by bringing the disperse phase. Any bubbles or pollutants should be avoided in this process.

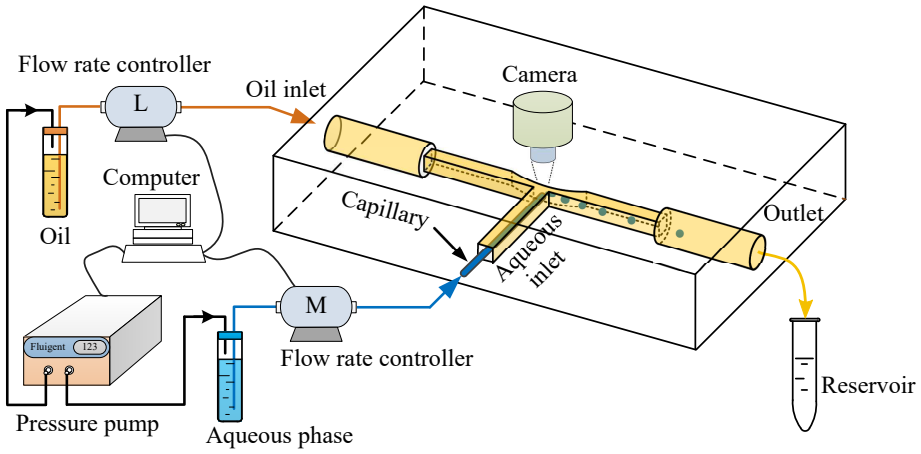

Figure B.2: One-step microcapsules fabrication with controlled size in microfluidic system.

Appendix C

Models of flow chambers

C.1 Design of the flow chamber

The extension flow chambers used in our experiment are shown in Figure C.1. Indeed, practically it is difficulty to observe the capsules deformation and wrinkling development at the same time in both views. We, thus, separated the observation with two flow chambers. For detecting the global deformation and wrinkles length in x-y plane, we used the flow chamber I (Figure C.1(a)). While for observing wrinkles profiles in y-z plane, we used the chamber II (Figure C.1(b) and (c)).

Comparing Figure C.1(b) and (c), we find that decreasing the thickness of suspending silicone oil that light pass through improves the capsule photography a lot, narrowing light refraction at the surface of capsule. However, thickness of the flow chamber, 4 mm, is the minimum we can fabricated on PMMA or PVC plates.

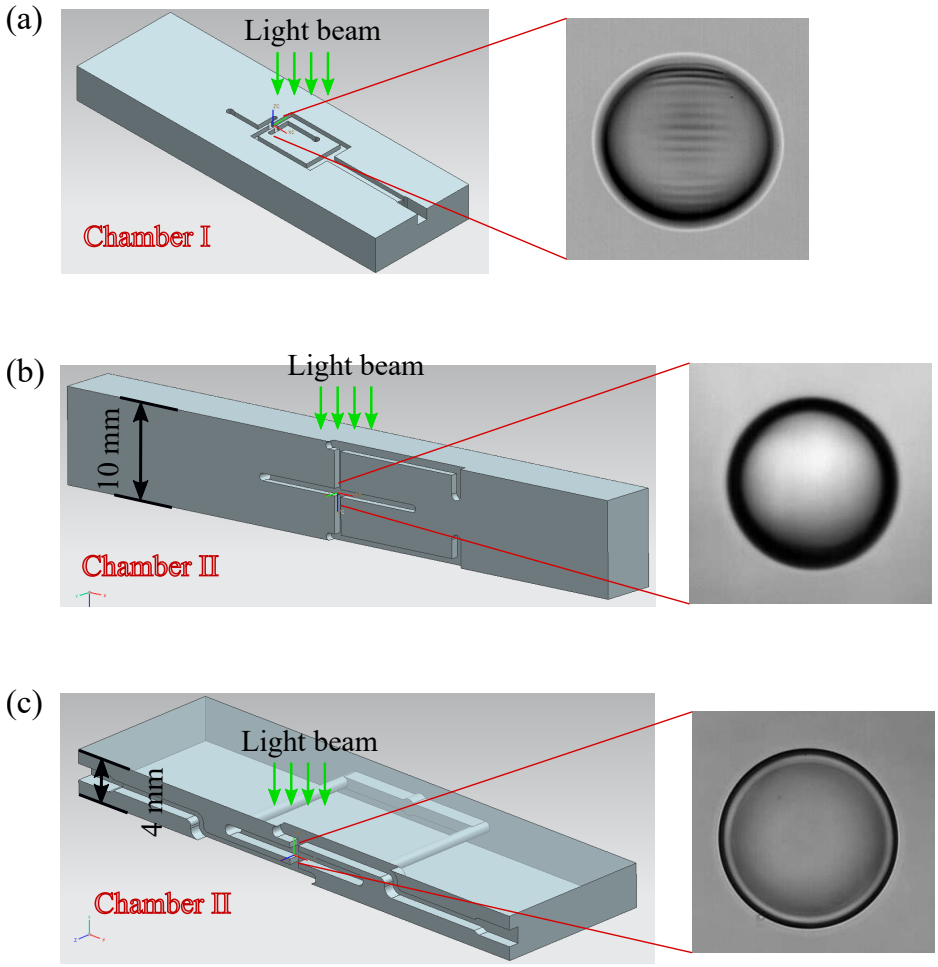

Figure C.1: 3D model of cross-slot flow chambers for stretching microcapsules. (a) Chamber I, used for observing capsules deformation in x-y view. (b) and (c) Chamber II, used for observing capsules profile in y-z view. Capsules were enclosed 0.25% w/v chitosan solution with 27% v/v glycerol (RI $\approx$ 1.37).

Appendix D

Dry membrane preparation

D.1 Drying process

A flat membrane was prepared by covering 4 ml aqueous phase with 6 ml oil phase for a few days. When it becomes sufficiently stiff, we adhered the membrane on a glass substrate or aluminium sheet using tweezers. To remove residual oil, we then used plenty of cyclohexane, ethanol and water to rinse the membrane. After that, the sample was placed in an oven set temperature 40-60°C for dry. A precision balance was used to measure the weight change (see Figure D.1). By assuming that thickness decreasing is mainly due to mass loss, we thus have

$$\psi = \frac{m_{wet}}{m_{dry}} = \frac{\rho_{wet} A_{wet} h_{wet}}{\rho_{dry} A_{dry} h_{dry}} \approx \frac{h_{wet}}{h_{dry}}, \tag{D.1}$$

where density $\rho_{wet} \approx \rho_{dry}$, and surface area $A_{wet} \approx A_{dry}$ for wet and dry membrane. We found that the coefficient ψ is 1.2-1.4 for CHT/PFacidYN and HSA/TC membrane.

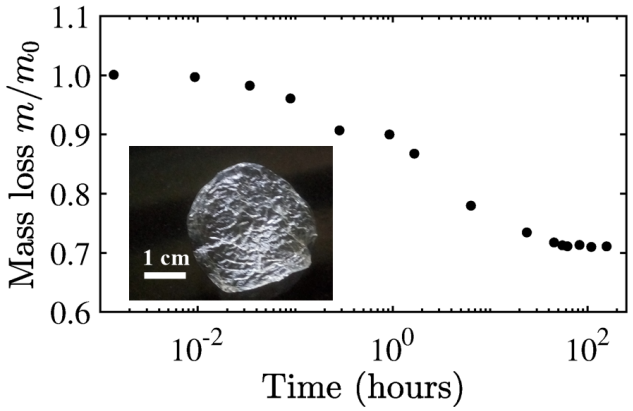

Figure D.1: Mass loss of a membrane during dry. Insert: image of the sample on a black background.

D.2 Membrane tailoring for SEM

D.2.1 Flat membrane

We cut the flat dry membrane deposited on aluminium sheet along a straight line with a thin blade. After that, the sample was mounted on the sample holders with double-side adhesive tape. A very thin carbon layer was used between the sample and the holders. One example, HSA/TC membrane cross section is shown in Figure D.2.

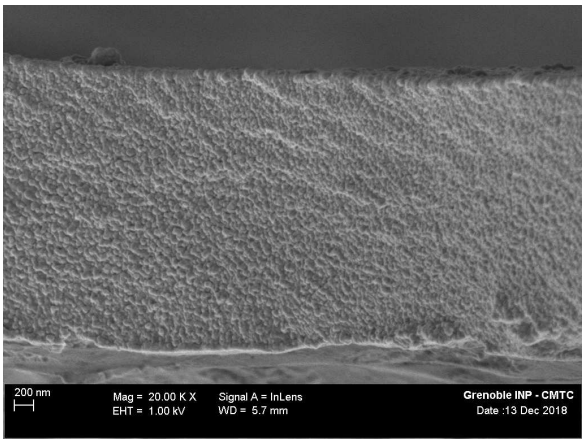

Figure D.2: SEM image of HSA/TC membrane at the cross section.

D.2.2 Capsule membrane

Similar to the drying process of CHT/PFacidYN capsules, HSA/TC capsules were deposited on the conducting glass, and then were dried in an oven under 40-60 °C. After drying, there exist many cracks on the membrane where it allows us to measure directly the thickness (Figure D.3(a)). In some cases, for example capsules having thick membrane, there is no cracks appearing on the surface. Thus, to see the cross section of membrane, we used a sharp blade to crush the capsules, forming broken pieces shown in Figure D.3(b).

In order to increase the conductivity of samples, we spray a thin layer of carbon powder (thickness < 10 nm) on the samples surface. This thickness of carbon layer can be neglected compared to the thickness of membrane. In practice, to minimize the measurement error due to the inclination of sample, we rotate the sample's cross section as perpendicular as possible to the observation direction.

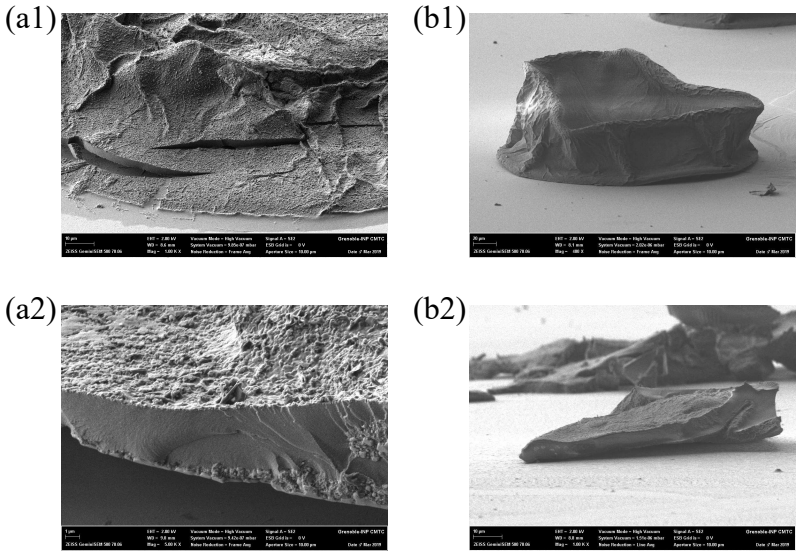

Figure D.3: Two examples of HSA/TC capsules with different thickness under SEM. (a1) A thin membrane collapses on a conducting glass. (a2) Magnified image of a crack area in (a1), in which we can measure the thickness. (b1) A thick membrane capsule dried on a conducting glass. (b2) Broken pieces of membrane of capsule in (b1).

Appendix E

Capsules breakup preparation

E.1 Viscosity ratio adjustment

Droplet and capsule fluids are the mixture of chitosan solution, glycerol, sucrose and PEG. Suspending fluids are the silicone oils with different viscosity. Different from the chitosan solution preparation in Appendix A, here we dissolve chitosan powder in phosphate buffer saline (PBS) solution at pH $\approx$ 3.0 with high concentration (1.0% w/v, referred to as 'Mother Solution'). PBS is used to slow down the capsule membrane polycondensation because of existing of ions. To ensure the same concentration of ions, we use the PBS solution II (see Section A.3 in Appendix A) to prepare the capsule fluids. PEG flakes (Mn = 35,000 from Sigma) is used to increase the viscosity of liquid inside capsules. All the aqueous phases are adjusted at pH = 3.0 when we produce capsules. To obtain various shear elastic moduli of capsules, like discussed in Chapter 3, we keep chitosan droplets in the rapeseed oil with presence of different concentration of PFacidYN for diverse reaction time.

Basic properties of liquids are listed in the Table E.1. In the table, CHT represents chitosan solution, and SU is the granular sucrose, and GL is the pure glycerol (> 99%). AP and DC are silicone oils. Note that, we just show the values at the temperature of 22 °C in the table. Indeed, in our experiment, the temperature might change around 1 °C around 22 °C. We considered the temperature correction in the data analysis, similar to Section A.5. Density difference between capsules/droplets and suspending fluid is too small, thus neglected. Several different viscosity ratios are used, namely λ_η = 3.4×10^{-3}, 6.5×10^{-3}, 1.3×10^{-2}, 2.6×10^{-2}, 7.1×10^{-2} and 1.7. In the range of shear rate we investigated in our experiment, both capsule/droplet and suspending fluids are considered as quasi-Newtonian or Newtonian fluid.

Table E.1: Physical properties of liquids used in breakup experiment. Data measurements are carried out at temperature 22 °C.

Fluid type	**Viscosity (mPa·s)**	**Density (g/ml)**	**Surface tension⋆ (mN/m)**
0.25%CHT+20%SU	7.1*	1.08	32
0.4%CHT	10 *	1.01	32
0.3%CHT+21.2%GL	13.2 *	1.06	32
0.3%CHT+22.5%GL	13.5 *	1.07	32
0.3%CHT+25%GL	14.6 *	1.08	32
0.3%CHT+12.8%GL+20%PEG	331.7 ×	1.07	31
AP100	202.4 ×	1.06	22
50%AP100+50%AP1000	517.1 ×	1.07	22
AP1000	1140.4 ×	1.09	22
50%DC200(0.1)+50%DC200(30)	2923.3 ×	0.98	23

* The data are the average measured using Anton-Paar Lovis module. The measuring shear rate is within 100 s^{-1}.

× The date are obtained from Mars Rheometer equipped with cone-plat geometry C60 1° TiL, in a range of shear rate 3-300 s^{-1}.

⋆ Liquid-air surface tension is measured by the pendent drop method with critical volume.

E.2 Particles decoration at water-oil interface

Hydrophilic PMMA particles and hydrophobic PS particles without surface charge are used to decorate the interfaces of droplets and capsules. Particles can be absorbed at the water/oil interface by the advantage of wettability. The procedures of operation are described as following.

PMMA particles

PMMA particles (Diameter ≈ 8-10 μm) are added into PFacidYN solution at a concentration around 0.5 mg/mL. To disperse particles, the particle-laden solution is then stirred using an agitator for a few hours. Since the density of PMMA particles is around 1.2 g/cm^3 which is larger than the oil phase (0.95 g/ml), stirring is necessary each time before preparing capsules. When chitosan phase is dispersed in the oil, PMMA particles will move towards the droplet interface due to its hydrophilic nature. At the same time, complexation between chitosan and PFacidYN molecules takes place, embedding the particles in the growing membrane. As the particles size is much larger than the thickness of membrane in our experiment, only partial area of each particle is buried by the membrane. For droplets decoration, PMMA particles are directly dispersed in the suspending fluids. When added aqueous phase in the suspending fluids, particles are attached on the droplets surface by the hydrophilicity.

PS particles

Differently, PS particles are naturally hydrophobic. They tend to move towards the W/O interface when dispersed in the chitosan solution. Concerning droplets/capsules are small, we use lower concentration of particles in the aqueous phase to weaken their effect on breakup (0.1 mg/mL). In practice, it takes time for PS particles aggregating at the interface from droplet bulk phase. Before the complexation occurrence at the interface, we keep the aqueous droplets in the oil phase with low concentration of PFacidYN ($\approx$ 0.1% w/w) for 20 minutes, followed by transferring these droplets into a higher concentration of PFacidYN to thicken the membrane forming capsules. Similarly, for droplets decoration PS particles are only dispersed in the aqueous phase. When the particle-laden aqueous phase is emulsified in the suspending fluids, particles move towards to the hydrophobic side of the W/O interface.

E.3 Capsules and droplets preparation

As the results in Chapter 3 show that the surface shear elastic modulus G_s is independent on the capsules size for given membrane complexation formulation, we here fabricate capsules using simple static agitation in a beaker.

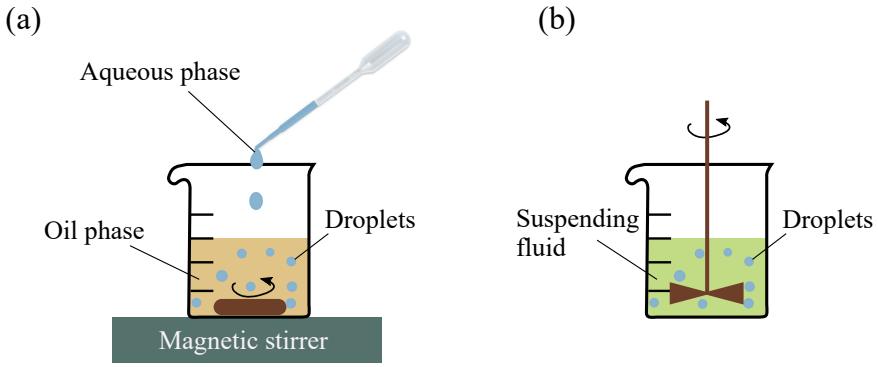

Figure E.1: Preparation of polydisperse droplets and capsules. (a) W/O droplets templates producing prior to membrane complexation. If with presence of PMMA particles (PS particles) in the oil phase (aqueous phase), the stirring should last at least 20 minutes. (b) Direct emulsification of droplet phase in the suspending fluid.

Figure E.1(a) shows the droplet templates preparation prior to assembling the membrane subject into a higher concentration of PFacidYN oil solution. 100 μL aqueous solution is emulsified in 12 mL rapeseed oil containing 0.1% w/w PFacidYN. Droplets size can be adjusted by the stirring speed. After, similar to the description in Chapter 2, these templates are transfer into a desired concentration of PFacidYN solution for

membrane formation. To stop the membrane complexation, we use the rinsing liquid to wash capsules, followed by dispersion in the suspending fluid.

Figure E.1(b) shows the preparation of droplets in the suspending fluid. Simply, around 50 μL aqueous phase is emulsified directly in 15 mL suspending fluid using a blender. Bubbles are removed using a vacuum pump several times.

E.4 Fluorescent capsules preparation

To dye the membrane of capsule, we use a commercial fluorescent dye (Hostasol Yellow 3G (HY-3G), from Clariant), which can be dissolved in organic phases. It is greenish yellow with good light fastness and excellent heat resistance. The wavelength of excitation is 450-480 nm, and emission is 520-550 nm.

Indeed, the CHT/PFacidYN capsule is naturally fluorescent due to the phosphate groups. But, the intensity is weak. To increase the emitted light intensity, we mix the HY-3G with pure cyclohexane. Followed by the description in section E.3, after removing the residual PFacidYN in the solution, we transfer capsules into cyclohexane with 0.1% w/v HY-3G for 20-30 minutes. During this process, the dye is adsorbed onto the surface. After that, pure cyclohexane is used to remove the excess dye. Figure E.2 shows the CHT/PFacidYN capsules with and without HY-3G treatment under blue light.

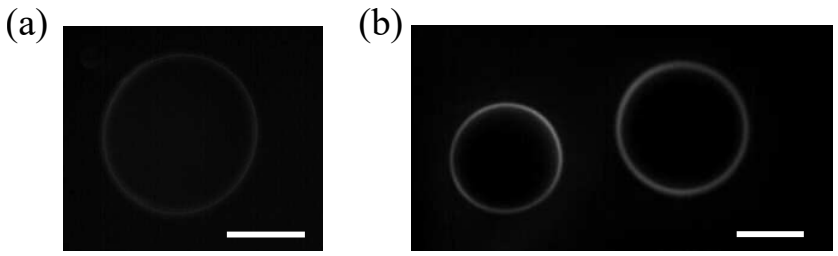

Figure E.2: Capsules on the substrate in fluorescent field. (a) CHT/PFacidYN capsules without HY-3G treatment. (b) CHT/PFacidYN capsules with HY-3G treatment. Scale bars: 85 μm.

E.5 Interfacial tension measurement

Since the droplets or capsules phase the same density with suspending fluid, classic pendent drop method does not work any more. Similarly, as deforming capsules, we stretch drops (no membrane) in the suspending fluid. In the limit of small deformation, theory of Taylor [72, 181] accurately describes the equilibrium deformation taking into

account of viscosity ratio and interfacial tension, as following

$$D = \frac{1}{8}\frac{16 + 19\lambda_\eta}{1 + \lambda_\eta}Ca \tag{E.1}$$

where Capillary number $Ca = \eta_{ex}\dot{\epsilon}R/\gamma$. γ indicates the liquid-liquid interfacial tension.

In Table E.2, we give an example of interfacial tension measurement result. The viscosity ratio is $\lambda_\eta = 7 \times 10^{-2}$. Different size of drops were studied. Size has no effect on the interfacial tension. Indeed, for all the droplet-suspending fluid systems in our experiment, the interfacial tension of droplets is similar, around 21 mN/m.

Table E.2: Interfacial tension of chitosan drops in silicone AP1000.

Radius, R (μm)	**Tension, γ (N/m)**
95.11	0.0219
71.21	0.0227
36.97	0.0236
69.83	0.0213
113.60	0.0212
218.66	0.0201
183.48	0.0216
78.58	0.0211

E.6 Interfacial rheology measurement

Interfacial rheology of the flat membrane is measured by using a bicone geometry (Bicone 68 mm, 2 x 5°) equipped on MCR 501 (Anton Paar). Figure E.3 shows the sketch of the interfacial rheology measurement.

To place the edge of bicone geometry exactly at the interface of the oil-water phase, we manipulate according to the following steps.

- Find zero position of the system, and set normal force zero.
- Rise up the geometry to a position where we can fill the cell easily.
- Fill the cell with the aqueous phase just a little below the required position (working line).
- Set down the geometry to the working position. If the down tip of geometry contacts the liquid surface, the normal force becomes negative.

- Fill the aqueous phase carefully with pipette until the normal force become zero again.
- Fill the oil phase with pipette carefully, better ejecting the liquid onto the top face of geometry to minimize the disturbance on the forming interface.

In the oscillation mode, by applying a pre-defined strain $\gamma(t) = \gamma_0 \cos(\omega t)$, the stress response $\tau(t) = \tau_0 \sin(\omega t + \delta)$, where ω is the frequency, and δ is the phase shift due to the hysteresis. The complex interfacial shear modulus $G_i^*(\omega)$ can be calculated as

$$G_i^*(\omega) = \frac{\tau_0 e^{i\delta}}{\gamma_0} = |G_i^*|(\cos\delta + i\sin\delta) = G_i^{'}(\omega) + iG_i^{''}(\omega) \tag{E.2}$$

where the $G_i^{'}$ and $G_i^{''}$ are described as interfacial storage modulus and loss modulus, respectively. In our experiment, to avoid the effect of inertia due to the geometry, we only work within the frequency lower than 5 Hz. In the strain-sweep test, the frequency is fixed at 0.5 Hz.

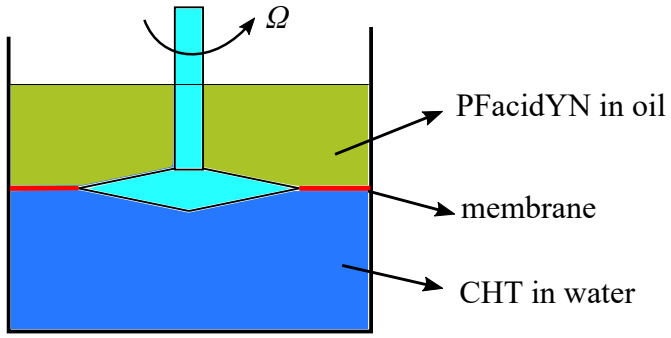

Figure E.3: Sketch of interfacial rheology measurement.

E.7 Fluorescent capsule G_s > 0.1 N/m during rupture

Figure E.4 shows the image sequences of a fluorescent capsule rupture process in the extensional flow. We can see that the membrane is broken randomly. Unlike the capsule with low G_s (< 0.1 N/m), the membrane is not stretched continuously during the breakup.

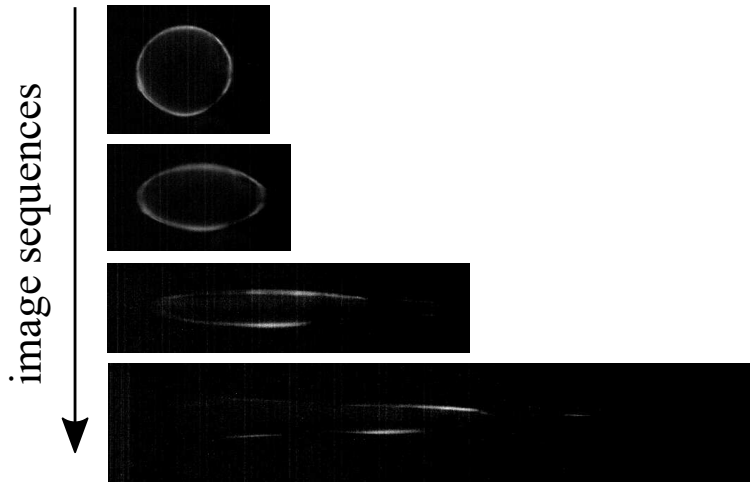

Figure E.4: Image sequences of fluorescent capsule rupture in flow. $G_s \approx$ 0.15 N/m.

Appendix F

Wrinkling instability of CHT/PFacidYN capsules

F.1 Estimation of wrinkles arc length

In the view of L-S (x-y plane), the direct measurement of wrinkles length is the projection length λ_w. To estimate the real length on the curved surface, we thus consider the geometry relation (as shown in Figure F.1).

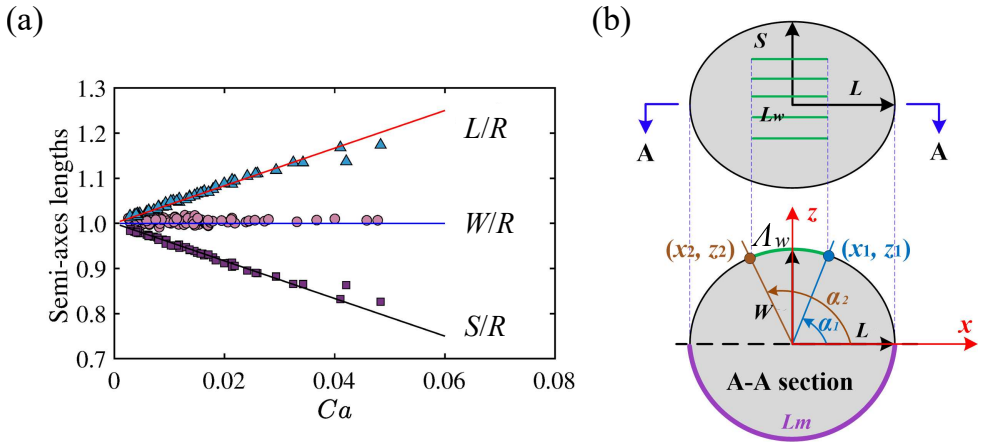

Figure F.1: Wrinkles arc lengths. (a) Three semi-major axes lengths L/R, S/R and W/R as a function of capillary number Ca. Scattering points are experimental data, obtained from different capsules. Solid lines are asymptotic results from Equation 2.6. (b) Schematic representation between wrinkles projection length, L_w, and arc length, Λ_w, in two views.

Here, we assume that the configuration of a deformed capsule is elliptical both on L-S and L-W views. For small deformation, W is considered as equal as to the initial radius R ($W \approx R$). This is verified by our experimental observation (Figure F.1(a)).

Therefore, the standard equation of the ellipse shape on L-W plane is given by

$$\frac{x^2}{L^2} + \frac{z^2}{W^2} = 1 \tag{F.1}$$

with the centre (0, 0), where L can be experimentally determined from the view of L-S. Combining the projection length L_w in the L-S view, we can deduce the two endpoints (x_1, z_1) and (x_2, z_2) of the corresponding arc length Λ_w in the view of L-W in Cartesian coordinates (Figure F.1(b)). Hence, we have

$$\tan\alpha_1 = \frac{z_1}{x_1} \quad \text{and} \quad \tan\alpha_2 = \frac{z_2}{x_2} \tag{F.2}$$

In the form of parametric expression of an ellipse, we have $x = L\cos t$ and $z = W\sin t$, where t is the eccentric anomaly. For the two intersection points, we have

$$\frac{z_1}{x_1} = \frac{W}{L}\tan t_1 \quad \text{and} \quad \frac{z_2}{x_2} = \frac{W}{L}\tan t_2 \tag{F.3}$$

Then, the arc length between t_1 and t_2 can be numerically calculated by replacing arc length with many small straight segments, $\sqrt{(\delta x)^2 + (\delta z)^2}$. Thus, the total arc length can be written

$$\Lambda_w = \sum_{i=1}^{N} \sqrt{(\delta x)^2 + (\delta z)^2} \tag{F.4}$$

where N is the number of divided segment between t_1 and t_2.

F.2 Estimation of wavelength λ_w

The wavelength of wrinkles was measured from the images obtained in W-S view by extracting the profiles of capsules boundary and by applying one dimensional Fast Fourier Transform (FFT). First, we detected the boundary and the centre coordinates of each capsule. Then the relative distance r-R, defined as the distance of each point on the boundary from the centres subtracting initial radius, can be plotted as a function of the angle β (Figure F.2(a) and (b)). In order to expel the influence of periodically overall deformation of the capsule, we adopted the Chebyshev type II method to filter the low frequency signal (Figure F.2(b) blue curve). Then, we split the entire signal into several segments (for example, the first one in Figure F.2(b) dashed box), in which the wavelengths λ_w are similar. FFT was then used to determine the main frequency for each segment, illustrated in Figure F.2(c). Finally, the average wavelength in each

image can be calculated as

$$\overline{\lambda}_w = \frac{1}{N}\sum_{i=1}^{N}\frac{R^i_{local}}{f^i_{peak}} \tag{F.5}$$

where N is the number of splitting segments. f^i_{peak} and R^i_{local} are the main frequency and the local radius of deformed capsules in each segment. Note that R^i_{local} is close to the value of radius R in the region of wrinkling Near-Threshold.

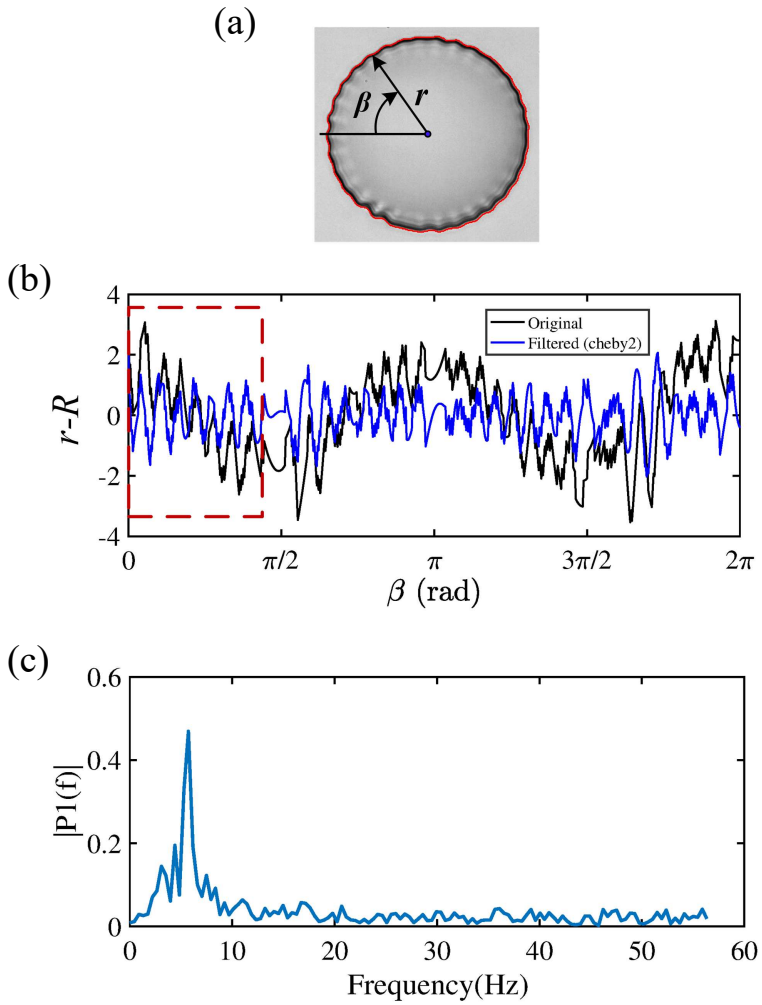

Figure F.2: Measurement of wrinkles wavelengths. (a) Detection of the boundary of a wrinkled capsule. (b) r-R as a function of angle β. Black curve is the original one, while the blue one is after filtering treatment with Chebyshev type II. (c) Spectrum of the blue signal in the dashed box in (b) as function of the frequency.

List of Symbols

h	thickness
R	radius
G_s	surface shear modulus
K_s	surface area dilation modulus
B	bending modulus
G	3D shear modulus
E	3D Young's modulus
E_s	2D Young's modulus
$\boldsymbol{T}$	tension tensor
T_1	principal tension
T_2	principal tension
C	concentration or tuning parameter
$\boldsymbol{q}$	load
$\boldsymbol{m}$	bending moment tensor
Re	Reynolds number
∇	gradient
$\dot{G}$	strain rate
D	Taylor parameter
p_{cr}	critical buckling pressure
t_r	reaction time
L, S and W	three principal axis lengths of a deformed capsule
Ca	capillary number
Ca_c^w	critical wrinkles capillary number
Ca_c^f	critical folds capillary number
Ca_c^d	critical capillary number where wrinkling disappearance
Bq	Boussinesq number
U_s	stretching energy
U_b	bending energy
U_m	constraints energy
A	amplitude

Q	flow rate
U	mean entrance velocity
D_h	hydraulic diameter
D_{sp}	distance from the stagnation point
D_{res}	residual deformation
P	perimeter
ν	3D Poisson ratio
ν_s	surface Poisson ratio
λ_1	extension ratio
λ_2	extension ratio
λ_w	wavelength
Ψ	coefficient varying between 0 and 1
χ	membrane viscosity to elasticity
η_m	membrane viscosity
η	fluid viscosity, with ex or in means external or internal fluid
γ	tensile strain or surface tension
$\dot{\gamma}$	shear rate
$\dot{\epsilon}$	extension rate
ε	strain
$\boldsymbol{\tau}$	tension tensor
σ	stress; with c in subscript means critical stress
λ_η	viscosity ratio
θ	angle
ξ	small deflection
$\mu^{'}$	elasticity
$\mu^{''}$	viscosity
κ	stiffness
ρ	density
τ_s	response time
τ_r	residence time
Λ_w	wrinkling arc length
L_w	wrinkling projected length

List of Abbreviations

RBCs	**R**ed **B**lood **C**ells
CHT	**C**hitosan
HSA	**H**uman **S**erum **A**lbumin
TC	**T**herephtaloyl **C**hloride
PFacidYN	**P**hosphatidic fatty acids
OTS	**O**octadecyltrichlorosilane
ALG	**A**lginate
H	**H**ooke's law
GH	**G**eneralized **H**ooke's law
NH	**N**eo-**H**ooke's law
MR	**M**ooney **R**ivlin law
SK	**Sk**alak law
TT	**T**ank-**T**reading
TU	**T**umbling
SW	**S**winging
WO	**W**ater in **O**il
OW	**O**il in **W**ater
BU	**B**ulbous
CY	**C**ylindrical
TS	**T**ip-**S**treaming
STS	**S**tretched **T**ip-**S**treaming
LbL	**L**ayer-by-**L**ayer
MCT	**M**edium **C**hain **T**riglyceride
RI	**R**efractive **I**ndex
SG	**S**tagnation **P**oint
AFM	**A**tomic **F**orce **M**icroscopy
SEM	**S**canning **E**lectron **M**icroscopy

List of Figures

List of Tables

Bibliography

[1] Imane Hadef, Barbara Roge, and Florence Edwards-Levy. Serum albumin-alginate microparticles prepared by transacylation: Relationship between physicochemical, structural and functional properties. *Biomacromolecules*, 16(8):2296–2307, 2015.

[2] Haishui Huang, Yin Yu, Yong Hu, Xiaoming He, O Berk Usta, and Martin L Yarmush. Generation and manipulation of hydrogel microcapsules by droplet-based microfluidics for mammalian cell culture. *Lab on a Chip*, 17(11):1913–1932, 2017.

[3] Keun-Shik Chang and William L Olbricht. Experimental studies of the deformation of a synthetic capsule in extensional flow. *Journal of Fluid Mechanics*, 250:587–608, 1993.

[4] V Seshadri, RM Hochmuth, PA Croce, and SP Sutera. Capillary blood flow: Iii. deformable model cells compared to erythrocytes in vitro. *Microvascular research*, 2(4):434–442, 1970.

[5] Dominique Barthes-Biesel. Motion and deformation of elastic capsules and vesicles in flow. *Annual Review of fluid mechanics*, 48:25–52, 2016.

[6] S Kessler, R Finken, and U Seifert. Swinging and tumbling of elastic capsules in shear flow. *Journal of Fluid Mechanics*, 605:207–226, 2008.

[7] Jules Dupire, Marius Socol, and Annie Viallat. Full dynamics of a red blood cell in shear flow. *Proceedings of the National Academy of Sciences*, 109(51):20808–20813, 2012.

[8] TM Fischer, CWM Haest, M Stöhr, D Kamp, and B Deuticke. Selective alteration of erythrocyte deformability by sh-reagents. evidence for an involvement of spectrin in membrane shear elasticity. *Biochimica et Biophysica Acta (BBA)-Biomembranes*, 510(2):270–282, 1978.

[9] Jonathan Gubspun. Experimental study of capsules into confined flows. *Ph.D. Thesis of Aix-Marseille Université*, 2015.

[10] Anja Walter, Heinz Rehage, and Herbert Leonhard. Shear induced deformation of microcapsules: shape oscillations and membrane folding. *Colloids and Surfaces A: Physicochemical and Engineering Aspects*, 183:123–132, 2001.

[11] Ivanka Koleva and Heinz Rehage. Deformation and orientation dynamics of polysiloxane microcapsules in linear shear flow. *Soft Matter*, 8(13):3681–3693, 2012.

[12] Reimar Finken and Udo Seifert. Wrinkling of microcapsules in shear flow. *Journal of Physics: Condensed Matter*, 18(15):L185, 2006.

[13] E Lac, D Barthes-Biesel, NA Pelekasis, and J Tsamopoulos. Spherical capsules in three-dimensional unbounded stokes flows: effect of the membrane constitutive law and onset of buckling. *Journal of Fluid Mechanics*, 516:303–334, 2004.

[14] Howard A Stone. Dynamics of drop deformation and breakup in viscous fluids. *Annual Review of Fluid Mechanics*, 26(1):65–102, 1994.

[15] BJ Bentley and L Gary Leal. An experimental investigation of drop deformation and breakup in steady, two-dimensional linear flows. *Journal of Fluid Mechanics*, 167:241–283, 1986.

[16] Keun-Shik Chang and William Lee Olbricht. Experimental studies of the deformation and breakup of a synthetic capsule in steady and unsteady simple shear flow. *Journal of Fluid Mechanics*, 250:609–633, 1993.

[17] Kyekyoon Kevin Kim and Daniel W Pack. Microspheres for drug delivery. In *BioMEMS and biomedical nanotechnology*, pages 19–50. Springer, 2006.

[18] A Viallat and M Abkarian. Red blood cell: from its mechanics to its motion in shear flow. *International journal of laboratory hematology*, 36(3):237–243, 2014.

[19] Gwennou Coupier, Alexander Farutin, Christophe Minetti, Thomas Podgorski, and Chaouqi Misbah. Shape diagram of vesicles in poiseuille flow. *Physical review letters*, 108(17):178106, 2012.

[20] R Skalak and PI Branemark. Deformation of red blood cells in capillaries. *Science*, 164(3880):717–719, 1969.

[21] Luca Lanotte, Johannes Mauer, Simon Mendez, Dmitry A Fedosov, Jean-Marc Fromental, Viviana Claveria, Franck Nicoud, Gerhard Gompper, and Manouk Abkarian. Red cells' dynamic morphologies govern blood shear thinning under

microcirculatory flow conditions. *Proceedings of the National Academy of Sciences*, 113(47):13289–13294, 2016.

[22] Manouk Abkarian and Annie Viallat. Vesicles and red blood cells in shear flow. *Soft Matter*, 4(4):653–657, 2008.

[23] F Edwards-Lévy, M-C Andry, and M-C Lévy. Determination of free amino group content of serum albumin microcapsules using trinitrobenzenesulfonic acid: effect of variations in polycondensation ph. *International journal of pharmaceutics*, 96(1-3):85–90, 1993.

[24] F Edwards-Lévy and M-C Lévy. Serum albumin–alginate coated beads: mechanical properties and stability. *Biomaterials*, 20(21):2069–2084, 1999.

[25] Clément De Loubens, Julien Deschamps, Marc Georgelin, Anne Charrier, Florence Edwards-Levy, and Marc Leonetti. Mechanical characterization of cross-linked serum albumin microcapsules. *Soft matter*, 10(25):4561–4568, 2014.

[26] Liesbeth J De Cock, Stefaan De Koker, Bruno G De Geest, Johan Grooten, Chris Vervaet, Jean Paul Remon, Gleb B Sukhorukov, and Maria N Antipina. Polymeric multilayer capsules in drug delivery. *Angewandte Chemie International Edition*, 49(39):6954–6973, 2010.

[27] Uttam Manna and Satish Patil. Dual drug delivery microcapsules via layer-by-layer self-assembly. *Langmuir*, 25(18):10515–10522, 2009.

[28] Deniz Z Gunes, Matthieu Pouzot, Martine Rouvet, Stéphane Ulrich, and Raffaele Mezzenga. Tuneable thickness barriers for composite o/w and w/o capsules, films, and their decoration with particles. *Soft Matter*, 7(19):9206–9215, 2011.

[29] X-Q Hu, A-V Salsac, and D Barthès-Biesel. Flow of a spherical capsule in a pore with circular or square cross-section. *Journal of Fluid Mechanics*, 705:176–194, 2012.

[30] E Foessel, J Walter, A-V Salsac, and D Barthès-Biesel. Influence of internal viscosity on the large deformation and buckling of a spherical capsule in a simple shear flow. *Journal of Fluid Mechanics*, 672:477–486, 2011.

[31] Narla Mohandas and Evan Evans. Mechanical properties of the red cell membrane in relation to molecular structure and genetic defects. *Annual review of biophysics and biomolecular structure*, 23(1):787–818, 1994.

[32] C Ross Ethier and Craig A Simmons. *Introductory biomechanics: from cells to organisms*. Cambridge University Press, 2007.

[33] Petia M Vlahovska, Thomas Podgorski, and Chaouqi Misbah. Vesicles and red blood cells in flow: From individual dynamics to rheology. *Comptes Rendus Physique*, 10(8):775–789, 2009.

[34] David Abreu, Michael Levant, Victor Steinberg, and Udo Seifert. Fluid vesicles in flow. *Advances in colloid and interface science*, 208:129–141, 2014.

[35] TX Chu, A-V Salsac, E Leclerc, D Barthès-Biesel, H Wurtz, and F Edwards-Lévy. Comparison between measurements of elasticity and free amino group content of ovalbumin microcapsule membranes: discrimination of the cross-linking degree. *Journal of colloid and interface science*, 355(1):81–88, 2011.

[36] Muriel Carin, Dominique Barthès-Biesel, Florence Edwards-Lévy, Caroline Postel, and Diana Cristina Andrei. Compression of biocompatible liquid-filled hsa-alginate capsules: Determination of the membrane mechanical properties. *Biotechnology and bioengineering*, 82(2):207–212, 2003.

[37] Frédéric Risso and Muriel Carin. Compression of a capsule: Mechanical laws of membranes with negligible bending stiffness. *Physical Review E*, 69(6):061601, 2004.

[38] Frédéric Risso, Fabienne CollÉ-Paillot, and Mokhtar Zagzoule. Experimental investigation of a bioartificial capsule flowing in a narrow tube. *Journal of fluid mechanics*, 547:149–173, 2006.

[39] Heinz Rehage, Martin Husmann, and Anja Walter. From two-dimensional model networks to microcapsules. *Rheologica acta*, 41(4):292–306, 2002.

[40] Inteaz Alli Catherine N. Mulligan Bernard F. Gibbs, Selim Kermasha. Encapsulation in the food industry: a review. *International journal of food sciences and nutrition*, 50(3):213–224, 1999.

[41] Alireza Abbaspourrad, Sujit S Datta, and David A Weitz. Controlling release from ph-responsive microcapsules. *Langmuir*, 29(41):12697–12702, 2013.

[42] Utai Klinkesorn and David Julian McClements. Influence of chitosan on stability and lipase digestibility of lecithin-stabilized tuna oil-in-water emulsions. *Food Chemistry*, 114(4):1308–1315, 2009.

[43] Xing Ma, Xu Wang, Kersten Hahn, and Samuel Sánchez. Motion control of urea-powered biocompatible hollow microcapsules. *ACS nano*, 10(3):3597–3605, 2016.

[44] Qinghe Zhao, Baosan Han, Zhaohai Wang, Changyou Gao, and Jiacong Peng, Chenghong ansd Shen. Hollow chitosan-alginate multilayer microcapsules as drug delivery vehicle: doxorubicin loading and in vitro and in vivo studies. *Nanomedicine: Nanotechnology, Biology and Medicine*, 3(1):63–74, 2007.

[45] Fujian Huang, Wei-Ching Liao, Yang Sung Sohn, Rachel Nechushtai, Chun-Hua Lu, and Itamar Willner. Light-responsive and ph-responsive dna microcapsules for controlled release of loads. *Journal of the American Chemical Society*, 138(28):8936–8945, 2016.

[46] Lorena Betancor and Heather R Luckarift. Bioinspired enzyme encapsulation for biocatalysis. *Trends in biotechnology*, 26(10):566–572, 2008.

[47] Wynter J Duncanson, Tina Lin, Adam R Abate, Sebastian Seiffert, Rhutesh K Shah, and David A Weitz. Microfluidic synthesis of advanced microparticles for encapsulation and controlled release. *Lab on a Chip*, 12(12):2135–2145, 2012.

[48] Pranay Agarwal, Jung Kyu Choi, Haishui Huang, Shuting Zhao, Jenna Dumbleton, Jianrong Li, and Xiaoming He. A biomimetic core–shell platform for miniaturized 3d cell and tissue engineering. *Particle & Particle Systems Characterization*, 32(8):809–816, 2015.

[49] Donald L Elbert. Liquid–liquid two-phase systems for the production of porous hydrogels and hydrogel microspheres for biomedical applications: a tutorial review. *Acta biomaterialia*, 7(1):31–56, 2011.

[50] Max Donbrow. *Microcapsules and nanoparticles in medicine and pharmacy*. CRC press, 1991.

[51] Clement De Loubens, Julien Deschamps, Florence Edwards-Levy, and Marc Leonetti. Tank-treading of microcapsules in shear flow. *Journal of Fluid Mechanics*, 789:750–767, 2016.

[52] Anja Unverfehrt and Heinz Rehage. Deformation, orientation and bursting of microcapsules in simple shear flow: Wrinkling processes, tumbling and swinging motions. *Procedia IUTAM*, 16:12–21, 2015.

[53] C Pozrikidis. Finite deformation of liquid capsules enclosed by elastic membranes in simple shear flow. *Journal of Fluid Mechanics*, 297:123–152, 1995.

[54] Dominique Barthès-Biesel. Modeling the motion of capsules in flow. *Current opinion in colloid & interface science*, 16(1):3–12, 2011.

[55] Dominique Barthès-Biesel. Capsule motion in flow: Deformation and membrane buckling. *Comptes Rendus Physique*, 10(8):764–774, 2009.

[56] Dominique Barthes-Biesel, Anna Diaz, and Emmanuelle Dhenin. Effect of constitutive laws for two-dimensional membranes on flow-induced capsule deformation. *Journal of Fluid Mechanics*, 460:211–222, 2002.

[57] Clement De Loubens, Julien Deschamps, Gwenn Boedec, and Marc Leonetti. Stretching of capsules in an elongation flow, a route to constitutive law. *Journal of Fluid Mechanics*, 767, 2015.

[58] R Skalak, A Tozeren, RP Zarda, and S Chien. Strain energy function of red blood cell membranes. *Biophysical journal*, 13(3):245–264, 1973.

[59] D Barthes-Biesel. Mechanics of encapsulated droplets. In *Structure, Dynamics and Properties of Disperse Colloidal Systems*, pages 58–64. Springer, 1998.

[60] Yannick Lefebvre, Eric Leclerc, Dominique Barthès-Biesel, Johann Walter, and Florence Edwards-Lévy. Flow of artificial microcapsules in microfluidic channels: a method for determining the elastic properties of the membrane. *Physics of Fluids*, 20(12):123102, 2008.

[61] X-Q Hu, B Sévénié, A-V Salsac, E Leclerc, and D Barthès-Biesel. Characterizing the membrane properties of capsules flowing in a square-section microfluidic channel: effects of the membrane constitutive law. *Physical Review E*, 87(6):063008, 2013.

[62] Dominique Barthes-Biesel and H Sgaier. Role of membrane viscosity in the orientation and deformation of a spherical capsule suspended in shear flow. *Journal of Fluid Mechanics*, 160:119–135, 1985.

[63] Alireza Yazdani and Prosenjit Bagchi. Influence of membrane viscosity on capsule dynamics in shear flow. *Journal of Fluid Mechanics*, 718:569–595, 2013.

[64] P Dimitrakopoulos. Dumbbell formation for elastic capsules in nonlinear extensional stokes flows. *Physical Review Fluids*, 2(6):063101, 2017.

[65] J Walter, A-V Salsac, D Barthès-Biesel, and P Le Tallec. Coupling of finite element and boundary integral methods for a capsule in a stokes flow. *International journal for numerical methods in engineering*, 83(7):829–850, 2010.

[66] Sebastian Knoche and Jan Kierfeld. Buckling of spherical capsules. *Physical Review E*, 84(4):046608, 2011.

[67] C Pozrikidis. Effect of membrane bending stiffness on the deformation of capsules in simple shear flow. *Journal of Fluid Mechanics*, 440:269–291, 2001.

[68] Dominique Barthes-Biesel and JM Rallison. The time-dependent deformation of a capsule freely suspended in a linear shear flow. *Journal of Fluid Mechanics*, 113:251–267, 1981.

[69] Manouk Abkarian, Colette Lartigue, and Annie Viallat. Tank treading and unbinding of deformable vesicles in shear flow: determination of the lift force. *Physical review letters*, 88(6):068103, 2002.

[70] Constantine Pozrikidis. *Modeling and simulation of capsules and biological cells*. CRC Press, 2003.

[71] Kaili Xie, Clément De Loubens, Frédéric Dubreuil, Deniz Z Gunes, Marc Jaeger, and Marc Léonetti. Interfacial rheological properties of self-assembling biopolymer microcapsules. *Soft matter*, 13(36):6208–6217, 2017.

[72] Geoffrey Ingram Taylor. The formation of emulsions in definable fields of flow. *Proc. R. Soc. Lond. A*, 146(858):501–523, 1934.

[73] S Ramanujan and C Pozrikidis. Deformation of liquid capsules enclosed by elastic membranes in simple shear flow: large deformations and the effect of fluid viscosities. *Journal of Fluid Mechanics*, 361:117–143, 1998.

[74] Chaouqi Misbah. Vacillating breathing and tumbling of vesicles under shear flow. *Physical review letters*, 96(2):028104, 2006.

[75] A Unverfehrt, I Koleva, and H Rehage. Wrinkling, tumbling and swinging microcapsules in simple shear flow. In *AIP Conference Proceedings*, volume 1593, pages 746–749. AIP, 2014.

[76] Alireza ZK Yazdani, R Murthy Kalluri, and Prosenjit Bagchi. Tank-treading and tumbling frequencies of capsules and red blood cells. *Physical Review E*, 83(4):046305, 2011.

[77] Thomas M Fischer, M Stohr-Lissen, and Holger Schmid-Schonbein. The red cell as a fluid droplet: tank tread-like motion of the human erythrocyte membrane in shear flow. *Science*, 202(4370):894–896, 1978.

[78] Stuart R Keller and Richard Skalak. Motion of a tank-treading ellipsoidal particle in a shear flow. *Journal of Fluid Mechanics*, 120:27–47, 1982.

[79] Vasiliy Kantsler and Victor Steinberg. Orientation and dynamics of a vesicle in tank-treading motion in shear flow. *Physical review letters*, 95(25):258101, 2005.

[80] Manouk Abkarian, Magalie Faivre, and Annie Viallat. Swinging of red blood cells under shear flow. *Physical review letters*, 98(18):188302, 2007.

[81] JM Skotheim and Timothy W Secomb. Red blood cells and other nonspherical capsules in shear flow: oscillatory dynamics and the tank-treading-to-tumbling transition. *Physical review letters*, 98(7):078301, 2007.

[82] Hiroshi Noguchi and Gerhard Gompper. Fluid vesicles with viscous membranes in shear flow. *Physical review letters*, 93(25):258102, 2004.

[83] A Walter, H Rehage, and H Leonhard. Shear-induced deformations of polyamide microcapsules. *Colloid and Polymer Science*, 278(2):169–175, 2000.

[84] TM Fischer, CW Haest, M Stöhr-Liesen, H Schmid-Schönbein, and R Skalak. The stress-free shape of the red blood cell membrane. *Biophysical journal*, 34(3):409–422, 1981.

[85] Timothy W Secomb, R Skalak, N Özkaya, and JF Gross. Flow of axisymmetric red blood cells in narrow capillaries. *Journal of Fluid Mechanics*, 163:405–423, 1986.

[86] Etienne Lac and Dominique Barthès-Biesel. Deformation of a capsule in simple shear flow: effect of membrane prestress. *Physics of Fluids*, 17(7):072105, 2005.

[87] Claire Dupont, P Le Tallec, Dominique Barthes-Biesel, Marina Vidrascu, and A-V Salsac. Dynamics of a spherical capsule in a planar hyperbolic flow: influence of bending resistance. *Procedia IUTAM*, 16:70–79, 2015.

[88] Claire Dupont, A-V Salsac, Dominique Barthes-Biesel, Marina Vidrascu, and Patrick Le Tallec. Influence of bending resistance on the dynamics of a spherical capsule in shear flow. *Physics of Fluids*, 27(5):051902, 2015.

[89] Xiaoyi Li and Kausik Sarkar. Front tracking simulation of deformation and buckling instability of a liquid capsule enclosed by an elastic membrane. *Journal of Computational Physics*, 227(10):4998–5018, 2008.

[90] Luka Pocivavsek, Robert Dellsy, Andrew Kern, Sebastián Johnson, Binhua Lin, Ka Yee C Lee, and Enrique Cerda. Stress and fold localization in thin elastic membranes. *Science*, 320(5878):912–916, 2008.

[91] Fabian Brau, Hugues Vandeparre, Abbas Sabbah, Christophe Poulard, Arezki Boudaoud, and Pascal Damman. Multiple-length-scale elastic instability mimics parametric resonance of nonlinear oscillators. *Nature Physics*, 7(1):56, 2011.

[92] Lifeng Wang, Carlos E Castro, and Mary C Boyce. Growth strain-induced wrinkled membrane morphology of white blood cells. *Soft Matter*, 7(24):11319–11324, 2011.

[93] Tuomas Tallinen, Jun Young Chung, François Rousseau, Nadine Girard, Julien Lefèvre, and Lakshminarayanan Mahadevan. On the growth and form of cortical convolutions. *Nature Physics*, 12(6):588, 2016.

[94] DG Roddeman, J Drukker, CWJ Oomens, and JD Janssen. The wrinkling of thin membranes: Part i—theory. *Journal of Applied Mechanics*, 54(4):884–887, 1987.

[95] Enrique Cerda, K Ravi-Chandar, and L Mahadevan. Thin films: Wrinkling of an elastic sheet under tension. *Nature*, 419(6907):579, 2002.

[96] Enrique Cerda and Lakshminarayanan Mahadevan. Geometry and physics of wrinkling. *Physical review letters*, 90(7):074302, 2003.

[97] Jiangshui Huang, Megan Juszkiewicz, Wim H De Jeu, Enrique Cerda, Todd Emrick, Narayanan Menon, and Thomas P Russell. Capillary wrinkling of floating thin polymer films. *Science*, 317(5838):650–653, 2007.

[98] Maria Ina, Aleksandr P Zhushma, Natalia V Lebedeva, Mohammad Vatankhah-Varnoosfaderani, Sean D Olson, and Sergei S Sheiko. The design of wrinkled microcapsules for enhancement of release rate. *Journal of colloid and interface science*, 478:296–302, 2016.

[99] Guanghui Ma and Zhi-Guo Su. *Microspheres and microcapsules in biotechnology: design, preparation and applications*. Pan Stanford, 2013.

[100] Rahul B Karyappa, Shivraj D Deshmukh, and Rochish M Thaokar. Deformation of an elastic capsule in a uniform electric field. *Physics of Fluids*, 26(12):122108, 2014.

[101] Harold P Grace. Dispersion phenomena in high viscosity immiscible fluid systems and application of static mixers as dispersion devices in such systems. *Chemical Engineering Communications*, 14(3-6):225–277, 1982.

[102] D Barthes-Biesel. Role of interfacial properties on the motion and deformation of capsules in shear flow. *Physica A: Statistical Mechanics and its Applications*, 172(1-2):103–124, 1991.

[103] M Husmann, H Rehage, E Dhenin, and D Barthès-Biesel. Deformation and bursting of nonspherical polysiloxane microcapsules in a spinning-drop apparatus. *Journal of colloid and interface science*, 282(1):109–119, 2005.

[104] XZ Li, D Barthes-Biesel, and A Helmy. Large deformations and burst of a capsule freely suspended in an elongational flow. *Journal of fluid mechanics*, 187:179–196, 1988.

[105] Hugo Doméjean, Mathieu de la Motte Saint Pierre, Anette Funfak, Nicolas Atrux-Tallau, Kevin Alessandri, Pierre Nassoy, Jérôme Bibette, and Nicolas Bremond. Controlled production of sub-millimeter liquid core hydrogel capsules for parallelized 3d cell culture. *Lab on a Chip*, 17(1):110–119, 2017.

[106] Isabel M Martins, Maria F Barreiro, Manuel Coelho, and Alirio E Rodrigues. Microencapsulation of essential oils with biodegradable polymeric carriers for cosmetic applications. *Chemical Engineering Journal*, 245:191–200, 2014.

[107] Xu-Qu Hu. *Motion and deformation of capsules flowing in microfluidic channels*. Theses, Université de Technologie de Compiègne, March 2013.

[108] I Burgaud, E Dickinson, and PV Nelson. An improved high-pressure homogenizer for making fine emulsions on a small scale. *International journal of food science & technology*, 25(1):39–46, 1990.

[109] Rodrigo Bocanegra, Anikumar G Gaonkar, Antonio Barrero, Ignacio G Loscertales, David Pechack, and Manuel Marquez. Production of cocoa butter microcapsules using an electrospray process. *Journal of food science*, 70(8):e492–e497, 2005.

[110] Yu Fukui, Tatsuo Maruyama, Yuko Iwamatsu, Akihiro Fujii, Tsutomu Tanaka, Yoshikage Ohmukai, and Hideto Matsuyama. Preparation of monodispersed polyelectrolyte microcapsules with high encapsulation efficiency by an electrospray technique. *Colloids and Surfaces A: Physicochemical and Engineering Aspects*, 370(1-3):28–34, 2010.

[111] Heike Karbstein and Helmar Schubert. Developments in the continuous mechanical production of oil-in-water macro-emulsions. *Chemical Engineering and Processing: Process Intensification*, 34(3):205–211, 1995.

[112] Mariana Petronela Hanga and Richard G Holdich. Membrane emulsification for the production of uniform poly-n-isopropylacrylamide-coated alginate particles using internal gelation. *Chemical Engineering Research and Design*, 92(9):1664–1673, 2014.

[113] GT Vladisavljević, Isao Kobayashi, and Mitsutoshi Nakajima. Production of uniform droplets using membrane, microchannel and microfluidic emulsification devices. *Microfluidics and nanofluidics*, 13(1):151–178, 2012.

[114] Rhutesh K Shah, Jin-Woong Kim, Jeremy J Agresti, David A Weitz, and Liang-Yin Chu. Fabrication of monodisperse thermosensitive microgels and gel capsules in microfluidic devices. *Soft Matter*, 4(12):2303–2309, 2008.

[115] Kwanghun Chung, Yoosik Kim, Jitendra S Kanodia, Emily Gong, Stanislav Y Shvartsman, and Hang Lu. A microfluidic array for large-scale ordering and orientation of embryos. *Nature methods*, 8(2):171, 2010.

[116] Aude Munin and Florence Edwards-Lévy. Encapsulation of natural polyphenolic compounds; a review. *Pharmaceutics*, 3(4):793–829, 2011.

[117] F Edwards-Lévy, M-C Andry, and M-C Lévy. Determination of free amino group content of serum albumin microcapsules: Ii. effect of variations in reaction time and in terephthaloyl chloride concentration. *International journal of pharmaceutics*, 103(3):253–257, 1994.

[118] Angus PR Johnston, Christina Cortez, Alexandra S Angelatos, and Frank Caruso. Layer-by-layer engineered capsules and their applications. *Current Opinion in Colloid & Interface Science*, 11(4):203–209, 2006.

[119] Hong Zhang, Ethan Tumarkin, Raheem Peerani, Zhihong Nie, Ruby May A Sullan, Gilbert C Walker, and Eugenia Kumacheva. Microfluidic production of biopolymer microcapsules with controlled morphology. *Journal of the american chemical society*, 128(37):12205–12210, 2006.

[120] TX Chu, A-V Salsac, D Barthes-Biesel, L Griscom, F Edwards-Lévy, and E Leclerc. Fabrication and in situ characterization of microcapsules in a microfluidic system. *Microfluidics and nanofluidics*, 14(1-2):309–317, 2013.

[121] DO Grigoriev, T Bukreeva, H Möhwald, and DG Shchukin. New method for fabrication of loaded micro-and nanocontainers: emulsion encapsulation by polyelectrolyte layer-by-layer deposition on the liquid core. *Langmuir*, 24(3):999–1004, 2008.

[122] Eduardo Guzmán, Ana Mateos-Maroto, Marta Ruano, Francisco Ortega, and Ramón G Rubio. Layer-by-layer polyelectrolyte assemblies for encapsulation and release of active compounds. *Advances in colloid and interface science*, 249:290–307, 2017.

[123] Julien Dupré de Baubigny, Corentin Trégouët, Thomas Salez, Nadège Pantoustier, Patrick Perrin, Mathilde Reyssat, and Cécile Monteux. One-step fabrication of ph-responsive membranes and microcapsules through interfacial h-bond polymer complexation. *Scientific reports*, 7(1):1265, 2017.

[124] Sandrine Le Tirilly, Corentin Tregouet, Mathilde Reyssat, Stephane Bone, Cedric Geffroy, Gerald Fuller, Nadege Pantoustier, Patrick Perrin, and Cécile Monteux. Interfacial rheology of hydrogen-bonded polymer multilayers assembled at liquid interfaces: Influence of anchoring energy and hydrophobic interactions. *Langmuir*, 32(24):6089–6096, 2016.

[125] Paul F Noble, Olivier J Cayre, Rossitza G Alargova, Orlin D Velev, and Vesselin N Paunov. Fabrication of "hairy" colloidosomes with shells of polymeric microrods. *Journal of the American Chemical Society*, 126(26):8092–8093, 2004.

[126] Sneha Puri and Rochish M Thaokar. Study of dependence of elasticity on the microstructure of microcapsules using electro-deformation technique. *Colloids and Surfaces A: Physicochemical and Engineering Aspects*, 569:179–189, 2019.

[127] M-C Andry, F Edwards-Lévy, and M-C Lévy. Free amino group content of serum albumin microcapsules. iii. a study at low ph values. *International journal of pharmaceutics*, 128(1-2):197–202, 1996.

[128] Rahul B Karyappa, Shivraj D Deshmukh, and Rochish M Thaokar. Breakup of a conducting drop in a uniform electric field. *Journal of Fluid Mechanics*, 754:550–589, 2014.

[129] Lorenz Baumgarten and Jan Kierfeld. Buckling of thermally fluctuating spherical shells: Parameter renormalization and thermally activated barrier crossing. *Physical Review E*, 97(5):052801, 2018.

[130] Andrew R Salmon, Richard M Parker, Alexander S Groombridge, Armando Maestro, Roger J Coulston, Jonas Hegemann, Jan Kierfeld, Oren A Scherman, and Chris Abell. Microcapsule buckling triggered by compression-induced interfacial phase change. *Langmuir*, 32(42):10987–10994, 2016.

[131] Lixiong Wen and Kyriakos D Papadopoulos. Effects of surfactants on water transport in w1/o/w2 emulsions. *Langmuir*, 16(20):7612–7617, 2000.

[132] Philipp Erni, Huda A Jerri, Kenneth Wong, and Alan Parker. Interfacial viscoelasticity controls buckling, wrinkling and arrest in emulsion drops undergoing mass transfer. *Soft Matter*, 8(26):6958–6967, 2012.

[133] Shupeng She, Chunxiu Xu, Xuefeng Yin, Weijun Tong, and Changyou Gao. Shape deformation and recovery of multilayer microcapsules after being squeezed through a microchannel. *Langmuir*, 28(11):5010–5016, 2012.

[134] Sujit S Datta, Shin-Hyun Kim, Jayson Paulose, Alireza Abbaspourrad, David R Nelson, and David A Weitz. Delayed buckling and guided folding of inhomogeneous capsules. *Physical review letters*, 109(13):134302, 2012.

[135] Lixiong Wen and Kyriakos D Papadopoulos. Effects of osmotic pressure on water transport in w1/o/w2 emulsions. *Journal of colloid and interface science*, 235(2):398–404, 2001.

[136] Jana Bahtz, Deniz Z Gunes, Eric Hughes, Lea Pokorny, Francesca Riesch, Axel Syrbe, Peter Fischer, and Erich J Windhab. Decoupling of mass transport mechanisms in the stagewise swelling of multiple emulsions. *Langmuir*, 31(19):5265–5273, 2015.

[137] Shelley Lynn Anna. Droplets and bubbles in microfluidic devices. *Annual Review of Fluid Mechanics*, 48:285–309, 2016.

[138] Nicolas Gallé and Victor Steinberg. On-chip encapsulation via chaotic mixing. *Microfluidics and Nanofluidics*, 20(11):156, 2016.

[139] P Colinart, S Delepine, G Trouve, and H Renon. Water transfer in emulsified liquid membrane processes. *Journal of membrane Science*, 20(2):167–187, 1984.

[140] Olga I Vinogradova, D Andrienko, VV Lulevich, S Nordschild, and GB Sukhorukov. Young's modulus of polyelectrolyte multilayers from microcapsule swelling. *Macromolecules*, 37(3):1113–1117, 2004.

[141] Th Dracos. Particle tracking velocimetry (ptv). In *Three-Dimensional Velocity and Vorticity Measuring and Image Analysis Techniques*, pages 155–160. Springer, 1996.

[142] F Dubreuil, N Elsner, and A Fery. Elastic properties of polyelectrolyte capsules studied by atomic-force microscopy and ricm. *The European Physical Journal E*, 12(2):215–221, 2003.

[143] Weijun Tong, you Gao, and Helmuth Möhwald. Manipulating the properties of polyelectrolyte microcapsules by glutaraldehyde cross-linking. *Chemistry of materials*, 17(18):4610–4616, 2005.

[144] Amit Kumar and Michael D Graham. Margination and segregation in confined flows of blood and other multicomponent suspensions. *Soft Matter*, 8(41):10536–10548, 2012.

[145] Marco E Rosti, Luca Brandt, and Dhrubaditya Mitra. Rheology of suspensions of viscoelastic spheres: Deformability as an effective volume fraction. *Physical Review Fluids*, 3(1):012301, 2018.

[146] Lev Davidovich Landau and Eugin M Lifshitz. *Course of Theoretical Physics Vol 7: Theory and Elasticity*. Pergamon press, 1959.

[147] Valery G Babak, Elena A Merkovich, Leonid S Galbraikh, Eleonora V Shtykova, and Margueritte Rinaudo. Kinetics of diffusionally induced gelation and ordered nanostructure formation in surfactant–polyelectrolyte complexes formed at water/water emulsion type interfaces. *Mendeleev Communications*, 10(3):94–95, 2000.

[148] Pierre-Yves Gires, Dominique Barthès-Biesel, Eric Leclerc, and Anne-Virginie Salsac. Transient behavior and relaxation of microcapsules with a cross-linked human serum albumin membrane. *Journal of the mechanical behavior of biomedical materials*, 58:2–10, 2016.

[149] Corentin Tregouët, Thomas Salez, Cecile Monteux, and Mathilde Reyssat. Microfluidic probing of the complex interfacial rheology of multilayer capsules. *Soft matter*, 2019.

[150] Derek C Tretheway and L Gary Leal. Deformation and relaxation of newtonian drops in planar extensional flows of a boger fluid. *Journal of non-newtonian fluid mechanics*, 99(2-3):81–108, 2001.

[151] Jingxin Shao, Mingjun Xuan, Tieyan Si, Luru Dai, and Qiang He. Biointerfacing polymeric microcapsules for in vivo near-infrared light-triggered drug release. *Nanoscale*, 7(45):19092–19098, 2015.

[152] Hongmei Bi, Shenghua Ma, Qingchuan Li, and Xiaojun Han. Magnetically triggered drug release from biocompatible microcapsules for potential cancer therapeutics. *Journal of Materials Chemistry B*, 4(19):3269–3277, 2016.

[153] Tatiana Borodina, Elena Markvicheva, Stanislav Kunizhev, Helmuth Möhwald, Gleb B Sukhorukov, and Oliver Kreft. Controlled release of dna from self-degrading microcapsules. *Macromolecular rapid communications*, 28(18-19):1894–1899, 2007.

[154] BJ Blaiszik, MM Caruso, DA McIlroy, JS Moore, SR White, and NR Sottos. Microcapsules filled with reactive solutions for self-healing materials. *Polymer*, 50(4):990–997, 2009.

[155] F-D_ Rumscheidt and SG Mason. Particle motions in sheared suspensions xii. deformation and burst of fluid drops in shear and hyperbolic flow. *Journal of Colloid Science*, 16(3):238–261, 1961.

[156] Charles D Eggleton, Tse-Min Tsai, and Kathleen J Stebe. Tip streaming from a drop in the presence of surfactants. *Physical review letters*, 87(4):048302, 2001.

[157] JJM Janssen, A Boon, and WGM Agterof. Influence of dynamic interfacial properties on droplet breakup in plane hyperbolic flow. *AIChE journal*, 43(6):1436–1447, 1997.

[158] Zhongwei Niu, Jinbo He, Thomas P Russell, and Qian Wang. Synthesis of nano/microstructures at fluid interfaces. *Angewandte Chemie International Edition*, 49(52):10052–10066, 2010.

[159] Giacomo Gallino, Tobias M Schneider, and François Gallaire. Edge states control droplet breakup in subcritical extensional flows. *Physical Review Fluids*, 3(7):073603, 2018.

[160] D Barthes-Biesel and Andreas Acrivos. Deformation and burst of a liquid droplet freely suspended in a linear shear field. *Journal of Fluid Mechanics*, 61(1):1–22, 1973.

[161] JM Rallison. A numerical study of the deformation and burst of a viscous drop in general shear flows. *Journal of Fluid Mechanics*, 109:465–482, 1981.

[162] S Torza, RG Cox, and SG Mason. Particle motions in sheared suspensions xxvii. transient and steady deformation and burst of liquid drops. *Journal of colloid and interface science*, 38(2):395–411, 1972.

[163] JM Rallison. Note on the time-dependent deformation of a viscous drop which is almost spherical. *Journal of Fluid Mechanics*, 98(3):625–633, 1980.

[164] Lord Rayleigh. On the instability of jets. *Proceedings of the London mathematical society*, 1(1):4–13, 1878.

[165] WJ Milliken and LG Leal. Deformation and breakup of viscoelastic drops in planar extensional flows. *Journal of non-newtonian fluid mechanics*, 40(3):355–379, 1991.

[166] Charlotte Py, Paul Reverdy, Lionel Doppler, José Bico, Benoit Roman, and Charles N Baroud. Capillary origami: spontaneous wrapping of a droplet with an elastic sheet. *Physical review letters*, 98(15):156103, 2007.

[167] Kai Liu, Caleb Hamilton, Jun Allard, John Lowengrub, and Shuwang Li. Wrinkling dynamics of fluctuating vesicles in time-dependent viscous flow. *Soft matter*, 12(26):5663–5675, 2016.

[168] Hunter King, Robert D Schroll, Benny Davidovitch, and Narayanan Menon. Elastic sheet on a liquid drop reveals wrinkling and crumpling as distinct symmetry-breaking instabilities. *Proceedings of the National Academy of Sciences*, 109(25):9716–9720, 2012.

[169] Jonas Hegemann, Horst-Holger Boltz, and Jan Kierfeld. Elastic capsules at liquid-liquid interfaces. *Soft Matter*, 2018.

[170] Yifan Yang, Hui-Hui Dai, Fan Xu, and Michel Potier-Ferry. Pattern transitions in a soft cylindrical shell. *Physical review letters*, 120(21):215503, 2018.

[171] Munehiro Asally, Mark Kittisopikul, Pau Rué, Yingjie Du, Zhenxing Hu, Tolga Çağatay, Andra B Robinson, Hongbing Lu, Jordi Garcia-Ojalvo, and Gürol M Süel. Localized cell death focuses mechanical forces during 3d patterning in a biofilm. *Proceedings of the National Academy of Sciences*, 109(46):18891–18896, 2012.

[172] Stephan Freiberg and XX Zhu. Polymer microspheres for controlled drug release. *International journal of pharmaceutics*, 282(1-2):1–18, 2004.

[173] Christian Wischnewski and Jan Kierfeld. Spheroidal and conical shapes of ferrofluid-filled capsules in magnetic fields. *Physical Review Fluids*, 3(4):043603, 2018.

[174] Norbert Stoop, Romain Lagrange, Denis Terwagne, Pedro M Reis, and Jörn Dunkel. Curvature-induced symmetry breaking determines elastic surface patterns. *Nature materials*, 14(3):337, 2015.

[175] Douglas P Holmes and Alfred J Crosby. Draping films: A wrinkle to fold transition. *Physical review letters*, 105(3):038303, 2010.

[176] Dominic Vella, Amin Ajdari, Ashkan Vaziri, and Arezki Boudaoud. Wrinkling of pressurized elastic shells. *Physical review letters*, 107(17):174301, 2011.

[177] Miguel Trejo, Carine Douarche, Virginie Bailleux, Christophe Poulard, Sandrine Mariot, Christophe Regeard, and Eric Raspaud. Elasticity and wrinkled morphology of bacillus subtilis pellicles. *Proceedings of the National Academy of Sciences*, 110(6):2011–2016, 2013.

[178] Sehoon Kwak and C Pozrikidis. Effect of membrane bending stiffness on the axisymmetric deformation of capsules in uniaxial extensional flow. *Physics of fluids*, 13(5):1234–1242, 2001.

[179] Steven Vandebril, Aly Franck, Gerald G Fuller, Paula Moldenaers, and Jan Vermant. A double wall-ring geometry for interfacial shear rheometry. *Rheologica Acta*, 49(2):131–144, 2010.

[180] Bernard Minifie. *Chocolate, cocoa and confectionery: science and technology*. Springer Science & Business Media, 2012.

[181] Isabelle Delaby, René Muller, and Benoit Ernst. Drop deformation during elongational flow in blends of viscoelastic fluids. small deformation theory and comparison with experimental results. *Rheologica acta*, 34(6):525–533, 1995.